Dissertation

Nonlinearity, topology and $\mathcal{PT}$ symmetry in Photonic Lattices

Gutachter

1. *Prof. Dr. Ulf Peschel*
    Institut für Festkörpertheorie und Optik
    Friedrich-Schiller-Universität Jena

2. *Prof. Dr. Alexander Szameit*
    Institut für Physik
    Universität Rostock

3. *Prof. Dr. Kestutis Staliunas*
    Catalan Institution for Research and Advanced Studies
    Universitat Politècnica de Catalunya

Tag der Disputation: 18.05.2020

"A little learning is a dang'rous thing;
Drink deep, or taste not the Pierian spring:
There shallow draughts intoxicate the brain,
And drinking largely sobers us again."

— Alexander Pope, "An Essay on Criticism".

Zusammenfassung

Bereits seit über einem Jahrzehnt besteht ein stetig wachsendes Interesse der Wissenschafts-
gemeinde an den hochaktuellen Themen von sogenannter Parität-Zeit ($\mathcal{PT}$) Symmetrie und
topologischen Phasen der Materie, die historisch aus nicht-hermitischen Erweiterungen der
Quantenmechanik bzw. Phasenübergängen ohne Symmetrieeinbruch in der Physik der kon-
densierten Materie stammen.

Jüngste technologische Fortschritte im Forschungsfeld der Photonik ermöglichten es,
einige der besondersten Aspekte der $\mathcal{PT}$ Symmetrie und der topologischen Materie sowohl
theoretisch als auch experimentell zu untersuchen und weiter zu entwickeln. $\mathcal{PT}$-symmetri-
sche, photonische Strukturen mit einer gezielten Anpassung von Verstärkungs- und Ver-
lustbereichen wurden zu einem neuen Paradigma für die unkonventionelle Steuerung des
Lichtflusses, und ebneten damit den Weg für neuartige Anwendungen in der Laserphysik,
der synthetischen optischen Materialien, Lichtsensoren und so weiter. Ebenso entstanden
im Bereich der Photonik schnell grundlegende Topologie-Ideen, die neue Möglichkeiten der
Lichtnutzung eröffneten, wie zum Beispiel einen robusten, rückstreuungsfreien Transport und
ein Thouless Pumping, um nur Einige zu nennen. Aufgrund der Universalität der topologis-
chen Prinzipien wurde eine Vielzahl von experimentellen optischen Plattformen realisierbar,
darunter optische Wellenleiter, Metamaterialien, optische Kristalle, Optomechanik, Photonik
auf Siliziumbasis, optische Resonatoren und Schaltkreis-QED.

Die meisten Aspekte der $\mathcal{PT}$ Symmetrie und Topologie sind im linearen Bereich, in
dem Lichtteilchen, Photonen, nicht miteinander interagieren, sehr gut erforscht. Im Gegen-
satz dazu sind sie in nichtlinearen optischen Systemen, die durch Selbstinteraktion und
Selbstlokalisierung von Licht in nichtlinearen Medien gekennzeichnet sind, bislang kaum
erforscht. In dieser Hinsicht ist das Ziel dieser Arbeit, diese einflussreichen Ideen in Rich-
tung nichtlineares Licht weiter auszudehnen, um schließlich neue Phänomene und Wech-
selwirkungen zwischen Nichtlinearität, $\mathcal{PT}$ Symmetrie und Topologie zu entdecken und
experimentell zu beobachten. Dazu untersuchen wir sowohl experimentell als auch theo-
retisch diskrete, photonische 1D- und 2D-Gitter mit synthetischen Dimensionen, die die
berühmten diskreten Quantenwanderungen imitieren und auf der extrem vielseitigen und
interferometrisch robusten experimentellen Technik namens Zeitmultiplex basieren. Die ex-
perimentellen Aufbauten bestehen im Wesentlichen aus Lichtleiterschleifen, die über pas-
sive oder aktive Lichtleiterstrahlteiler miteinander gekoppelt sind. Unsere besonderen Ak-
tivitäten betreffen die Entdeckung und experimentelle Beobachtung neuartiger und fasziniere-
nder Aspekte nicht-hermitischer diskreter Solitonen in $\mathcal{PT}$-symmetrischen Umgebungen und
topologischen chiralen Randzuständen unter der Einwirkung optischer Kerr-Nichtlinearität.

Abstract

Since over a decade, there is an ever-growing interest of scientific community towards the hot topics of so-called parity-time ($\mathcal{PT}$) symmetry and topological phases of matter, historically originating from non-Hermitian extensions of Quantum Mechanics and phase transitions without symmetry breaking in Condensed Matter Physics, respectively.

Recent technological advancements in Photonics allowed one to study and fruitfully develop some of the most peculiar aspects of $\mathcal{PT}$ symmetry and topological matter on both theoretical and experimental levels. $\mathcal{PT}$-symmetric photonic structures, with a judicious tailoring of gain and loss bulk regions, became a new paradigm in controlling the flow of light in unconventional manner, thereby paving the way to novel applications in laser physics, synthetic optical materials, optical sensing and so on. Likewise, fundamental ideas of topology rapidly emerged in the field of Photonics and brought about new possibilities for harnessing light, such as robust backscattering-free transport and Thouless pumping, to name a few. Owing to universality of the topological principles, a wide range of experimental platforms became feasible, including waveguides, metamaterials, optical crystals, optomechanics, silicon-based photonics, cavities and circuit QED.

Most of the aspects of $\mathcal{PT}$ symmetry and topology in Photonics are very well understood in the linear regime, where light particles, photons, do not interact with each other. In contrast, up to date, they remain hardly explored in nonlinear optical regimes, characterized by self-interaction and self-localization of light in nonlinear media. In that regard, the aim of this thesis is to extend those powerful ideas further on in the direction of nonlinear light, in order to eventually discover and experimentally observe novel phenomena and interplays between nonlinearity, $\mathcal{PT}$ symmetry and topology. For that, we study both experimentally and theoretically 1D and 2D Discrete Photonic Lattices with synthetic dimensions, mimicking the celebrated Discrete Quantum Walks and experimentally based on the extremely versatile and interferometrically robust technique, called time-multiplexing. The set-ups essentially consist of optical fiber loops, mutually coupled via passive or active in-fiber beam splitters. In particular, we discover and experimentally observe novel and fascinating aspects of non-Hermitian discrete solitons in $\mathcal{PT}$-symmetric environments and topological chiral edge states under the action of optical Kerr nonlinearity.

Contents

Introduction

Nowadays, perhaps the most general trend in science and particularly in physics is unification and systematization of an inconceivable amount of phenomena, effects and observations within a countable number of universal theories and concepts. Having once discovered a certain mathematical pattern or regularity in one still relatively abstract field of physics, a physicist then strives to bring it to another, technologically more advanced area, where an immediate experimental verification is possible. In the meantime, fairly often, the physicist may experience some discomfort, as if he has surgically transplanted a living tissue from a healthy man to a diseased one, hoping the latter will finally be cured. That misgiving is, for course, not groundless, since those experimental and collaterally theoretical explorations might not claim universality, and hence a reversal transition of the received knowledge backwards to the "donor" field is not always possible. In such situations, a careful researcher will resort, at least partly, to some kind of theoretical superstructure, terminologically stuffed with prefixes like "artificial", "quasi", "pseudo", etc. As a result, one might acquire a synthetic aftertaste of that knowledge. But nevertheless, should its natural character and universality be once disclosed, the true value of the entire explorations will rise significantly, in light of the aforementioned unification trend.

In that regard, recent extensive research activities [1, 2] represent one of such endeavours, called upon to bring the powerful concepts of topological order and parity-time ($\mathcal{PT}$) symmetry from Quantum Mechanics, Solid State and Condensed Matter Physics into the technologically progressive and versatile field of Photonics, the science of light.

In short, the groundbreaking idea of topological orders is that besides conventional states (orders) of matter like liquid, solid, gas, etc., described within Landau symmetry-breaking theory, there are other, quantum phases of matter, that transform one into another without any symmetry breaking and either correspond to long-range quantum entanglement or symmetry-protected short-range quantum entanglement. The latter entanglement type is closely related to the so-called topological insulators' phases. Although first studies on topological phases began 50 years ago with discoveries of the Berezinskii–Kosterlitz–Thouless transition [3–5] in thin films of liquid Helium and integer quantum Hall effect [6, 7] in two-dimensional magnetized electron gases, the great physical significance of those discoveries had been comprehended by the scientific community just recently, as it was remarkably distinguished by a Nobel Prize in 2016.

The general idea of $\mathcal{PT}$ symmetry in the framework of so-called pseudo-Hermitian quantum systems, having real-valued energies, is the following. Any energetic disbalance of an incoming (gain) and outcoming (loss) energy flow from an environment to an open non-Hermitian system and vice versa inevitably lead to an energy amplification or attenuation inside the system. Although such a non-Hermitian behaviour of quantum systems is generally forbidden by postulates of Quantum Mechanics, the first seminal works by Bender and Boettcher [8, 9] hypothetically argued that a judicious distribution of gain and loss regions in a system can conversely lead to a quasi-conservative evolution, meaning that while the

instantaneous total energy periodically oscillates in time, its averaged value remains constant. The key (although in general neither sufficient nor necessary) prerequisite for the quasi-conservative evolution is the compatibility of the open system with $\mathcal{PT}$ symmetry. In contrast to the topological phases of matter and unlike the universal $\mathcal{CPT}$ symmetry of all forces in nature, a fundamental role of $\mathcal{PT}$ symmetry in nature is still to be revealed, since most of the $\mathcal{PT}$ symmetric systems have been realized experimentally exclusively in Photonics, by means of classical light amplification and attenuation. Therefore, the driving force of current research activities in this direction lays mainly within Photonics itself, and surprisingly enough, it does not stop to inspire us with ever newer discoveries.

The aim of this thesis is to extend those ideas even further, into the special and yet extremely diverse subfield of Nonlinear Optics, where they still remain largely unexplored from both experimental and theoretical sides. In particular, the role of the experimental platform for testing those concepts with self-interacting light is played by one- or two-dimensional Discrete Photonic Lattice with synthetic dimensions, mimicking the celebrated Discrete Quantum Walk via coherent optical pulses, propagating on the lattice. The synthetic dimensions are realized through the powerful experimental technique called time-multiplexing, which allows us to coherently implement almost all conceivable manipulations with light, namely with its phase, amplitude and trajectory. An exceptional interferometic robustness of time-multiplexed devices based on fiber optics provides us with extremely large distances of coherent light propagation, spanning up to 6000 km.

In the first purely theoretical chapter 1, we thoroughly investigate 1D and 2D beam splitter based Quantum Walks in the linear regime, including discrete light dynamics in terms of Floquet-Bloch extended waves, periodic phase and coupling modulations, principles and advantages of the time-multiplexing, underlying lattice symmetries and classification in the framework of non-interacting symmetry-protected topological insulators. The final part of this chapter is devoted to the concept of pseudo-Hermitian quasi-conservative evolution and, in particular, to $\mathcal{PT}$-symmetric complex potentials.

The second chapter 2 briefly covers principle schemes and technical features of the time-multiplexed set-ups with (1+1)D and (2+1)D synthetic dimensions. A more detailed description of the one-dimensional system, one can find in previous works [10, 11] of our former PhD student and my supervisor Martin Wimmer.

In the core part 3 of the dissertation, optical Kerr nonlinearity meets $\mathcal{PT}$ symmetry and topology. Nonlinear localized formations, such as discrete solitons and nonlinear topological edge states, branching in the linear limit from bulk eigenmodes and mid-gap topologically protected edge states, respectively, embody a complex synthesis of all the aforementioned concepts. Thereby, we reveal a series of fascinating interplays and establish non-trivial connections between seemingly unrelated phenomena, such as non-Hermitian power blow-up and conservative quasi-collapse of solitons, $\mathcal{PT}$-symmetric phase transitions and enhanced Bose-Einstein statistics of soliton's lifetimes, nonlinearity-induced instability of topological edge states and temporal Floquet modulation in Discrete Quantum Walks, nonlinear remote pumping of the edge states and chiral symmetry breaking, etc.

Finally, the last chapter 4 summarizes all principle outcomes of the thesis and outlines possible research directions within and beyond the paradigm of nonlinearity, topology and $\mathcal{PT}$ symmetry, that have not been covered in the current work.

Chapter 1

Theoretical background

1.1 Classical Random Walk

Continuous random walk describes stochastic motion of classical particles induced by random collisions with molecules, the so-called Brownian motion. On an individual level, the motion is completely random, while a macroscopic ensemble of such particles follows the diffusion Fokker-Planck equation, which in the simplest 1D case is

$$\frac{\partial \rho(x,t)}{\partial t} = -v\frac{\partial \rho(x,t)}{\partial x} + D\frac{\partial^2 \rho(x,t)}{\partial x^2}, \tag{1.1}$$

where $\rho(x,t)$ is the particle density in space x and time t, v and D and constant drift (average) velocity and diffusion coefficient, respectively. One can see that the equation does not obey time-reversal symmetry ($t \to -t, v \to -v$) unless $D = 0$, indicating an irreversible stochastic nature of the underlying Brownian motion.

A discrete counterpart of the random walk is traditionally demonstrated with the so-called Galdon Board (see Fig. 1.1), in which beads are falling down through a vertical board with interleaved rows of pegs. At every new horizontal level of the pegs, they bounce either left or right and move further below. Eventually, the beads are collected into bins at the bottom.

In general, the walk characterized by a random discrete position n updating every time
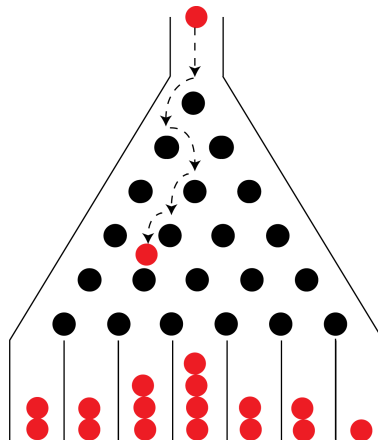

Figure 1.1: Galton board

step m as

$$n_{m+1} = n_m + \Delta n_{m+1}, \tag{1.2}$$

$$n_0 = 0, \tag{1.3}$$

can be asymmetric

$$\Delta n_m = \begin{cases} 1 & \text{with probability } p, \\ -1 & \text{with probability } 1-p, \end{cases} \tag{1.4}$$

i.e. the expectation value of the position $\langle n_m \rangle = \sum_{m'=0}^{m} \langle \Delta n_{m'} \rangle = m(2p-1)$ can change with the time step m, unless both probabilities to step right p and left $1-p$ are 50%. While calculating the expectation value, we assumed that the random variables Δn_m at different time steps are mutually independent and thus the random walk is a Markovian process [12]. Holding the same assumption for deriving the root-mean-square deviation after m time steps, we come up with

$$\sigma_m = \sqrt{\langle n_m^2 \rangle - \langle n_m \rangle^2} = \sqrt{mp(1-p)} \tag{1.5}$$

It is known from combinatorics, that the discrete variable n_m follows binomial distribution, which for a fixed p and in the limit of infinite m is approaching the normal distribution:

$$P(n_m) \sim \frac{1}{\sigma_m \sqrt{2\pi}} e^{-\frac{(n_m - \langle n_m \rangle)}{2\sigma_m}}. \tag{1.6}$$

This is the continuous limit of the system, since n_m can be treated as a continuous variable while the distribution width σ_m is growing with m. As a result, this continuous distribution is equivalent to the diffusive dynamics of the previously introduced continuous walk, recognized by its peculiar decelerating spreading speed

$$\frac{\mathrm{d}\sigma_m}{\mathrm{d}m} = \frac{\sqrt{p(1-p)}}{2\sqrt{m}}. \tag{1.7}$$

1.2 Discrete Quantum Walks in Optics

Random walk of a classical particle is dramatically different from that of a quantum particle, because of a conceptually new phenomena inherent to the latter, namely quantum superposition and quantum coherence [13]. As a result, a quantum walker doesn't randomly jump in one particular direction, but instead it "chooses" all directions simultaneously. Afterwards, its multiple trajectories spread, cross and interfere with each other in a wave-like manner, so that they can either suppress or amplify each other in case of a destructive or constructive interference, respectively. Multiple position states $|n\rangle$ of the walker at a given time step m can be superimposes together with corresponding complex amplitudes $\psi_{x,m}$, in order to form a quantum wavefunction of the particle state:

$$|\psi\rangle^m = \sum_n \psi_n^m |n\rangle. \tag{1.8}$$

According to Quantum Mechanics, a physical observation (detection) of the particle at a time step m and in one of the positions n will necessarily lead to collapse of the particle's wavefunction $|\psi\rangle^m$ into the corresponding single-position state $|n\rangle$. The particle's detection at the position n and the collapse will take place with the probability $|\psi_n^m|^2$. Since the probability to find the particle anywhere is 1 and the states $\{|n\rangle\}$ form an orthonormal basis, i.e. the particle can not be detected at several positions at the same time, one gets the normalization condition

$$\langle\psi|\psi\rangle^m = \sum_n |\psi_n^m|^2 \langle n|n\rangle = 1 \tag{1.9}$$

Similarly to the classical case, a future state at $m+1$ explicitly depends on its precursor at m only, however due to the quantum nature of the process all position shifts are possible at the same time, meaning that the walk evolution of a closed intact particle is essentially deterministic:

$$|\psi\rangle^{m+1} = \hat{U}|\psi\rangle^m, \tag{1.10}$$

where $\hat{U}$ is a discrete unitary evolution operator acting on the state every time step. The unitarity $\hat{U}^\dagger = \hat{U}^{-1}$ of the operator ensures probability conservation during the walk. In addition, the unitary evolution operator can be inverted, implying that the quantum walk dynamics can be reversed in time for an arbitrary number of time steps. This is a fundamental difference to the inherently irreversible classical walk, whose entropy steadily increases according to the second law of thermodynamics. Nevertheless, any external disturbance of the quantum coherence (e.g. via detection) can introduce some degree of stochasticity as well, thus leading to a completely or partly irreversible dynamics [14]. Along with Discrete Quantum Walks (DQWs) based on trapped atoms [15–18], ions [19–22], quantum QED [23, 24] and molecules in a strong magnetic field [25, 26] modern optics offers a number of alternative platforms such as optical waveguides and time-multiplexed fiber loops for realizing DQWs with coherent light [27–29], with single photons [28, 30–33] as well as with correlated photons [34–41].

Out of the great variety of photonic implementations, in this section we introduce one-dimensional (1D) and two-dimensional (2D) DQWs, based on 2×2 optical beam splitters. Further, we will show that each of them exhibits its peculiar photon dynamics as well as topological properties stemming from distinct network topologies. In addition, the systems under study generally represent a walk on a 1D or 2D periodic lattice with chiral (sublattice) symmetry, and therefore constructively they are similar to tight-binding models, originally proposed for electrons in Solid State Physics. Owing to the discretization of both temporal and spatial dimensions, we readily apply the concept of Bloch-Floquet periodic waves to study the wave-like dynamics of a walker. Although only two of the presented DWQs have been experimentally realized in our group via time-multiplexing, we nevertheless include two more walks (1D Hadamard and 2D walk of a four-component pseudospin) into consideration in order to give a broader view to the reader on beam splitter based networks.

1.2.1 1D Hadamard Walk of a polarized photon

The so-called Hadamard Walk of a single photon [42, 43], the most common example of a one-dimensional walk, is based on a photon's internal degree of freedom, the photon's helicity, which is also referred to as polarization. Quantum mechanical interpretation of the helicity is

the projection of the photon's spin angular momentum on its momentum, which can be ± 1 or 0 in agreement with Bose-Einstein statistics. Photons being massless relativistic particles do not have a rest reference frame and therefore such a projection is unique and invariant under Lorentz transformations. From the point of electromagnetism and according to Maxwell equations, an electromagnetic wave propagating in vacuum or a homogeneous medium can only be polarized in a plane perpendicular to the propagation direction. In other words, the wave has to be transverse and not longitudinal. In application to individual photons, this implies that only the helicity of +1 and -1 are possible, corresponding to the clockwise and counter-clockwise polarization, respectively. Conveniently, a generalized polarization state can be written as a superposition of these fundamental states or alternatively in the basis of horizontally $|H\rangle$ and vertically $|V\rangle$ polarized states $\psi_H |H\rangle + \psi_V |V\rangle$. This vector with two complex components is formally equivalent to a fermionic spinor state, which is a superposition of "spin-up" and "spin-down" states, characterized by a total half-integer spin. However, as we will see further, the helicity does not always transforms under time-reversal in the same way as a spinor, and therefore can not be directly associated with a genuine fermionic spin. Next, the walk itself takes place in a discrete spatial dimension and is characterized by the position state $\sum_n \psi_n |n\rangle$. All in all, the photon's state can be written via direct product as follows

$$|\psi\rangle = \sum_n (\psi_{H,n} |H\rangle \otimes |n\rangle + \psi_{V,n} |V\rangle \otimes |n\rangle) = \sum_n \begin{pmatrix} \psi_{H,n} \\ \psi_{V,n} \end{pmatrix} |n\rangle, \qquad (1.11)$$

where on the right-hand side the vectorial form is used for brevity. The normalization condition then reads as $\sum_n (|\psi_{H,n}|^2 + |\psi_{V,n}|^2) = 1$.

Next, we represent the homogeneous one-step evolution operator of the Hadamard Walk as

$$\hat{U} = \hat{S}\hat{C} \qquad (1.12)$$

consisting of two consecutive elementary operators, namely the Hadamard Coin

$$\hat{C} = \frac{1}{\sqrt{2}} \begin{pmatrix} 1 & 1 \\ 1 & -1 \end{pmatrix}, \qquad (1.13)$$

which locally rotates the polarization state counter-clockwise by 45° for all positions and the Shifter

$$\hat{S} = \sum_n \begin{pmatrix} |n+1\rangle \langle n| & 0 \\ 0 & |n-1\rangle \langle n| \end{pmatrix}, \qquad (1.14)$$

which shifts the position one step right or left depending on whether the polarization is $|H\rangle$ or $|V\rangle$, respectively. A physical implementation of the Shifter could be done by a polarizing beam splitter based on Fresnel reflection or the calcite beam displacer, acting as a birefringent crystal. In both cases, the polarization basis $|H\rangle$ and $|V\rangle$ has to be accordingly aligned with respect to the polarizer's operating axis. The way to physically realize the Hadamard Coin is however less obvious, because despite unitarity of the matrix ($\hat{C}^\dagger = \hat{C}^{-1}$), the optical element has to be asymmetric with respect to the horizontal and vertical polarization axes. Indeed, the symmetric flip (mirroring) of the Hadamard Coin with respect to the bisector of

the basis polarization axes does not lead to the same coin operator:

$$\hat{F}^{-1}\hat{C}\hat{F} \neq \hat{C}, \tag{1.15}$$

where

$$\hat{F} = \begin{pmatrix} 0 & 1 \\ 1 & 0 \end{pmatrix} \tag{1.16}$$

mutually flips two vectorial components of a polarization state. One special solution to this problem offered by linear optics is the half-wave phase retarder [44]:

$$\hat{C}_{\lambda/2}(\theta) = e^{-\frac{i\pi}{2}} \begin{pmatrix} \cos 2\theta & \sin 2\theta \\ \sin 2\theta & -\cos 2\theta \end{pmatrix}, \tag{1.17}$$

which delivers the Hadamard Coin, when the angle between the horizontal axis and the fast axis of the retarder $\theta = \pi/8$. The walk can be schematically represented as a series of walker's jumps between the optical principal elements, forming a one-dimensional chain in space, as shown in Fig. 1.2. Every knot of the chain rotates the horizontal and vertical linear polarization of a photon, incident from the left and right side, respectively, counter-clockwise by $45°$. Thereafter, the rotated state splits again into the horizontally and vertically polarized components, that propagate to the right and to the left neighbouring positions, respectively. In that regard, the direction of the position shift is linked to the corresponding polarization component.

Further, since the walker is constantly hopping to one of the two neighboring knots and never remains at the same position, it can only occupy either even or odd positions at a given time step. Therefore, the hopping takes place between two equivalent sublattices, that are distinguished by the blue and yellow colors of the beam splitters in the figure. Few comments regarding the notion of sublattice are in order:

1. The combination of two neighbouring elementary unit cells (knots) of one and another sublattice forms an elementary unit cell of the entire lattice. In other words, we use the term "sublattice" in a close analogy to the one used in crystallography, which is loosly defined as the lattice or array of atoms of a particular element in a compound or alloy. For more details on the notion of sublattice, see, for example, [45].

2. As a result of the next-nearest-neighbor hopping model, the number of hopping directions (left or right), which at the same time is the number of sublattices, coincides with dimensionality of the internal space of the photon.

3. Provided a single photon is launched into an even or odd position, further on it is hopping between one and another sublattice every time step and never occupies both sublattices at the same time. It is clear, that photon's dynamics does not depend on the initial choice (the even or odd position), since at any time step of the evolution one can always perfectly superimpose wavefunctions of two independent photons simultaneously launched into different sublattices by simply shifting one of the wavefunctions by the initial separation distance between photons. This fact directly follows from the so-called sublattice aka chiral symmetry of the walk, which will be extensively analysed further below in the context of symmetries and topology (see sections 1.7 and 1.6).

Owing to the temporal Floquet periodicity of the Discrete Quantum Walk, one can introduce two distinct descriptions of the evolution: 1) the one-step evolution operator $\hat{U}$ promotes a
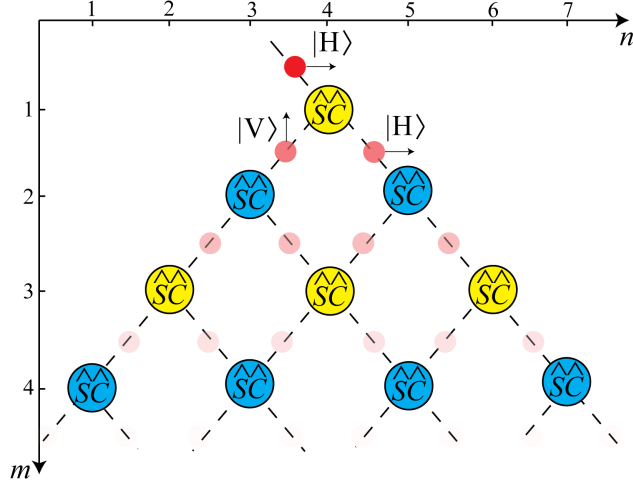
Figure 1.2: Hadamard Walk of a polarized photon (red disk). Optical elements at even (yellow) and odd (blue) positions ,respectively, represent two complementary sublattices.

wavefunction, which in general can occupy both sublattices or only one of them at a time, if initially only one sublattice is excited. This description will be further referred to as full or instantaneous picture; 2) if only one sublattice is initially excited, one can effectively trace that sublattice at every second time step by using the compound stroboscopic evolution operator $\hat{U}_{\text{eff}} = \hat{U}\hat{U}$. In presence of the above mentioned sublattice symmetry, this stroboscopic picture works without loss of generality and therefore it is dynamically equivalent to the full instantaneous picture. Note, however, that both pictures are fundamentally different from the perspective of symmetries and topology, as will be clarified in sections 1.7 and 1.6. But so far, beginning with the dynamical characteristics of the free walk, we will use the effective stroboscopic picture $\hat{U}_{\text{eff}}$ without loss of generality. Next, provided the walk is conservative, i.e no particle absorption or amplification is possible in the closed system, the unitary evolution operator can always be mapped to an effective Hermitian Hamiltonian of the system H_{eff} via $\hat{U}_{\text{eff}} = \exp\left(i\hat{H}_{\text{eff}}\right)$. In order to evaluate the Hamiltonian as a logarithm of $\hat{U}_{\text{eff}}$, we shall diagonalize the evolution matrix by representing the states and operators in terms of its eigenvectors. Owing to the periodicity of the system in both time and space, we further apply the Floquet-Bloch theorem, which was originally developed for electrons in periodic crystals, and seek for a fundamental solution of the form

$$|k\rangle = \begin{pmatrix} \psi_H \\ \psi_V \end{pmatrix} \sum_{n \in \mathbb{Z}} e^{-i2kn} |2n\rangle \tag{1.18}$$

which is a spatially extended Bloch wave with a quasimomentum k, defined up to an integer multiple of π. The sublattice with even positions is chosen for convenience. Fourier transform of the Shifter to the quasimomentum reciprocal space yields

$$\hat{S} = \int_{-\pi/2}^{\pi/2} \begin{pmatrix} e^{ik} & 0 \\ 0 & e^{-ik} \end{pmatrix} |k\rangle \langle k| \, \mathrm{d}k \overset{\text{def}}{=\!=} \int_{-\pi/2}^{\pi/2} \hat{S}(k) |k\rangle \langle k| \, \mathrm{d}k. \tag{1.19}$$

It is easy to see that the operator acts locally on each quasimomentum and does not mix them together, unlike the position states. This implies that there is no interaction between the waves and that the evolution can be considered individually for each wave with the local

evolution operator:

$$\hat{U}_{\text{eff}}(k) = \hat{S}(k)\hat{C}\hat{S}(k)\hat{C}. \tag{1.20}$$

Finally, one can diagonalize the evolution matrix by solving the following eigenvalue problem:

$$\hat{U}_{\text{eff}}(k)\,|k\rangle = \begin{pmatrix} \lambda & 0 \\ 0 & \lambda \end{pmatrix} |k\rangle. \tag{1.21}$$

The resulting eigenvalues further lead us to the eigenenergies according to $\lambda = \exp(2iE)$, where the factor of 2 accounts for two time steps of the stroboscopic period. Hence, we obtain the following dispersion relation

$$E_\pm = \pm\frac{1}{2}\arccos\frac{1 + \cos 2k}{2} \tag{1.22}$$

with associated polarization eigenvectors

$$|k\rangle_\pm = \begin{pmatrix} e^{ik}\left(\cos k \pm \frac{\sqrt{6 + 2\cos 2k}}{2}\right) \\ 1 \end{pmatrix} \sum_{n\in\mathbb{Z}} e^{-i2kn}\,|2n\rangle. \tag{1.23}$$

Since the evolution is linear, it is not necessary to normalize the eigenvectors to 1. The first Brillouine Zone (BZ) of the band structure is depicted in Fig. 1.3a. Note, that both quasimomentum and quesienergy have the period of π, which corresponds to the evolution period of 2 in space and time. Two bands with positive and negative energies degenerate at $E = 0$. Also, there is a forbidden gap at $|E| > \pi/4$, where no states exist. In addition, we plot the group velocity $E'(k)$ in Fig. 1.3b, which by definition is the speed of the group of localized waves (also known as wavepacket) with the mean "carrier" energy E. At the edges of the Brillouine zone with the maximum absolute energy $|E| = \pi/4$, the group velocity is zero and the respective steady-state solutions are circularly polarized modes $(1, \pm i)$. This is not surprising, since exclusively for such modes, the walk becomes invariant under axial rotation of the set-up and thus its distribution has to be static. In contrast, the region around the center of the 1$^{\text{st}}$ BZ $k = 0$ can be well approximated by a Dirac-like relativistic energy:

$$E(k)_\pm = \pm\frac{|k|}{\sqrt{2}} + O(k^3), \tag{1.24}$$

describing a massless quasiparticle and quasiantiparticle with the effective speed of light $c = 1/\sqrt{2}$, which is also the maximum possible group velocity in the system. Interestingly, this velocity is still 30% smaller than the principal upper limit of the velocity, which is 1 position per 1 time step. The rapidly moving solutions in the center of the BZ possess linearly polarized states $(1 \pm \sqrt{2}, 1)$, which are aligned in parallel and perpendicularly to the principal axis of the half-wave phase retarder. Despite the suppressed value of the speed of light, the relativistic quasienergy dispersion is a signature of photons propagating in free space. Thus, in analogy with periodic crystals in Solid State Physics, we can interpret the forbidden gap and the group velocity slow-down at the edges of the BZ as photon's dispersion on the periodic spatiotemporal lattice. Indeed, a closer look at the group velocity in Fig. 1.3b shows that the group velocity dispersion $E''(k)$, which accounts for spatial spreading of a wavepacket with time, is maximum for the almost static waves, while it keeps the shape of
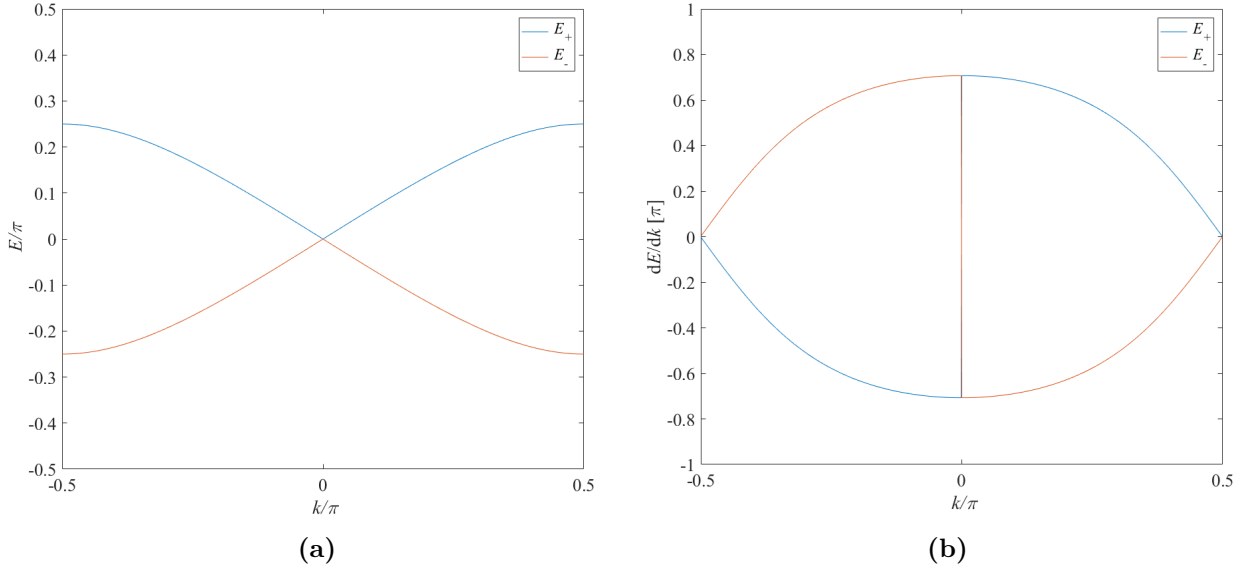
9

Figure 1.3: (a) The first Brillouine zone of the band structure for Hadamard Walk. (b) Group velocities, derived for the respective upper (blue) and lower (red) band.

initially localized rapidly moving waves unchanged for very long propagation times.

Note, that the diaganalization procedure demonstrated above is equivalent to a canonical Bogoliubov transformation of photon's annihiliation and creation operators, which, although not necessary in the Schrödinger picture of a single photon used so far, can nevertheless be introduced for a coherent electromagnetic wave with many photons, exhibiting an equivalent quantum walk dynamics [46], via second quantization of the field and by treating beam splitters in the Heisenberg picture.

Finalizing this section, we use the extended wave eigensolutions and eigenenergies of the walk in order to calculate standard deviation of the walker's position starting from a single lattice site n after m time steps:

$$\sigma_V^m = \sqrt{\langle n, V | \hat{U}^\dagger \hat{n}^2 \hat{U} | n, V \rangle - \langle n, V | \hat{U}^\dagger \hat{n} \hat{U} | n, V \rangle^2}, \tag{1.25}$$

where for simplicity we consider only the vertically polarized component, which is 1 for all k values and for both bands. Rewriting the position state in terms of vertically polarized normalized components of the Bloch eigenmodes and representing the evolution and position operators in momentum space, we obtain:

$$|n, V\rangle = \frac{1}{\sqrt{2\pi}} \int_{-\pi}^{\pi} e^{ikn} |k, V\rangle \, dk, \tag{1.26}$$

$$\hat{U} = \int_{-\pi}^{\pi} (e^{iE_- m} |k\rangle_- \langle k|_- + e^{iE_+ m} |k\rangle_+ \langle k|_+) dk, \tag{1.27}$$

$$\hat{n} = -i\frac{\mathrm{d}}{\mathrm{d}k}. \tag{1.28}$$

Further, neglecting interference effects between the lower and the upper band, one can come

up with the following analytical expression:

$$\sigma_V^m = m\sqrt{1 - \frac{1}{\sqrt{2}}} \approx 0.5412m. \tag{1.29}$$

Hence, the spreading speed of the Hadamard Walk is constant. Note, that a half of the spreading speed gives a rough estimation of the average group velocity, which is around 40% slower than the previously calculated maximum speed $c \approx 0.71$. This is expected result since the initially localized wave being a delta-like signal occupies the entire Brillouine zone in the reciprocal space, including the dispersion regions. Nevertheless, we observe a drastic speed enhancement compared with classical random walks, that eventually allows for an exponential speedup of Quantum Walk based algorithms compared with their classical counterparts [47].

1.2.2 1D walk of a two-component pseudospin

In this section, we discuss one-dimensional DQW, which in contrast to Hadamard Walk does not involve the genuine internal space, polarization, but instead deals with a local spatial degree of freedom, formed by the two previously mentioned complementary sublattices. In other words, the coin operator is not rotating the polarization state, but instead it rotates the two-component vector, formed by the localized wave components approaching the node from the left and the right side on the spatiotemporal lattice. Therefore, the dimensionality of the input and ouput states of the coin has to necessarily coincide with the number of sublattices, which in turn is predefined by the global topology of the network and has nothing to do with any internal degree of particle's freedom. Despite this fundamental difference, in sec. 1.4 we will see that the band structure of the new one-dimensional walk being introduced can be continuously deformed with a periodic potential into the one of the Hadamard walk, owing to the same underlying network topology of both DQWs. As already mentioned, in order to implement the polarization-insensitive walk of a photon, one needs a coin with two input and two output ports. The natural choice is based on polarization-insensitive beam splitters, arranged in a pyramid array as it was first proposed by Bouwmeester [27]. In this regard, the half-wave plate and the beam displacer at each position are replaced by an optical 50/50 beam splitter. Each beam splitter splits photon's wavefunction into two equal parts. The part travelling in the same direction as the incoming wave is transmitted by the beam splitter, while the one that is perpendicular to the incoming wave can be referred to as the reflected wave. In accordance with Fresnel equations based on Maxwell theory, an electromagnetic reflected wave acquires $\pi/2$ phase shift with respect to the transmitted one. The same value is valid in case of the DQW of a single photon as one can infer from the correspondence principle, holding for the quantum and classical electromagnetic descriptions of a beam splitter (see for example [48]). Consequently, the Coin operator reads

$$\hat{C} = \frac{1}{\sqrt{2}} \begin{pmatrix} 1 & i \\ i & 1 \end{pmatrix}, \tag{1.30}$$

which, in contrast to the Hadamard Coin, possess the mirror symmetry as one can easily check using the eq. (1.15). This is a direct consequence of a mirror symmetric design of optical beam splitters. On the other hand, the Shifter $\hat{S}$ remains the same as in eq. (1.15).

A general state at a time step m can be expressed as

$$\psi^m = \sum_n (l_n |l\rangle + r_n |r\rangle) \otimes |n\rangle = \sum_n \binom{l_n}{r_n} |n\rangle , \tag{1.31}$$

where n are positions of the beam splitters, $|l\rangle$ and $|r\rangle$ are the basis internal states that propagate to the left and to the right neighboring position, respectively. The complex vector $(l, r)^{\mathrm{T}}$ is often called pseudospin, emphasizing that physically it is not related neither to a fermionic spin-$\frac{1}{2}$, nor to the photon's helicity, although it has the same vectorial form.

In what follows, accounting for the same network topology of the Hadamard and the pseudospin walk, we perform again the diagonalization procedure for the double-step stroboscopic evolution matrix of the latter, in order to find the corresponding dispersion relation and the resulted band structure. Subsequently, we come up with two following bands:

$$E_\pm(k) = \pm\frac{1}{2} \arccos \frac{\cos 2k - 1}{2} \tag{1.32}$$

and the associated Bloch eigenvectors

$$|k\rangle_\pm = \begin{pmatrix} e^{ik}(\sin k \mp i\frac{\sqrt{2\cos 2k - 6}}{2}) \\ 1 \end{pmatrix} \sum_{n\in\mathbb{Z}} e^{-i2kn} |2n\rangle , \tag{1.33}$$

where again we chose, without loss of generality, to start the walk from the sublattice with even positions. Quasienergies and related group velocities in the first BZ are plotted in Fig. 1.4. One can see that, in contrast to the Hadamard Walk, here the photon experience dispersion on the spatiotemporal lattice mainly in the central region of the BZ, where the group velocity is small. On the other hand, the linear dispersion at the edges of the BZ resembles the dynamics of a free particle. Note, that the symmetric $(1, 1)^{\mathrm{T}}$ and anti-symmetric pseudospins $(1, -1)^{\mathrm{T}}$ of the steady-state Bloch modes with $k = 0$ are also eigenmodes of the maximally localized system, consisting of one single beam splitter with reflecting or periodic boundary conditions at the neighboring lattice knots. However, such a localization of the steady-state solutions down to one polarization rotating element is not possible for the Hadamard Walk, because there one needs at least two positions in order to accommodate the full wave cycle at $k = \pi/2$. Moreover, unlike in the Hadamard Walk, the rapidly moving waves of the pseudospin walk at the edges of the BZ are elliptically polarized, i.e. $|k\rangle_\pm \sim (i(1 \pm \sqrt{2}), 1)^{\mathrm{T}}$.

Also, note that the forbidden energy gap appears now in the center of the BZ, thus resembling an insulator's band structure for electrons in Solid State Physics. The half of the energy gap $\pi/4$ is associated with the effective rest energy of the quasiparticle (quasiantiparticle) residing in the upper (lower) band. As a result, the dynamics of the massive quasiparticle and antiparticle around their ground states can be approximated by the Schrödinger-like non-relativistic Hamiltonian:

$$E_\pm = \pm\frac{\pi}{4} \pm \frac{k^2}{2} + O(k^4) \approx mc^2 + \frac{k^2}{2m}, \tag{1.34}$$

where the effective mass and the effective speed of light can be derived from the kinetic and the rest energy as 1 and $\sqrt{\pi/2}$, respectively. Finally, calculations of the standard deviation σ^m and the spreading speed using the same approximations as in the previous subsection deliver us exactly the same result as for the Hadamard Walk. This implies that despite the
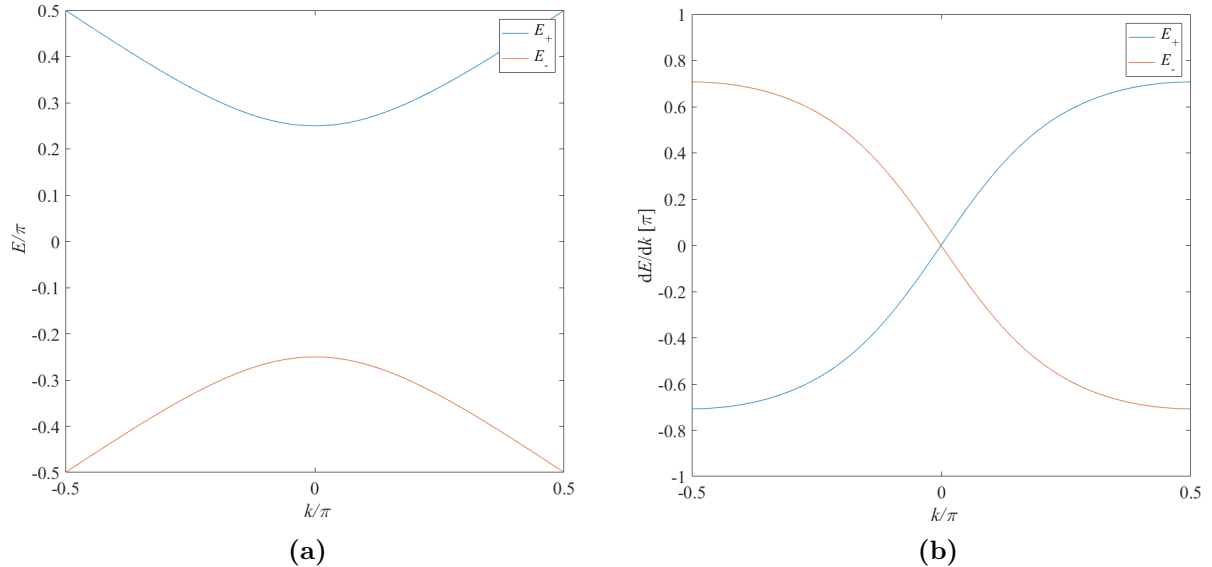
Figure 1.4: (a) The first Brillouine zone of the band structure for the pseudospin walk. (b) Group velocities, derived for the respective upper (blue) and lower (red) band.

non-relativistic dynamics around the ground state, the average dynamics over the entire band structure holding for a maximally localized state is the same for both walks. Afterwards, we will see that one walk can be continuously transformed into another by applying an appropriate phase modulation, and therefore the walks are equivalent to each other from a topological perspective, although their underlying optical elements and internal degrees of freedom are physically distinct.

1.2.3   2D walk of a four-component pseudospin

So far we have studied quantum walks on the simplest one-dimensional chain. A natural extension of the model would be to two spatial dimensions. It is clear already that multiple arrays of equally oriented beam splitters, although being in total a two-dimensional structure, will lead to the unidirectional 1D DQW, described above. Therefore, to make the walk truly two-dimensional we rotate every second beam splitter by 90° as shown in Fig. 1.5a. One can see that there are four complementary sublattices, corresponding to four different types of knots as illustrated in Fig. 1.5b. We can distinct four pseudospin components $(u, l, d, r)^{\mathrm{T}}$ entering the sublattice A, formed by "blue" and "green" knots and indicated by the red square in the figure, and four other components $(u, l, d, r)^{\mathrm{T}}$, entering the sublattice B, comprising "purple" and "yellow" knots. Thus, the full evolution description would comprise in total 8 components, however, since simultaneously occupied sublattices never interact in the linear lattice and the sublattice (chiral) symmetry holds for the free walk (see sections 1.6 and 1.7 for details), one can, similarly to the 1D walks, effectively reduce the description of dynamics to the stroboscopic evolution of a four-component vector, occupying only one particular sublattice. Again, such a description is enough to capture the entire photon dynamics in the lattice. Note, that the probability flow direction is fixed by the arrows only for convenience, although time reversal symmetry of the system allows one to choose the opposite flow direction as well. Next, in order to simplify following calculations, we choose the diagonal position basis $n' = (n + p)/2$, $p' = (n - p)/2$, which is however not indicated in Figs. 1.5, and fix the sublattice A as a starting point of the evolution. Thus, the diagonal
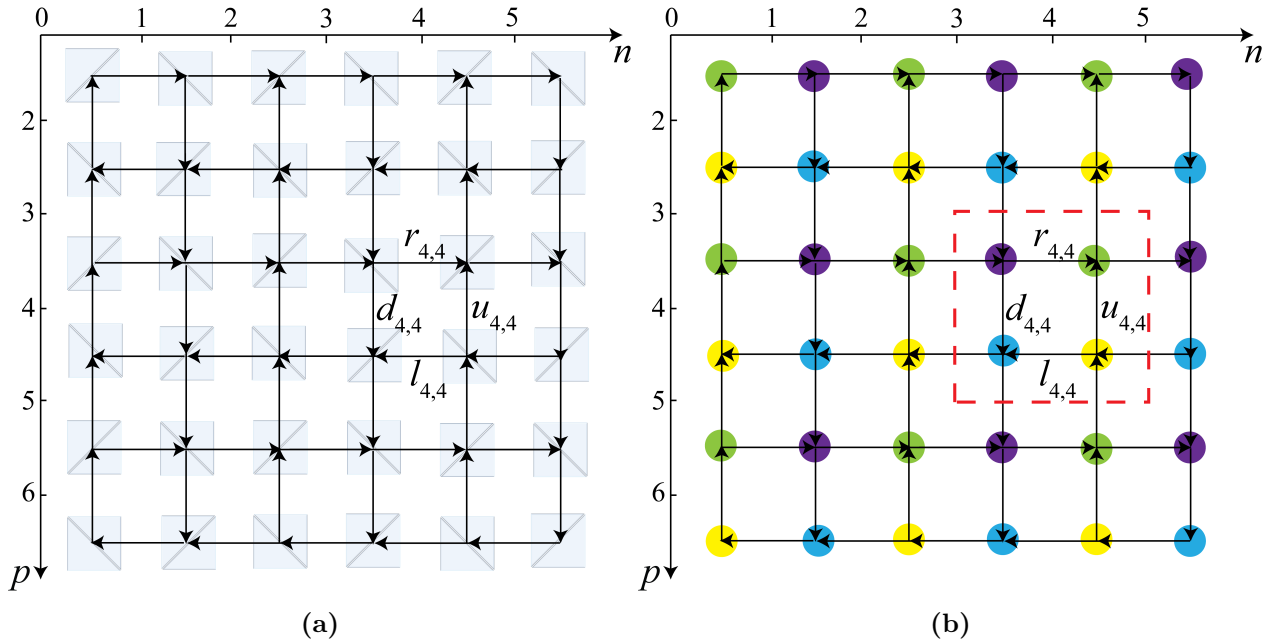
Figure 1.5: (a) Genuine two-dimensional network of beam splitters, obtained from the one-dimensional walk by rotating every second beam splitter by 90°. (b) The associated lattice with the elementary unit cell (red dashed square), containing four beam splitters. Particle's probability flow directions are predefined by the arrows for convenience.

position coordinates take only integer values on the sublattice and therefore we can write the generalized state as

$$|\psi\rangle = \sum_{n'\in\mathbf{Z}} \sum_{p'\in\mathbf{Z}} \begin{pmatrix} u_{n',p'} \\ r_{n',p'} \\ d_{n',p'} \\ l_{n',p'} \end{pmatrix} |n',p'\rangle. \tag{1.35}$$

The stroboscopic evolution operator with the doubled time period, mapping the sublattice A to itself, is the following:

$$\hat{U} = \hat{S}_{p'}\hat{C}_2\hat{S}_{n'}\hat{C}_1, \tag{1.36}$$

where $\hat{C}_1$ and $\hat{C}_2$ are Coin operators associated with beam splitters oriented along p' and n' axes, respectively. By looking at the lattice, it is easy to derive the operators' matrices as

$$\hat{C}_1 = \frac{1}{\sqrt{2}} \begin{pmatrix} 1 & i & 0 & 0 \\ i & 1 & 0 & 0 \\ 0 & 0 & 1 & i \\ 0 & 0 & i & 1 \end{pmatrix}, \tag{1.37}$$

$$\hat{S}_{n'} = \begin{pmatrix} |n'-1\rangle\langle n'| & 0 & 0 & 0 \\ 0 & |n'-1\rangle\langle n'| & 0 & 0 \\ 0 & 0 & |n'+1\rangle\langle n'| & 0 \\ 0 & 0 & 0 & |n'+1\rangle\langle n'| \end{pmatrix}, \tag{1.38}$$
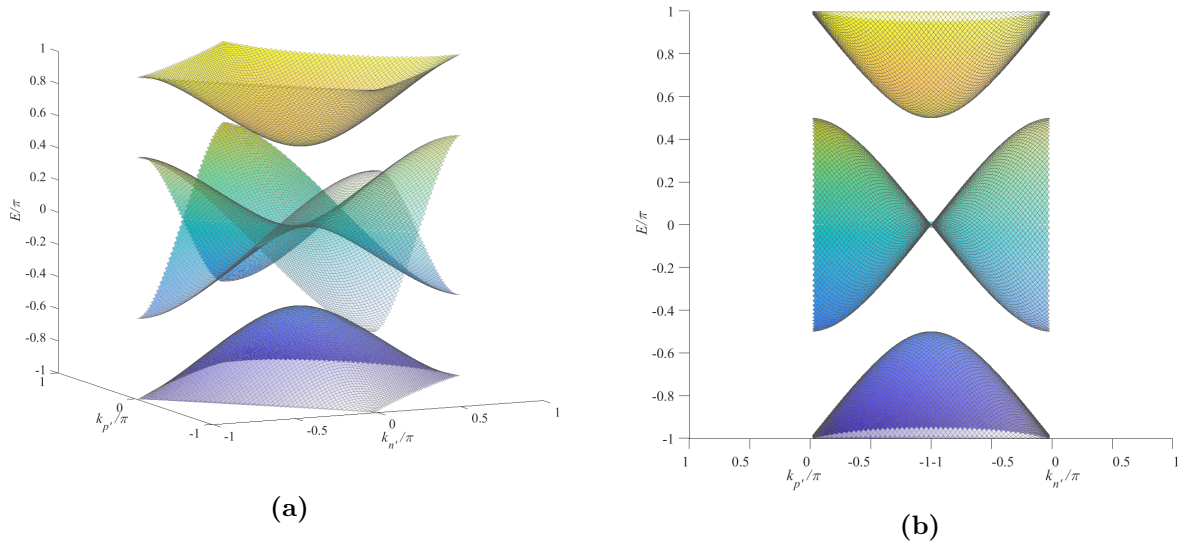
Figure 1.6: (a) Band structure of the four-component pseudospin walk, consisting of four bands. (b) Planar cross section of the band structure along the horizontal n or vertical p axis.

$$\hat{C}_2 = \frac{1}{\sqrt{2}} \begin{pmatrix} 1 & 0 & 0 & i \\ 0 & 1 & i & 0 \\ 0 & i & 1 & 0 \\ i & 0 & 0 & 1 \end{pmatrix} \tag{1.39}$$

$$\hat{S}_{p'} = \begin{pmatrix} |p'+1\rangle\langle p'| & 0 & 0 & 0 \\ 0 & |p'-1\rangle\langle p'| & 0 & 0 \\ 0 & 0 & |p'-1\rangle\langle p'| & 0 \\ 0 & 0 & 0 & |p'+1\rangle\langle p'| \end{pmatrix}. \tag{1.40}$$

Similarly to the one-dimensional walks, one can diagonalize the evolution matrix and eventually come up with the following four bands:

$$E_{1,\pm} = \pm \arccos\left(\frac{2\cos k_n \cos k_p - \sqrt{(\cos 2k_n - 3)(\cos 2k_p - 3)}}{4}\right), \tag{1.41}$$

$$E_{2,\pm} = \pm \arccos\left(\frac{2\cos k_n \cos k_p + \sqrt{(\cos 2k_n - 3)(\cos 2k_p - 3)}}{4}\right), \tag{1.42}$$

plotted within the first Brillouine zone, which is a square with a reduced size along the diagonal directions k'_n and k'_p, thus corresponding to the square unit cell of size 2×2 in real space. Note that the upper and lower bands degenerate at their bases $E = \pm\pi$ and in the vicinity of the center of the BZ, they describe two-dimensional Schrödinger-like dynamics of a non-relativistic massive particle and antiparticle, as follows from the approximation:

$$E_{1,\pm} = \pm\left(\frac{\pi}{2} + \frac{k_{n'}^2}{2} + \frac{k_{p'}^2}{2} + O(k_{n'}^4) + O(k_{p'}^4)\right). \tag{1.43}$$

This expression shows that the effective mass is equal to 1 and is the same as for the one-dimensional pseudospin walk. The rest mass differs, however it does not play any role for the walk dynamics. For the eigenvectors, we will not provide the general expressions as they are

cumbersome, but only mention that in the center of the BZ the pseudospins of the positive and the negative Schrödinger-like bands are $(1, 1, 1, 1)^\mathrm{T}$ and $(1, -1, 1, -1)^\mathrm{T}$, respectively. As one could expect for the array of beam splitters, the eigenmodes are composed of symmetric or anti-symmetric two-component wavefunctions.

In contrast, the intermediate two bands have one critical degeneracy point in the center of the BZ. In particular, the vicinity of this point exhibits quasi-one-dimensional Dirac-like linear divergence along the line $k_n = 0$ or $k_p = 0$, but in fact it has a form of a saddle point for each of the bands. Thus, these two bands are very different from degenerate Dirac cones of a massless relativistic particle. Further in sections 1.4 and 1.7, we will also reveal a very peculiar topology of this two-dimensional network. Nevertheless, the planar cross sections of the intermediate bands as shown in Fig. 1.6b resemble the band structure of the one-dimensional Hadamard Walk.

Finally, rigorous calculations of the standard deviation of a delta-like signal in both position coordinates n' and p' deliver exactly the same result as in the one-dimensional cases

$$\sigma_{n',p'} = m\sqrt{1 - \frac{1}{\sqrt{2}}} \approx 0.5412m, \qquad (1.44)$$

where however m accounts for one complete evolution step. This evidence together with previous remarks on the band structure supports the idea that the two-dimensional four-component walk combines some key dynamical features of its one-dimensional counterparts introduced earlier, even though the global network topology, as will be shown later, becomes very different when every second beam splitter in the original array is rotated by $90°$.

1.2.4 2D relativistic walk of a two-component pseudospin

Previously, we have shown that a two-dimensional walk can inherit basic dynamical features of its more primitive counterpart in one dimension, despite a more complex network topology of the former. However, it turns out that there is another two-dimensional network, in which the change of dynamics and dispersion properties become more dramatic, while the topology is essentially preserved. Given the same type of beam splitters with two input and two output ports, one can think of only one additional nearest-neighbour configuration of the two-dimensional network, namely the one where the input (output) ports enter (exit) a beam splitter from two opposite sides, i.e. from the left- and the right-hand side or from above and below. Obviously, this configuration is not realizable with conventional free-space beam splitters, because the light should enter or exit a splitter from mutually perpendicular directions. One could, for example, implement some additional free-space manipulations with the optical path, however nowadays it is convenient to use fiber optics to guide the light in a required direction. In particular, one can use in-fiber optical beam splitters to create the network, as demonstrated in Fig. 1.7a. Note, however, that in this scheme one should presume ideally equal fiber lengths and identical beam splitters, in order to ensure interferometric stability and coherence for the walk. These requirements are practically not feasible for a large number of optical elements, and a special experimental technique of time-multiplexing will be therefore discussed in that regard.

In contrast to the previous 2D four-component pseudospin walk, the network under consideration comprises two types of splitters: the "green" and the "blue" ones, branching their output (input) ports along axis p (n) and n (p), respectively. Consequently, the lattice consists of two sublattices, each hosting one pseudospin with two components, u and d

or l and r. Note, that in contrast to other 1D and 2D DQWs, where one sublattice can be transformed into another one by an appropriate discrete sublattice translation, in this case one has to additionally rotate the sublattice by 180°. Nevertheless, using the same argumentation of decoupled sublattices as in all previous systems, we can stroboscopically describe the walk just by a two-component pseudospin, occupying one particular sublattice. Again, in presence of the sublattice symmetry mentioned earlier and to be revealed in sections 1.6 and 1.7, such a description does not lose any features of the full instantaneous description and therefore it reflects the entire photon dynamics in the lattice.

In what follows, we can assume without loss of generality that, for example, only horizontal ports l and r are occupied at the initial time step, and then only these components are being traced during the evolution in a stroboscopic manner. Note, that in contrast to the four-component walk, the unit cell here is a rhomb. Also, we chose to numerate the positions for each component (port) based on the beam splitter it is heading to, as illustrated by the arrows in Fig. 1.7a. Consequently, a summation of the components over all elementary unit cell yields the description of an arbitrary state

$$|\psi\rangle = \sum_{\mathrm{mod}\,\frac{n+p}{2}\in\mathbb{Z}} \begin{pmatrix} l_{n,p} \\ r_{n,p} \end{pmatrix} |n,p\rangle. \tag{1.45}$$

The evolution matrix, as a consecutive action of the "green" and the "blue" beam splitters, then reads

$$\hat{U} = \hat{S}_n \hat{C} \hat{S}_p \hat{C}, \tag{1.46}$$

with

$$\hat{C} = \frac{1}{\sqrt{2}} \begin{pmatrix} 1 & i \\ i & 1 \end{pmatrix}, \tag{1.47}$$

$$\hat{S}_n = \begin{pmatrix} |n-1\rangle\langle n| & 0 \\ 0 & |n+1\rangle\langle n| \end{pmatrix}, \tag{1.48}$$

$$\hat{S}_p = \begin{pmatrix} |p-1\rangle\langle p| & 0 \\ 0 & |p+1\rangle\langle p| \end{pmatrix}. \tag{1.49}$$

Similarly to all previous DQWs, we perform diagonalization of the evolution matrix based on a Bloch wave ansatz and come up with the following two bands

$$E_{\pm} = \pm \arccos\left(-\sin k_n \sin k_p\right). \tag{1.50}$$

In Fig. 1.7b we demonstrate the band structure also beyond the first Brillouine zone, having a rhombus shape, in order to clearly show the genuine two-dimensional Dirac-like cones at the edges of the BZ. In this regard, the upper and the lower band around the Dirac-like degeneracy points with $E = 0$ are associated with the dynamics of a massless relativistic particle and antiparticle, respectively. If we square the energies and approximate them around these points neglecting the higher order terms, then we get the following cone's
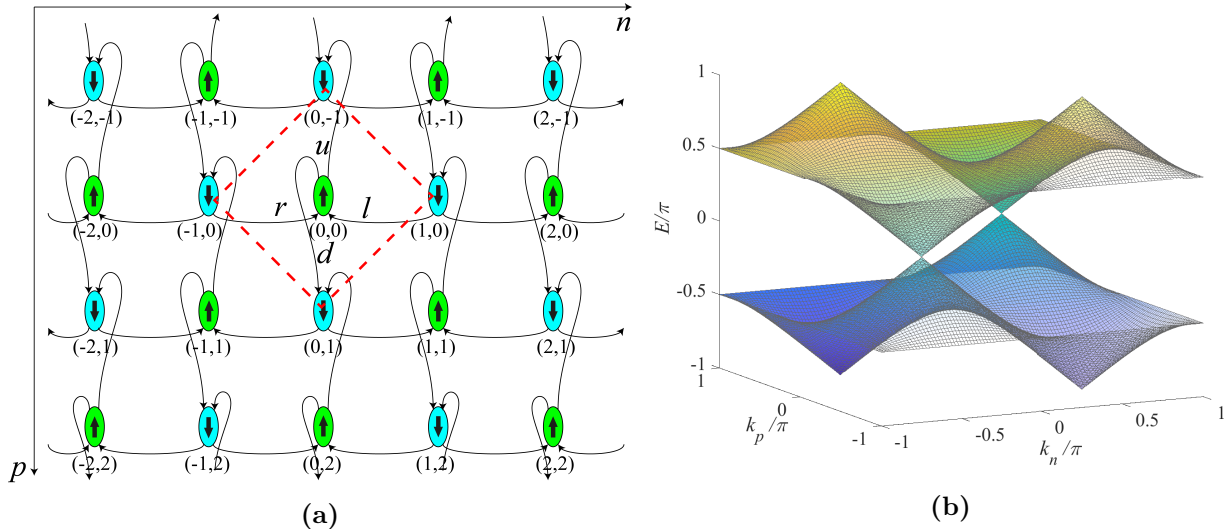
Figure 1.7: (a) One more two-dimensional network with output (input) ports branching from (into) a beam splitter in mutually opposite directions. The usage of fiber optical components is very convenient here. The elementary unit cell is denoted with the red dashed square. (b) Band structure of the corresponding two-component pseudospin walk, comprising two bands.

equations:

$$E_+^2 \approx \left(k_n \pm \frac{\pi}{2}\right)^2 + \left(k_p \mp \frac{\pi}{2}\right)^2, \tag{1.51}$$

$$E_-^2 \approx -\left(k_n \pm \frac{\pi}{2}\right)^2 - \left(k_p \mp \frac{\pi}{2}\right)^2. \tag{1.52}$$

The absence of the energy gap corresponds to a massless particle as mentioned above. The speed of light and the group velocity are equal to 1 as it can be derived from the relativistic energy $E^2 = k^2 c^2$. Since one evolution time step moves a particle along the diagonal direction, the principal speed limit is effectively $\sqrt{2}$ diagonal positions per one time step. Thus, similarly to the Hadamard Walk, the effective speed of light is again smaller than the principal limit by the factor of $\sqrt{2}$. Nevertheless, the higher dimensionality of the Dirac-like cones eventually leads to an overall speed enhancement of a maximally localized wavepacket. Indeed, the estimated standard deviation of an initially delta-localized photon shows the spreading speed enhancement of about 10% compared to the Hadamard and other walks, namely

$$\sigma_{n,p} = m\sqrt{1 - \frac{2}{\pi}} \approx 0.6028m \tag{1.53}$$

This speed enhancement is mainly limited by the quasimomenta regions, that are far enough from the Dirac points and where the dispersion on the lattice becomes considerable. Also, note that the irrational number π appears in the expression as an indicator of circular symmetry of Dirac-like cones in the reciprocal space.

1.2.5 One remark on Light and Quantum Walks

Finalizing the chapter, we would like to emphasize one simple yet important aspect, that has been mentioned earlier few times. Namely, the coherence property of a single photon is pre-

served by a monochromatic coherent light wave with many photons, allowing for a coherent walk of the latter in a network of beam splitters, provided the network is interferometrically stable. A large number of photons ensures that quantum fluctuations of the electromagnetic field are much smaller, than the amplitude of the field. Moreover, such a coherent walk of an optical pulse with a slowly varying envelope is equivalent to the quantum walk of a single photon with a well-defined start time, which is due to mathematically identical transformations of electric fields and photon annihilation operators (in the Heisenberg picture) by optical beam splitters. This aspect is very well known from previous studies on classical Light and single photon Quantum Walks [10, 46]. In future, we will always use the notion Discrete Quantum Walk (DQW) interchangeably for both cases, except in the chapter 3, where nonlinear Kerr effects take place only on the classical level and thus the DQW implies exclusively the Light Walk.

1.3 Time-multiplexed analogues of the Discrete Quantum Walks

So far, we have shown that various DQW networks are possible in both one and two dimensions even with one constituent element, namely with the 2×2 optical beam splitter. However, a straightforward experimental implementation of the networks inevitably meets a number of difficulties.

In particular, a perfect wave interference, a necessary requirement for the coherent walk, would require that all possible optical paths branching from some splitter n and eventually converging to a splitter n' within a certain number of time steps M, should be mutually equal up to an error δ_M, that has to be much smaller than half of the optical wavelength $\lambda/2$. This requirement is quite demanding since the error is scaled up with the number of time steps as $\delta \sim M$. For example, in order to realize the 1D DQW for $M = 100$ time steps, the error should be less than $\lambda/200$, which is in the nanometer range for a visible light. Moreover, for such a walk starting from a single position, one would require a pyramid of $(M + 1) \times M/2 = 5050$ beam splitters. Two-dimensional networks are even more demanding, since the number of elements grows cubically with time and the optical paths in two dimensions become twice longer. Thereby, the straightforward implementation of large-scale DQWs is very impractical and another technique called time-multiplexing is required to resolve these problems.

1.3.1 One-dimensional case

The time-multiplexing has been widely used for the one-dimensional case in both quantum [33] and coherent light experiments [29]. In this method, periodicity of the structure allows one to loop a single beam splitter on itself as shown in Fig. 1.8 for the one-dimensional case. It is very convenient, although not essential, to use optical fibers and in-fiber 50/50 couplers for that. One can see, that the simple looping of the system with symmetric left and right optical paths does not allow for the position changes since both pseudospin components become trapped just to one position. As mentioned already before, this system can capture only the steady-state localized wavepacket of the extended network. However, the situation becomes different in case of asymmetric loop lengths as indicated by different colors in Fig. 1.8. In this way, assuming an incident wave splits into two pieces at the beam splitter, the resulted two waves propagating through the left and the right fiber loops will meet
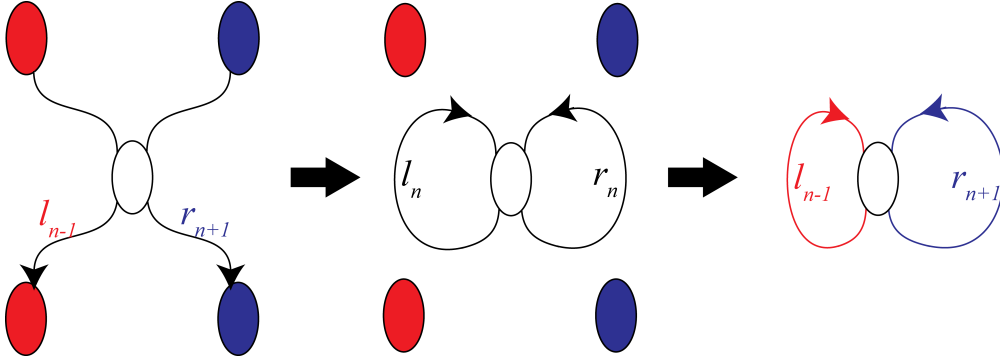
Figure 1.8: The core idea of time-multiplexing. Firstly, we introduce periodic boundaries by looping one beam splitter onto itself. Secondly, an artificial spatial dimension is created via mutual length asymmetry between the left (red) and the right (blue) loop and resulting temporal delays between circulating pulses.

again at the beam splitter but with a certain temporal delay ΔL proportional to the loop length difference. If the waves are infinite in time, then they will mutually interfere every new round-trip along the loops. This way, no walk dynamics can be established, because the waves will be constantly mixing. However, if the temporal width of the waves is smaller than the temporal delay associated with the loop length difference, the waves will not overlap and thus each of them can be identified by their individual arrival times at the splitter. Taking the moment of the initial split as a reference point, the temporal wavepackets (pulses) will arrive at the splitter again at the times

$$T_{l,r} = \frac{n_{\text{fiber}}(\bar{L} \mp \Delta L/2)}{c}, \tag{1.54}$$

where $\bar{L}$ is an average length of the short and the long loop, c is the speed of light and n_{fiber} is the effective group index of the fiber. If the evolution continues further, the pulses get doubled every time step, so that all pulses can be described by their arrival times as

$$T_{l_n,r_n} = \frac{n_{\text{fiber}}(m\bar{L} \mp n\Delta L/2)}{c}, \tag{1.55}$$

where n is odd (even) at odd (even) time steps m. It is clear now, that each pulse can be identified by its arrival time at the beam splitter instead of the spatial and temporal positions in the original network. In particular, a pulse energy that always propagates through the long (short) loop would correspond to the walker going right (left) on the original lattice. If two optical paths simultaneously branching from the beam splitter comprise the same amount of round-trips through the long and the short loop, but implemented in a different order, they will necessarily cross each other and will lead to interference. The pulse width, despite of being shorter than the temporal delay, should still contain a considerable number of optical cycles for the slowly varying envelope approximation to apply, so that one can avoid pulse broadening. Another limitation is that the number of available time steps and positions is restricted to $\bar{L}/\Delta L$ and $2\bar{L}/\Delta L$, respectively, because thereafter the train of pulses of two adjacent round-trips will begin to overlap with each other.

1.3.2 Two-dimensional cases

In two dimensions, the network becomes more complex and one elementary unit cell of the lattice covers more than one beam splitter. As a result, the time-multiplexed system gets more complicated as well, as illustrated in Fig. 1.9a and 1.9b for the four-component and two-component pseudospin walk, respectively. It turns out, that significant topological distinctions of the four-component pseudospin network from the one-dimensional one does not allow for a straightforward time-multiplexing due to a lack of interferometric stability. In contrast, the 2D two-component pseudospin walk is interferometrically amenable via time-multiplexing with two beam splitters. Further on, we clarify this question specifically for each of the walks.

Four-component pseudospin walk

Regarding the walk of a four-component pseudospin, let us first concentrate on the single lattice site $n = 3, p = 4$ (see Fig. 1.5b), comprising four beam splitters of different colors and having a clockwise circulating particle flow. This unit cell can be considered as elementary in the stroboscopic evolution picture, introduced earlier. Therefore, in accordance with the principle of time-multiplexing, one has to loop those four beam splitters on itself, as shown in the Fig. 1.9a. Note, that in this figure, for a greater clarity, we changed the position assignments to the four pseudospin components r, d, l and u, so that every four-component pseudospin with a uniformly defined position (n, p) has now counter-clockwise or clockwise sense of rotation of the power flow. It is worth mentioning, that instead of the clockwise rotating pseudospin, one could alternatively choose the counter-clockwise rotating or outward oriented (like saddle points) unit cell as the pseudospin of the time-multiplexed set-up. Thus, in total there are four alternative time-multiplexed schemes, but all of them are equivalent to the original spatiotemporal walk.

Next, comparing the original and the time-multiplexed network, one can observe two principal types of round-trips in the latter scheme:

1. The first type comprises the clockwise trajectory $u_{n,p} \to r_{n,p} \to d_{n,p} \to l_{n,p}$ and the counter-clockwise path $u_{n,p-1} \to l_{n-1,p} \to d_{n,p+1} \to r_{n+1}, p$, each of which covers four splitters. Since in both spatial and time-multiplexed systems these trajectories correspond to a closed loop, a pulse traveling along one of them will come back to its initial point in both systems. For that property, we shall call this type a "genuine" round-trip. The "genuine" round-trips correspond to one evolution period of the walk, meaning that they advance the pulse to the next time step. It implies that the total length of the internal fiber pieces $u_{n,p}, r_{n,p}, d_{n,p}$ and $l_{n,p}$ of the time-multiplexed network should be equal to the total sum of the external fiber pieces $u_{n,p-1}, l_{n-1,p}, d_{n,p+1}$ and r_{n+1}, p, because otherwise the temporal period will depend on the taken path and thus interferometric stability of the walk will be violated.

2. In contrast, when a light pulse travels, for example, along $r_{n,p}$ and $r_{n+1,p}$ thus covering two beam splitters, physically it comes back to its initial point only in the time-multiplexed network, while in the original lattice it makes one position to the right. According to the time-multiplexing technique, the pairwise length difference between the outer pieces $l_{n-1,p}$ and $r_{n+1,p}$ ($u_{n,p-1}$ and $d_{n,p+1}$) encode position shift of the walker along n (p). In addition and in contrast to the one-dimensional walk, the inner pseudospin components $u_{n,p}, r_{n,p}, d_{n,p}$ and $l_{n,p}$ form an internal pseudospin space, which is essentially also a spatial dimension in the original lattice. This space does
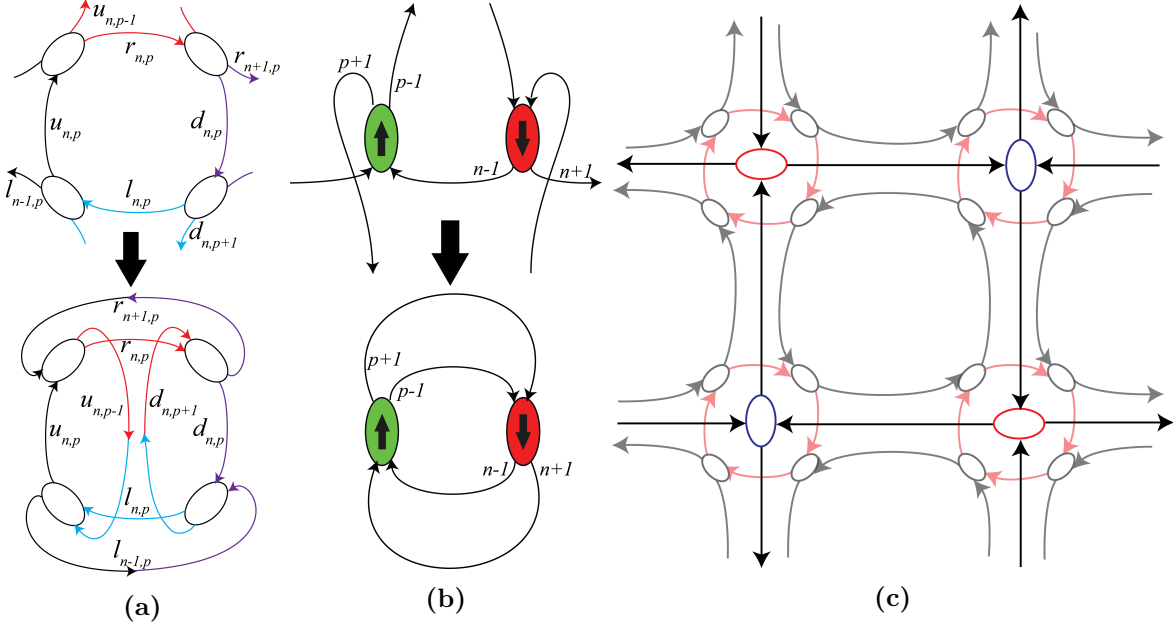
21

Figure 1.9: (a) One of the four trials of time-multiplexing of the four-component pseudospin walk. The minimum number of required beam splitters is four. (b) Time-multiplexed two-component pseudospin walk, comprising two connected beam splitters. (c) The lower complexity of the time-multiplexed two-component pseudospin walk stems from effectively zero size of the pseudospins, linked to the knots of the network (blue and red colored beam splitters). The four-component pseudospins (red rotating arrows) of another walk, in contrast, exhibit internal dynamics, i.e. the walker can locally circulate in one single lattice site.

not need to be particularly encoded by the time-multiplexing, because it is invariably transferred from the original lattice, i.e. the pseudospin remains genuinely spatial. In order to avoid an overlap between pulses of adjacent time steps, all the pairwise length differences of the corresponding outer loops should be much smaller than the "genuine" round-trip length. Also, to avoid an overlap between adjacent positions n (or p), one has to make the length difference between corresponding u and d pieces (or r and l) much smaller, than the mismatch between r and l (or u and d) pieces.

Mentioned already in the first paragraph, the requirement of exactly equal total lengths of the inner and outer loops makes the time-multiplexed set-up practically nonamenable to an interferometric alignment and stabilization. Therefore, such straightforward time-multiplexing is neither scalable nor viable for experimental purposes. To ultimately improve the scheme, one could think of a more advanced time-multiplexing technique, involving, for example, counter-propagating directions [49] or additionally exploiting the polarization degree of freedom [50]. We, however, do not expand further on this system, since the experimentally realized in our group 2D time-multiplexed platform is based on its one-dimensional "topological relative", as we discuss further on.

Two-component pseudospin walk

It is interesting, that complexity of the time-multiplexed network can be reduced without compromising the spatial dimensionality, but instead at the cost of a reduced pseudospin dimension. Indeed, earlier introduced two-dimensional walk with the two-component pseudospin is equivalent to a looped system of only two beam splitters and four fiber pieces as

shown in Fig. 1.9b. In contrast to the four-component pseudospin time-multiplexed system, where one had to introduce in total five scales (three time scales for the originally spatial and temporal dimensions, and two spatial scales for the internal pseudospin dimension), here only three time scales is enough since the two-component pseudospins reside on the knots of the network and thus have effectively a spatial size of zero, in contrast to the four-component vertices or, alternatively, saddle points. We illustrate this principal difference between the two- and four-component pseudospins in Fig. 1.9c.

In that regard, the length difference between lower two fibers ΔL_n encodes shifts along the horizontal axis, while the mismatch between the upper two fibers ΔL_p corresponds to one step of the position p. One round-trip in the time-multiplexed scheme, from one beam splitter to another and back, is not "genuine", because in the original lattice it does not bring the walker to its original position. Instead, two such round-trips covering all four fiber pieces is required to make one genuine round-trip in the spatial lattice. A pulse, making the genuine round-trip should subsequently cover all fiber loops of the time-multiplexed set-up (see Fig. 1.9b), i.e. it will thereby acquire the total time delay of $\bar{T} = \frac{n}{c}(L_{p-1} + L_{p+1} + L_{n+1} + L_{n-1})$, where n is the effective group index of the fibers, c is speed of light in vacuum and the Ls are corresponding fiber loop lengths. If the pulse will instead propagate through one fiber piece twice, it will be shifted by two positions in the corresponding direction. Summarizing these observations, one can get the following time delay with respect to the starting point of the pulse after a multiple number of round-trips m:

$$T = m\bar{T} + n\Delta T_n + p\Delta T_p, \tag{1.56}$$

where T_n and T_p are time delays associated with the length differences between the lower and the upper two fibers, respectively. Assuming the time delay ΔT_n is larger than ΔT_p, the overlap between pulses of adjacent positions n will take place after the occupied number of vertical positions exceeds $p_{max} = \Delta T_n/\Delta T_p$. Similarly, the overlap between two adjacent time steps will take place if more than $n_{max} = \bar{T}/(2\Delta T_n)$ horizontal positions are occupied.

1.4 Continuous band structure deformation via periodic potential

In this section, we will consider the possibility of a continuous tuning of the band curvature and of the forbidden gap's size. This can be done by introducing a periodic static potential on the lattice, which in turn is doable in the time-multiplexed fiber loop set-ups via dynamically controlled phase modulation, introduced in the chapter 2. While an impact of such band structure deformations on symmetries of the DQWs will be discussed in the chapter 1.6, from now on we will mostly concentrate on changes in the dynamical features of the DQWs.

1.4.1 One-dimensional walk

First, we consider a phase modulation pattern for the one-dimensional lattice, which was introduced by Martin Wimmer in [51]. This potential pattern appears as a static periodic array of alternating potential wells and barriers. Since the on-site acquired phase φ has to exchange every time step between the two pseudospin components l and r, the elementary unit cell comprises two time steps and two positions as illustrated in Fig. 1.10. Note, that here odd and even modulation time steps are unambiguously linked to the respective sublattices
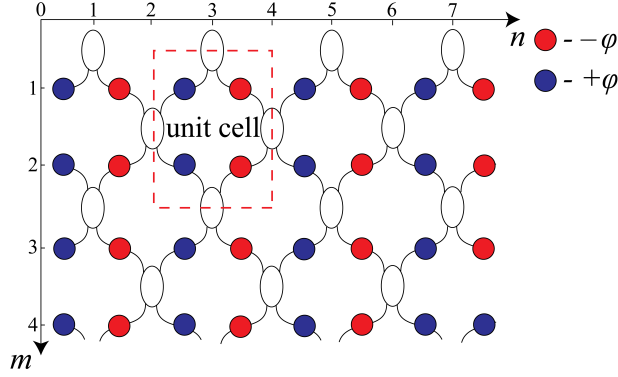
Figure 1.10: Static periodic potential pattern, applied via phase modulation of the wavefunction.

and therefore the effective evolution operator has to necessarily contain two time steps, unlike its unmodulated counterpart. In this regard, the evolution operator reads

$$\hat{U} = \hat{\Phi}(-\varphi)\hat{S}\hat{C}\hat{\Phi}(\varphi)\hat{S}\hat{C}, \tag{1.57}$$

where the Shifter $\hat{S}$ and the Coin $\hat{C}$ had been introduced earlier and

$$\hat{\Phi}(\phi) \stackrel{\text{def}}{=\!=} \begin{pmatrix} e^{i\varphi} & 0 \\ 0 & e^{-i\varphi} \end{pmatrix} = e^{i\varphi\hat{\sigma}_z} \tag{1.58}$$

is the phase shift operator, acting homogeneously on internal pseudospin states. It is also expressed in terms of the Pauli matrix σ_z responsible for rotation of a pseudospin in its associated Hilbert space. The phase operators $\hat{\Phi}(\varphi)$ and $\hat{\Phi}(-\varphi)$ are commuting with the Shifter and thus together with the Coin $\hat{C}$, they form the generalized Coin

$$\hat{C(\varphi)} = \hat{\Phi}(-\varphi)\hat{C}\hat{\Phi}(\varphi) = \frac{1}{\sqrt{2}} \begin{pmatrix} 1 & ie^{-2i\varphi} \\ ie^{2i\varphi} & 1 \end{pmatrix}, \tag{1.59}$$

where the coin of the pseudospin walk is chosen as a reference point.

Accounting for the doubled time period, we represent the fundamental states of the system in terms of extended Floquet-Bloch waves and diagonalize the evolution matrix in order to find the dispersion relations. Thereby, we come up with two bands for the Hadamard Walk

$$E_\pm = \pm\frac{1}{2}\arccos\frac{\cos 2k + \cos 2\varphi}{2} \tag{1.60}$$

and for the pseudospin walk

$$E_\pm = \pm\frac{1}{2}\arccos\frac{\cos 2k - \cos 2\varphi}{2}, \tag{1.61}$$

where the prefactor $1/2$ is kept for conformity with the results in subsection 1.2.2. Both band structures are demonstrated in Fig. 1.11 for different potential heights φ. It is easy to see that the periodic potential allows one to bridge these two walks, turning one walk into another at $\varphi = \pi/2$ via continuous deformation of the bands. Such a deformation, however, does not deliver the same eigenvectors for both walks even though their band structures are identical. This is because the generalized coin $\hat{C}(\varphi)$ still preserves mirror symmetry of the
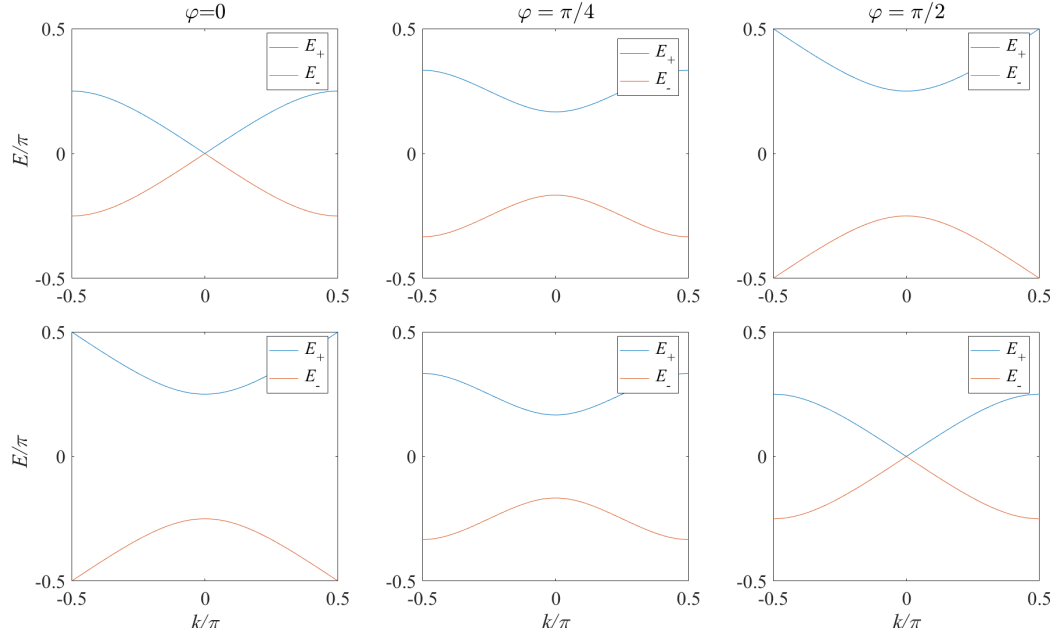
Figure 1.11: Various amplitudes φ of phase modulation lead to deformations of the band structure and change sizes of the band gaps. The upper and the lower row correspond to the Hadamard and the pseudospin walk, respectively.

beam splitter and consequently the eigenspectrum of pseudospins should obey this symmetry as well, while the polarization eigenmodes do not. So, the macroscopic dynamics of both walks can be made identical via the periodic potential despite that their microscopic features remain different.

Finally, we can approximate the generalized band structure around the center of the BZ $k = 0$. Thus, choosing the pseudospin walk as a reference point, we make the Taylor expansion for all φ except $\pi/2$ and come up with the nonrelativistic Schrödinger-like Hamiltonian

$$E_\pm \approx \pm\frac{1}{2}\arccos\left(\frac{1 - \cos 2\varphi}{2}\right) \pm \frac{k^2}{2\sqrt{1 - \frac{(1-\cos 2\varphi)^2}{4}}} + O(k^4), \tag{1.62}$$

while at the special point $\varphi = \pi/2$ we get relativistic energies of the Hadamard Walk for a massless particle

$$E_\pm = \pm\frac{k}{\sqrt{2}} + O(k^3). \tag{1.63}$$

The first constant term of the Schrödinger-like energy is associated with the rest energy of a quasiparticle and quasiantiparticle.

$$E_r = \pm\frac{1}{2}\arccos\frac{1 - \cos 2\varphi}{2}, \tag{1.64}$$

while the second term is associated with a non-relativistic kinetic energy $E_k = \pm k^2/2m$, so

that the effective mass can be derived as

$$m = \pm\sqrt{1 - \frac{(1 - \cos 2\varphi)^2}{4}} = \sin 2E_r. \qquad (1.65)$$

Interestingly, the mass-energy equivalence equation $E_r = mc^2$ holds only for small enough rest energies $|E_r| \ll \pi/4$ with the constant effective speed of light $c = 1/\sqrt{2}$, but as the band gap $2|E_r|$ becomes larger, the increase of the effective mass slows down until the mass reaches its limit of ± 1 at $E_r = \pm\pi/4$. Recalling that the mass is also the inverse of the group velocity dispersion $1/E''(k)$, we conclude that dispersion-free localization of an immobile wavepacket is impossible in the lattice and thus a photon can not behave as a heavy classical immobile particle. However, in the relativistic Hadamard limit the dispersion is zero and thus the localized photon can move without spreading only as a relativistic massless particle. This is in agreement with the intrinsic relativistic nature of photons.

Further on, we will examine the topological charge of the pseudospin at the degeneracy point at $k = 0$ and $\varphi = \pi/2$. To do so, we shall consider the celebrated Berry phase [52], which is a phase difference acquired by a complex wavefunction of a quantum system under its adiabatic evolution along a closed loop in a parametric space of the Hamiltonian. This phase has a topological origin. In particular, the famous result derived by Berry himself in [52] and by Aharonov and Anandan in [53] is that the electron's spin placed in a magnetic field and evolving adiabatically along a closed loop C around a degeneracy point of the Hamiltonian acquires the Berry phase $\gamma(C) = \pm s\Omega(C)$, where $\Omega(C)$ is the solid angle that the loop C subtends at the degeneracy, while $s = 1/2$ is the spin angular momentum of the electron. A more relevant example, however, is the two-component local pseudospin of an electron in the graphene layer modeled as a hexagonal lattice with tight-binding approximation [54]. In this case, the pseudospin eigenvector $|\psi(k_x, k_y)\rangle$ of a fixed band circumventing a closed loop around the Dirac two-fold degeneracy point in the two-dimensional reciprocal space (k_x, k_y) will acquire the Berry phase $\gamma = \pm s2\pi = \pi$, where the solid angle is now replaced by the planar angle of 2π and the quantum number s coincides with the fermionic spin-1/2 despite the wavefunction $|\psi(k_x, k_y)\rangle$ is not the genuine spin of the electron.

To find the Berry phase, we consider the Hamiltonian operator $\hat{H}(k, \varphi)$ of the one-dimensional walk, which periodically spans the two-dimensional parametric space (k, φ) and which can be found via the generalized Euler's formula

$$\hat{H}(k, \varphi) = E(k, \varphi)[(e_x(k, \varphi)\hat{\sigma}_x + e_y(k, \varphi)\hat{\sigma}_y + e_z(k, \varphi)\hat{\sigma}_z], \qquad (1.66)$$

$$\hat{U}(k, \varphi) \stackrel{\text{def}}{=} e^{i\hat{H}(k,\varphi)} = \cos E(k, \varphi)\hat{I} + i\sin E(k, \varphi)[e_x(k, \varphi)\hat{\sigma}_x + e_y(k, \varphi)\hat{\sigma}_y + e_z(k, \varphi)\hat{\sigma}_z], \qquad (1.67)$$

where $\pm E(k, \varphi)$ are quasienergies of the upper and the lower band given in eq. (1.61), $\hat{\sigma}$ are Pauli matrices and $\vec{e}(k, \varphi)$ is a real-valued vector normalized to unity and representing the eigenvectors on the so-called Bloch or Poincare sphere. Straightforward derivation of the vector $\vec{e}(k, \varphi)$ yields:

$$\vec{e} = \frac{1}{2\sin E(k, \varphi)} \begin{pmatrix} \cos 2\varphi + \cos 2k \\ \sin 2\varphi - \sin 2k \\ \sin 2\varphi + \sin 2k \end{pmatrix}. \qquad (1.68)$$

In order to describe a closed loop around the two-fold degeneracy point $k = 0$, $\varphi = \pi/2$, we use the parametrization $k = R\cos\alpha$ and $\varphi = \pi/2 + R\sin\alpha$, where R is a fixed radius of the

loop and α runs from 0 to 2π. Substituting these parameters into the unit vector and taking the limit $R \to 0$, we obtain

$$\vec{e} \approx \begin{pmatrix} 0 \\ -\cos(\alpha - \pi/4) \\ -\sin(\alpha - \pi/4) \end{pmatrix}, \tag{1.69}$$

which remains a unit vector. Note that, as expected, the Hamiltonian takes the relativistic form $\pm(\vec{e}\vec{\sigma})k/\sqrt{2}$ around the degeneracy point. Recalling the definitions of the Pauli matrices, we consider the eigenvalue problem $\vec{e}|\psi\rangle_\pm = \pm|\psi\rangle_\pm$ and obtain the following eigenmodes:

$$|\psi\rangle_\pm = \begin{pmatrix} i\frac{\cos(\alpha+\pi/4)\pm 1}{\sin(\alpha+\pi/4)} \\ 1 \end{pmatrix}. \tag{1.70}$$

In order to resolve the uncertainty $0/0$ at $\alpha - \pi/4 = \pm\pi/2$, we perform a series of standard trigonometric transformations and come up with the following expressions:

$$|\psi\rangle_+ = \begin{pmatrix} i\cos\left(\frac{\alpha}{2} + \frac{\pi}{8}\right) \\ \sin\left(\frac{\alpha}{2} + \frac{\pi}{8}\right) \end{pmatrix}, \quad |\psi\rangle_- = \begin{pmatrix} -i\sin\left(\frac{\alpha}{2} + \frac{\pi}{8}\right) \\ \cos\left(\frac{\alpha}{2} + \frac{\pi}{8}\right) \end{pmatrix}. \tag{1.71}$$

The half angle $\alpha/2$ indicates that the eigenmodes acquire the Berry phase of π in the associated Hilbert space upon the full cycle around the Dirac point in the parametric space. Therefore, the two-component pseudospin around that degeneracy point behaves as a fermionic spin-$\frac{1}{2}$. Further in section 1.7, it will become clear that this result is not generic, because time-reversal transformation of the pseudospin at another Dirac point ($k = \pi/2, \varphi = 0$) oppositely indicate an integer spin (bosonic) behaviour and thus one can anticipate the Berry phase of 0 at that point. One can also expect the same ambiguity for the helicity in the Hadamard Walk. Moreover, we presume that the fermion-boson duality of the pseudspin is essentially the reason, why correlated photons can exhibit both quantum statistics in the same system [37, 41]. Moreover, an intermediate behaviour with fractional exchange statistics is possible in continuous quantum walks [55]. The fact that even helicity does not behave as a genuine integer spin is related to the absence of photon's mass and of a rest frame. In electromagnetism, this fact is translated to the absence of longitudinal electromagnetic waves in homogeneous media.

1.4.2 Two-dimensional walks

In this subsection, we study earlier introduced two-dimensional walks in presence of a static periodic potential. The associated phase pattern has a period of 2 in both spatial directions and is illustrated in Figs. 1.12a and 1.12b. Note, that the elementary unit cell becomes larger for the modulated lattice in accordance with the pattern period. Similarly to the one-dimensional case, this phase potential can be effectively imposed by a spatially uniform time-dependent phase modulation, as we will show further below. Such a modulation in temporal domain perfectly works in time-multiplexed walks as well, with a voltage-driven phase modulator incorporated into one of the loops. In addition, we will show that, unlike the pseudospin and Hadamard Walks, the two-component and four-component 2D walks can not be topologically connected via the continuous band structure deformation. This is
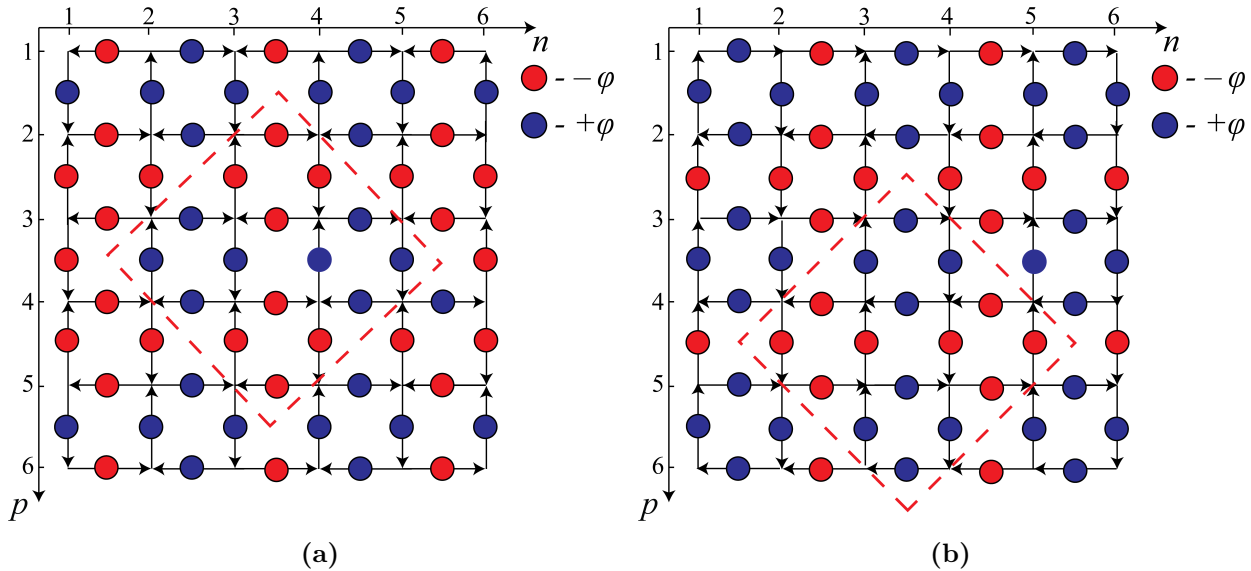
Figure 1.12: The two-dimensional periodic potential, applied to the two-component (a) and four-component (b) pseudospin walk. The elementary unit cell (red dashed squares) is twice bigger in both diagonal directions, compared to the ones of the unmodulated walks.

due to a completely different topologies of these two networks. In other words, the phase potential by no means is able to decouple the four-component pseudospin into a pair of independent two-component pseudospins. Below, we will briefly consider both of the 2D walks, namely transformations of the band structures, effective masses and Berry phases acquired by pseudospins in the reciprocal space around degeneracy points.

Two-component spin

In order to effectively realize the periodic potential pattern of the two-component 2D walk (see Fig. 1.12a), we can again use the stroboscopic evolution operator driving a two-component pseudospin located in one of the two sublattices. With this assumption, an unambiguous self-consistent temporal phase modulation becomes possible with the doubled time period as follows

$$\hat{U} = \hat{\Phi}(-\varphi)\hat{S}_p\hat{C}\hat{\Phi}(-\varphi)\hat{S}_n\hat{C}\hat{\Phi}(\varphi)\hat{S}_p\hat{C}\hat{\Phi}(\varphi)\hat{S}_n\hat{C}. \tag{1.72}$$

The reader can explicitly check that this modulation indeed corresponds to the spatial pattern in Fig. 1.12a. Solving the eigenvalue problem for the evolution operator yields the following band structure:

$$E_\pm = \pm \arccos \frac{\cos 2k_n \cos 2k_p - \cos^2 2\varphi - \cos 2\varphi(\cos 2k_n + \cos 2k_p)}{2}, \tag{1.73}$$

which is also depicted in the upper row of Fig. 1.13. We see that the Dirac cone initially situated at the edge of the first BZ reappear again in the central point at $\varphi = \pi/2$. Intermediate values of the phase amplitude lead to a parabollic Schrödinger-like valley, as seen in Fig. 1.13 at $\varphi = \pi/4$. More specifically, the eigenergies around the central point of the BZ can be approximated for all phase amplitude values except $\varphi = \pi/2 + \pi N$, where $N \in \mathbb{Z}$,
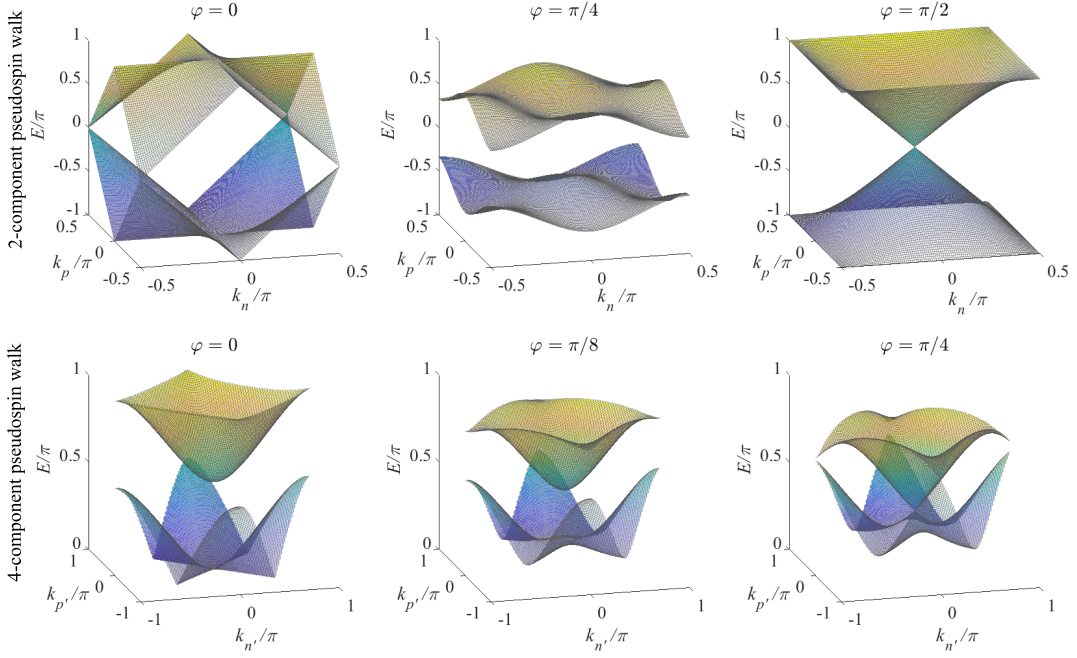
Figure 1.13: Two-dimensional band structures of the walks with various amplitudes φ of the phase modulation.

namely

$$E_\pm \approx \pm E_r(\varphi) \pm \frac{k_n^2 + k_p^2}{2m(\varphi)}, \tag{1.74}$$

$$E_r(\varphi) \stackrel{\text{def}}{=\!=} \arccos \frac{\sin^2 2\varphi - 2\cos 2\varphi}{2}, \tag{1.75}$$

$$m(\varphi) \stackrel{\text{def}}{=\!=} \frac{|\sin E_r|}{4 + 2\sqrt{2 - 2\cos E_r(\varphi)}}. \tag{1.76}$$

Note, that the effective mass is increasing linearly with the rest energy only for very small values with the effective speed of light $c = \sqrt{E/m}$ equal to 2, which coincides with value found in the relativistic unmodulated lattice (one position per one time step). However, in contrast to the one-dimensional lattice, the growth of the effective mass does not only slow down, but also turns backward starting from $E_r = 2\varphi = \arccos \sqrt{5} - 2 \approx 0.42\pi$. This is the critical phase amplitude, below which the central Schrödinger-like valley is disappearing and another one at the edge of the BZ starts forming.

Next, similarly to the case of the unmodulated lattice, the case $\varphi = \pi/2$ delivers the Dirac-like cone with a degeneracy point in the center of the BZ (see upper row of the Fig. 1.13)

$$E_\pm \approx \pm 2\sqrt{k_p^2 + k_n^2}, \tag{1.77}$$

which describes a massless relativistic quasi particle and antiparticle. Note, that none of the phase amplitude values reconstructs the band structure of the four-component walk. Finalizing this paragraph, we make sure that the pseudospin indeed has the topological quantum number of $1/2$ inherent to fermions, by calculating the Berry phase. To do so,

we fix φ to $\pi/2$ and encircle the Dirac point in the two-dimensional reciprocal space. First, expressing the evolution operator $\hat{U} = \exp\left(i\hat{H}\right)$ in terms of Pauli matrices and applying the generalized Euler's formula, we can find the Hamiltonian as a superposition of Pauli matrices $\hat{H} = |E_{\pm}|(\vec{e}, \vec{\hat{\sigma}})$. We will not provide here the full version of the vector $\vec{e}$ due to its lengthy expression, but will only consider its form in the vicinity of the Dirac point at $\varphi = \pi/2$, when the parametric radius of the closed path $r \overset{\text{def}}{=\!=} \sqrt{k_n^2 + k_p^2}$ tends to zero. Then, we get

$$\vec{e} \approx \begin{pmatrix} 0 \\ -\cos(\alpha) \\ \sin(\alpha) \end{pmatrix}, \tag{1.78}$$

where $\alpha \overset{\text{def}}{=\!=} \arctan k_p/k_n$. This expression is very similar to eq. (1.69) and therefore it will again lead to the topological Berry phase of π. Thus, the two-component pseudospin indeed behaves as a fermionic spin, however we anticipate an integer spin for $\varphi = \pi/2$ to $k_{n,p} = \pi/2$, because similarly to the one-dimensional walks the classification in section 1.7 also reveals bosonic topological classes.

4-component spin

Proceeding with the same periodic potential, we consider now the four-component pseudospin walk. It turns out that the effective temporal phase modulation corresponding to this potential takes only one elementary time step. Indeed, assuming without loss of generality that four-components of only one position per one unit cell are excited simultaneously, we can write the evolution operator as follows:

$$\hat{U} = \hat{\Phi}(-\varphi)\hat{S}_{p'}\hat{C}_2\hat{\Phi}(\varphi)\hat{S}_{n'}\hat{C}_1. \tag{1.79}$$

Note, that the full evolution period is not able to bring a local pseudospin back to its initial position within the unit cell, which would require at least two evolution periods. Next, as many times before we solve the eigenvalue problem for the evolution operator in order to find the four-fold band structure

$$E_{1,\pm} = \pm\arccos\frac{2\cos k_{n'}\cos k_{p'} - \sqrt{6 + 2\cos 4\varphi - 4\cos 2k_{n'} - 4\cos 2k_{p'} + 4\cos^2 k_{n'}\cos^2 k_{p'}}}{4},$$
$$\tag{1.80}$$

$$E_{2,\pm} = \pm\arccos\frac{2\cos k_{n'}\cos k_{p'} + \sqrt{6 + 2\cos 4\varphi - 4\cos 2k_{n'} - 4\cos 2k_{p'} + 4\cos^2 k_{n'}\cos^2 k_{p'}}}{4}.$$
$$\tag{1.81}$$

A further analysis shows that none of the potential values allows one to decompose the four-component pseudospin into a pair of independent spinors. More specifically, it is not possible to represent the evolution matrix as a block matrix formed by two non-zero 2-by-2 matrices on the main- or on the off-diagonal. The upper two bands are illustrated in the lower row of the Fig 1.13, while lower bands are always symmetric to the upper ones with respect to zero. We see, that the half-period of the phase modulation is $\pi/4$ instead of $\pi/2$. Also, a striking difference to the two-component 2D walk, where the band structure continuously transforms from one Dirac point to another one, is that here the transition takes place between the lines of two-fold degeneracy at $\varphi = 0$ for $E = 0$ and $E = \pm\pi$ and the single degeneracy point in

the center of the BZ at $\varphi = \pi/4$. Further below, we will see that this point is in fact not of the Dirac type. Firstly, let us concentrate on the parabolic valleys that appear if $\varphi \neq N\pi/4$ with $N \in \mathbb{Z}$. The vicinity of the central point can be approximated as

$$E_{1,2,\pm} \approx \pm E_{r1,2} \pm \frac{k_{n'}^2 + k_{p'}^2}{2m_{1,2}}, \tag{1.82}$$

$$E_{r1,2} \overset{\text{def}}{=} \arccos \frac{1 \mp |\cos 2\varphi|}{2}, \tag{1.83}$$

$$m_{1,2} \overset{\text{def}}{=} \mp \sin E_{r1,2}\left(2 - \frac{1}{\cos E_{r1,2}}\right). \tag{1.84}$$

We see, that the effective mass of the intermediate bands (index 2) is negative and it's modulus is growing linearly only for small values of E_r with the effective speed of light $c = 1$ ($m \approx -E_r/c^2$). It is important to note, however, that in the degeneracy limit $\varphi = 0$, the saddle point is very different from the Dirac point and thus the relativistic terms such as speed of light are not applicable here. Instead, in this point the branching type becomes hyperbolic, namely

$$E_{2,\pm} \approx \pm \frac{k_{n'}^2 - k_{p'}^2}{2}, \tag{1.85}$$

where the negative and positive energy bands are now redefined as two mutually mirrored hyperbolic surfaces. Note, that the central saddle singularity point is not the lowest ground state energy, but is only a "ferry" point for the quasiparticle, i.e. the latter can reach even lower energy values on the hyperbolic surface.

Next, a detailed numerical numerical analysis shows that eigenmodes corresponding to the degeneracy lines crossing in the saddle point are approachable by the eigemodes of the surrounding non-degenerate region. Indeed, the degenerate set of eigenmodes at $\varphi = 0$ is easy to derive analytically as

$$\psi_{k_p=0} = a \begin{pmatrix} i(e^{-i\sqrt{2}k_n} - 1) \\ -1 \\ 0 \\ 1 \end{pmatrix} + b \begin{pmatrix} -e^{-i\sqrt{2}k_n} \\ 0 \\ 1 \\ 0 \end{pmatrix}, \tag{1.86}$$

$$\psi_{k_n=0} = a \begin{pmatrix} 0 \\ -e^{-i\sqrt{2}k_p} \\ 0 \\ 1 \end{pmatrix} + b \begin{pmatrix} -1 \\ i(e^{-i\sqrt{2}k_p} - 1) \\ 1 \\ 0 \end{pmatrix}, \tag{1.87}$$

where a and b are arbitrary complex numbers, k_n and k_p are quasimomenta oriented along the horizontal and vertical axes of the lattice, respectively. These basis eigenvectors, even though they are generally non-orthogonal, span a two-dimensional subspace in the four-dimensional Hilbert space, which coincides with the subspace spanned by the two intermediate bands when the quasimomentum is approaching the degeneracy line. Although we fail to show this limit analytically, numerical calculations indicate that this is indeed the case. Thus, the situation is analogous to the Dirac cone of the two-component walk, where the degenerate eigenmode spans over the entire two-dimensional Hilbert space (since only two bands are present) and the surrounding eigenmodes approach their own limit, which depends on the half of the azimuth angle $\alpha/2$. To finalize the case of $\varphi = 0$, we emphasize that the energy

splitting from the degeneracy line locally obeys a linear dependency with respect to the infinitesimal tangential momentum component $\delta k_\alpha = k_r \delta \alpha$, where we define $k_n \overset{\text{def}}{=\!=} k_r \sin \alpha$ and $k_p \overset{\text{def}}{=\!=} k_r \cos \alpha$. Indeed, the eq. (1.85) in the vicinity of any degeneracy line reads

$$E_{2,\pm} \approx \pm k_r^2 \delta \sin 2\alpha \approx \pm k_r \delta k_\alpha, \tag{1.88}$$

where the radial component k_r is fixed during the infinitesimal rotation by the angle $\delta \alpha$.

Next, while increasing further the phase amplitude and thus the rest energy, the growth of the effective mass quickly slows down and turns backward until the mass of zero is reached again in the degeneracy point $E_r = \pi/3$, corresponding to $\varphi = \pi/4$. Around this point, the effective mass again behaves linearly with respect to E_r, namely $m \approx 3(E_r - \pi/3)$ with the effective speed of light $c = 1/\sqrt{3}$. Note, that this value of c is much smaller than the principal speed limit for the lattice, which is 2 positions per evolution period (always along the horizontal or the vertical direction). Moreover, the bands approximation around the degeneracy points

$$E_{1\pm} \approx \pm \sqrt{\left(\frac{\pi}{3}\right)^2 + \frac{2\pi}{3\sqrt{3}} k_r + (\frac{1}{3} + \frac{2\pi}{9\sqrt{3}}) k_r^2}, \tag{1.89}$$

$$E_{2\pm} \approx \pm \sqrt{\left(\frac{\pi}{3}\right)^2 - \frac{2\pi}{3\sqrt{3}} k_r + (\frac{1}{3} + \frac{2\pi}{9\sqrt{3}}) k_r^2}, \tag{1.90}$$

shows that for small radial momenta the leading term (besides the rest energy $\pi/3$) enters the expressions as a square root of k_r. This is in a great contrast to the relativistic Dirac cone, where the energy splitting is linear with respect to k_r. On the other hand, the square-root law is typical for the second-order exceptional points, which are inherent to non-Hermitian systems [56–60]. Another indication of an exceptional point is the coalescence of eigenmodes into one state while approaching this point. However, in our case a detailed numerical analysis shows that exactly defined eigenmodes of the degeneracy points $E_\pm = \pm\frac{\pi}{3}$ exist and are isolated from the set of surrounding eigenvectors, namely in the degeneracy points $E_\pm = \pm\frac{\pi}{3}$ the eigenvectors read

$$|\psi\rangle_\pm = \begin{pmatrix} \pm i\sqrt{3} \\ -i \\ -i \\ 1 \end{pmatrix}. \tag{1.91}$$

These vectors are not approached by their surrounding eigenmodes as the radial momentum k_r tends to 0. In fact, the four-dimensional Hilbert space spanned by the four non-degenerate bands is abruptly collapsing into these two eigenvectors when the degeneracy point is set exactly. This situation is similar to the exceptional point, where the collapse of dimensionality takes place as well, but in the latter case the eigenmode coalescence is approached smoothly.

Finally, we probe the topological Berry phase of the four-component pseudospin. While the saddle point can not be encircled with a closed trajectory without crossing the degeneracy lines, the square root degeneracy point enables such a closed loop in the reciprocal space. Hence, we further evaluate Berry phase near this point at $\varphi = \pi/4$. Analytic derivation of the eigenmodes lead to extremely cumbersome expressions, therefore we prefer to find the modes numerically. So, in Fig. 1.14 we demonstrate the moduli and phases of the u, r, d
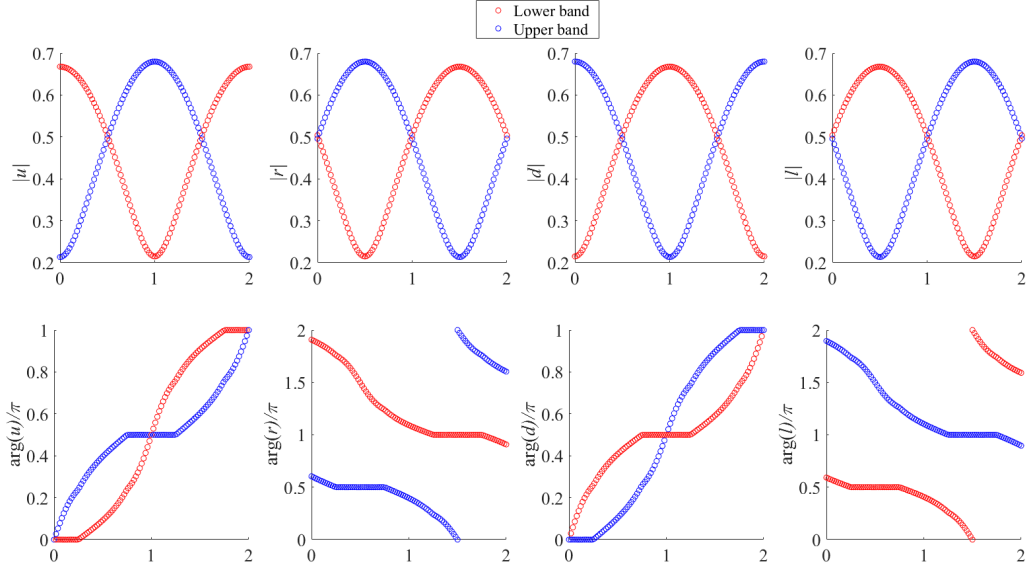
Figure 1.14: Moduli (upper row) and phases (lower row) of pseudospin components of the eigenmodes, encircling the degeneracy point at $k = 0$ and $\varphi = \pi/4$.

and l components of the eigenmodes, encircling the degeneracy point with the parametric angle $\alpha \in (0, 2\pi)$ and the fixed radius $k_r = 0.01\pi$, which was chosen arbitrarily. None of the curves show a singularity and therefore, there are no uncertainties to be resolved. This implies that Berry phase can be estimated directly from the plots, namely all the curves have period of 2π, what corresponds to the Berry phase of zero. In other words, the four-component pseudospin behaves as a spin-1 particle, typically associated with a massive boson. Surprisingly, the topological classification in section 1.7 shows that this result is generic for the four-component pseudospin, meaning that it always behaves as an integer spin. Moreover, this is somewhat unusual result, because commonly a massive bosonic state corresponds to a three-component complex vector. An archetypical example of such a state in photonics is illustrated by the three-component pseudspin-1 occurring in the Lieb photonic lattice [61], possessing two Dirac cones and additionally one flat band in between. In this example, the flat band is able to stop the light completely due to zero group velocity. However, we presume that this integer spin result for the four-component pseudospin should be closely related to the non-zero rest energy and the relatively slow effective speed of light, reached in the lattice, because topology of the localized pseudospin originates from global dynamical properties of the entire network.

1.5 Band structure deformation via periodically-driven coupling

Previously, we have introduced stationary periodic potentials via phase modulation. It has been shown that phase retardation can drastically change the band structure and the dynamics and continuously connect the Hadamard and pseudospin one-dimensional walk. Globally, it increased the parametric space of the Hamiltonian, what eventually enriches the topological diversity of the walks as will be shown later. Here, we briefly introduce another degree of freedom, that is a dynamical variation of the coupling between pseudospin components. This dynamical control is also possible in time-multiplexed set-ups, as will

be discussed in Chapter. From the perspective of photon dynamics, the coupling degree of freedom θ can completely decoupled some of the lattice knots and thus lead to a flat band in the reciprocal space, the effect not possible via phase modulation.

1.5.1   1D pseudospin walk

For the one-dimensional walk we introduce the following conservative coin with variable coupling θ

$$\hat{C}(\theta) = \frac{1}{\sqrt{2}} \begin{pmatrix} \cos\theta & i\sin\theta \\ i\sin\theta & \cos\theta \end{pmatrix}. \tag{1.92}$$

Note, the the relative phase is not changing and is fixed to $\pi/2$. The simplest coupling modulation within the doubled temporal periodicity of the stroboscopic Floquet system is the following

$$\hat{U} = e^{\frac{i\hat{H}}{2}} = \hat{\Phi}(-\varphi)\hat{S}\hat{C}(\theta_2)\hat{\Phi}(\varphi)\hat{S}\hat{C}(\theta_1), \tag{1.93}$$

where we also kept the periodic potential introduced in the previous chapter. Since the dynamical coupling does not increase the period further in time or space, we can apply the same Bloch ansatz as before and eventually derive the band structure as

$$\hat{E}_\pm = \pm\frac{1}{2}\arccos\left(\cos 2k \cos\theta_1 \cos\theta_2 - \cos 2\varphi \sin\theta_1 \sin\theta_2\right). \tag{1.94}$$

The upper band with various fixed coupling strengths θ_1, θ_2 and sweeping phase amplitude φ is shown in Fig. 1.15. The plots indicate that flat bands (in the momentum space) are possible, when at least one of the coefficients is set to full reflection ($\theta = \pm\pi/2$), corresponding to the trivial case of a trapped walker. In addition, the upper and lower bands degenerate at some Dirac points only if both couplings take one of the equilibrium values: $\pi/4$ or $3\pi/4$. Otherwise, the Hamiltonian is gapped. Finally, we observe the non-relativistic band approximation for the gapped system around $k = 0$

$$E_\pm \approx \pm E_r \pm \frac{k^2}{2m}, \tag{1.95}$$

$$E_r \overset{\text{def}}{=\!=} \frac{\arccos\left(\cos\theta_1 \cos\theta_2 - \cos 2\varphi \sin\theta_1 \sin\theta_2\right)}{2}, \tag{1.96}$$

$$m \overset{\text{def}}{=\!=} \frac{\sin 2E_r}{2(\cos 2E_r + \cos 2\varphi \sin\theta_1 \sin\theta_2)}, \tag{1.97}$$

which appropriately modifies the rest energy and the mass. The relativistic limit close to the Dirac points also remains valid for the gappless Hamiltonian:

$$\lim_{E_r \to 0} E_\pm = \pm k\sqrt{1 + \cos 2\varphi \sin\theta_1 \sin\theta_2} + O(k^3), \tag{1.98}$$

$$\lim_{E_r \to \frac{\pi}{2}} E_\pm = \pm\frac{\pi}{2} \mp k\sqrt{1 - \cos 2\varphi \sin\theta_1 \sin\theta_2} + O(k^3). \tag{1.99}$$
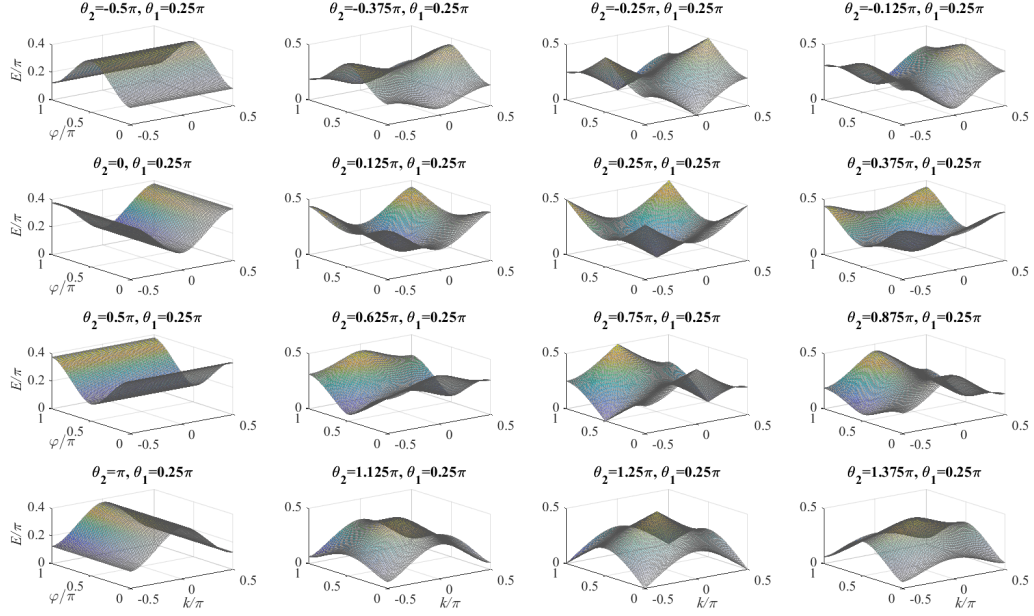
Figure 1.15: Band structures (only the positive band) of the one-dimensional walk with various coupling coefficients θ_1 and θ_2 and continuously sweeping amplitude of the phase modulation φ.

In order to find the Hamiltonian, we rotate the reference time frame of the Floquet stroboscopic evolution operator as

$$\hat{U}' = \hat{C}(\theta_1/2)\hat{U}\hat{C}(-\theta_1/2). \tag{1.100}$$

This permutation, which does not change the walk dynamics in the bulk, but can modify topological properties of the Hamiltonian, is very useful for finding a chiral (sublattice) symmetry of the system as will be demonstrated in section 1.6. Therefore, it is commonly called chiral symmetry time frame [62–64]. While the new reference frame does not change the band structure, it rotates eigenvectors of the Hamiltonian on the so-called Bloch sphere. Below we only provide the resulted expression:

$$\hat{H}' = |E_{\pm}|/(\vec{e'} \cdot \vec{\sigma}), \tag{1.101}$$

$$\vec{e'} \overset{\text{def}}{=\!=} \frac{1}{\sin 2|E_{\pm}|} \begin{pmatrix} \cos 2k \cos\theta_2 \sin\theta_1 + \cos 2\varphi \cos\theta_1 \sin\theta_2 \\ \sin 2\varphi \sin\theta_2 \\ \cos\theta_2 \sin 2k \end{pmatrix}. \tag{1.102}$$

1.5.2 2D two-component pseudospin walk

Next, we introduce the variable coupling to the two-dimensional walk of a two-component pseudospin in exactly the same way as

$$\hat{U} = \hat{S}_n \hat{C}(\theta_2) \hat{S}_p \hat{C}(\theta_1). \tag{1.103}$$

For simplicity and also for the educational reason that will be clear below, this time we disregard the phase modulation and find the band structure as

$$E_{\pm} = \pm \arccos\left(\cos k_n \cos k_p \cos(\theta_1 + \theta_2) - \sin k_n \sin k_p \cos(\theta_1 - \theta_2) \right). \tag{1.104}$$

35

Different realizations of the band structure are illustrated in Fig. 1.16, including the cases of
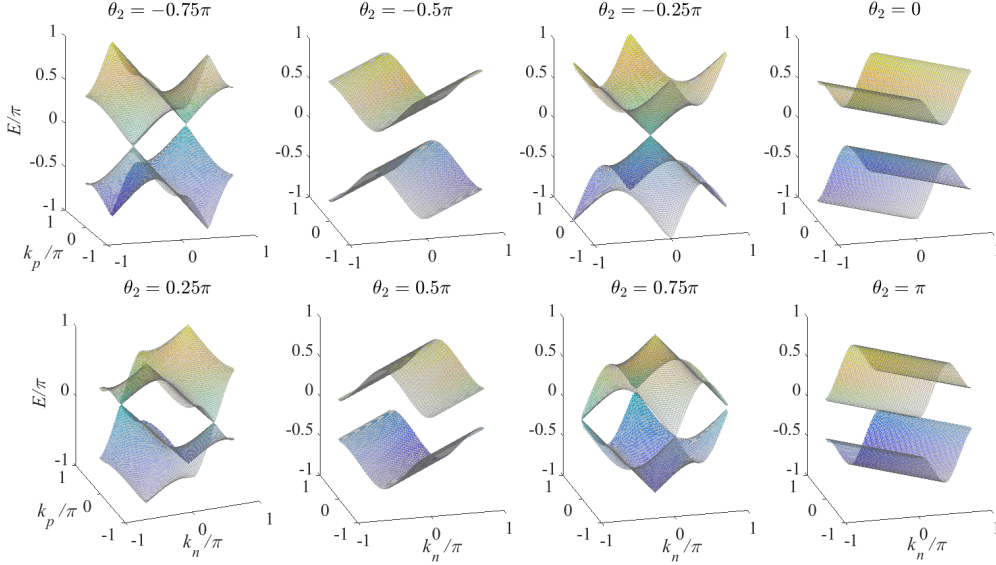

Figure 1.16: Band structures of the two-component pseudospin walk with various values of θ_2, while θ_1 is fixed to $\pi/4$.

quasi-1D flat bands along one of the diagonal directions. The latter implies that the walker is spatially confined in that direction. The gapless Dirac degeneracy points again occur if both couplings take the same or different equilibrium values $\pi/4$ and $3\pi/4$. The approximation around the (originally) saddle point at $k_{n,p} = 0$

$$E_\pm \approx \pm E_r \pm \frac{1}{2m}\left(k_p^2 + k_n^2 + 2k_p k_n \frac{\cos(\theta_1 - \theta_2)}{\cos E_r}\right), \tag{1.105}$$

$$E_r \overset{\text{def}}{=\!=} \theta_1 + \theta_2, \tag{1.106}$$

$$m \overset{\text{def}}{=\!=} \tan E_r \tag{1.107}$$

is now continuously bridged with the Dirac-like cones, appearing around this point at $\theta_1 - \theta_2 = \pi/2$, where however the approximation shows Schrödinger-like parabolic curve.

Again, applying the chiral symmetry time frame

$$\hat{U}' = \hat{C}(\theta_1/2)\hat{U}\hat{C}(-\theta_1/2) \tag{1.108}$$

we get the Hamiltonian as

$$\hat{H}' = |E_\pm|/(\vec{e'} \cdot \vec{\sigma}), \tag{1.109}$$

$$\vec{e'} \overset{\text{def}}{=\!=} \frac{1}{\sin|E_\pm|}\begin{pmatrix} \cos(k_p + k_n)\cos\theta_2\sin\theta_1 + \cos(k_n - k_p)\cos\theta_1\sin\theta_2 \\ \sin(k_p - k_n)\sin\theta_2 \\ \cos\theta_2\sin(k_n + k_p) \end{pmatrix}. \tag{1.110}$$

It is now interesting to note that the Hamiltonian of the 1D walk can be transformed into

the one of the 2D walk without phase modulation, using the following permutation:

$$E_{2D} = f(k_n, k_p, \theta_1 + \theta_2, \theta_1 - \theta_2) \Longleftrightarrow E_{1D} = f(\theta_1, \theta_2, 2k, 2\varphi), \tag{1.111}$$

$$\vec{e'}_{2D} = \vec{e'}(k_p + k_n, k_p - k_n, \theta_1, \theta_2) \Longleftrightarrow \vec{e'}_{1D} = \vec{e'}(2k, 2\varphi, \theta_1, \theta_2). \tag{1.112}$$

As a consequence, one might expect a certain topological equivalence between these systems. Indeed, in section 1.7 we show that both Hamiltonians span over almost the same spectrum of topological classes, except the AI class, which is possible only for the 1D walk and not for the 2D one without phase modulation.

1.5.3 2D four-component pseudospin walk

Finally, the four-component walk is generalized as well with the dynamical coupling as

$$\hat{U} = \hat{S}_{p'}\hat{C}_2(\theta_2)\hat{S}_{n'}\hat{C}_1(\theta_1), \tag{1.113}$$

$$\hat{C}_1(\theta_1) = \begin{pmatrix} \cos\varphi & i\sin\varphi & 0 & 0 \\ i\sin\varphi & \cos\varphi & 0 & 0 \\ 0 & 0 & \cos\varphi & i\sin\varphi \\ 0 & 0 & i\sin\varphi & \cos\varphi \end{pmatrix}, \tag{1.114}$$

$$\hat{C}_2(\theta_2) = \begin{pmatrix} \cos\varphi & 0 & 0 & i\sin\varphi \\ 0 & \cos\varphi & i\sin\varphi & 0 \\ 0 & i\sin\varphi & \cos\varphi & 0 \\ i\sin\varphi & 0 & 0 & \cos\varphi \end{pmatrix}, \tag{1.115}$$

where, for simplicity we disregarded the phase modulation. Then, the band structure reads

$$\begin{aligned} E_{1,\pm} = \arccos\Big(&\cos k_n \cos k_p \cos\theta_1 \cos\theta_2 - \\ &- \frac{1}{4}\sqrt{(\cos 2k_p - 3 + 2\cos^2 2k_p \cos 2\theta_1)(\cos 2k_n - 3 + 2\cos^2 2k_n \cos 2\theta_2)}\Big), \end{aligned} \tag{1.116}$$

$$\begin{aligned} E_{2,\pm} = \arccos\Big(&\cos k_n \cos k_p \cos\theta_1 \cos\theta_2 + \\ &+ \frac{1}{4}\sqrt{(\cos 2k_p - 3 + 2\cos^2 2k_p \cos 2\theta_1)(\cos 2k_n - 3 + 2\cos^2 2k_n \cos 2\theta_2)}\Big). \end{aligned} \tag{1.117}$$

Evidently, this walk is very distinct from other 1D and 2D systems with a two-component pseudospin, because none of the coupling values is able to perfectly match the upper two (or the lower two) bands together and thus decouple the four-component pseudospin into two two-component ones. Moreover, we will show further below that the four-component pseudospin walk in contrast possess a very robust "achirality", which is directly translated to its distinct spectrum of topological classes, which remains within the range of so-called chiral topological insulators.

1.6 On-site and global symmetries of the walks

In this section, we derive all fundamental symmetries of the one- and two-dimensional walks. Afterwards in section 1.7, the obtained groups of symmetries will allow us to classify the bosonic systems among other topological insulators and semiconductors. The symmetries to be considered comprise on-site transformations (chiral, particle-hole and time-reversal symmetries), which transform each individual pseudospin of a state locally in space, as well

as the global parity (inversion) transformation, which flips the entire lattice in space, thus exchanging the pseudospins. It is worth saying, that we do not consider here translation symmetries as well as discrete rotations of the two-dimensional lattices.

While the parity transformation has the direct geometrical interpretation, other (local) symmetries are outlined only ambiguously, so, for example, the 2D lattices having different underlying networks can obey a local symmetry, described by two different exact forms. Moreover, we will see that even within the single network of the 2D four-component pseudospin walk, chiral and particle-hole symmetry can be expressed differently for different periodic potentials. On the other hand, the presence of chiral or particle-hole symmetry translates to a certain symmetry of the band structure as will be shown later. However, the presence of the band structure symmetry by itself does not yet guarantee that the respective symmetry is respected. Therefore, in order to validate one or another symmetry, one has to find the rigorous form of its associated operator at least in one of the time frames of the evolution. Another difficulty is that all the generalized walks with periodically-varied phase and/or couplings belong to the class of Floquet systems. The evolution operator for such systems can be described in two dynamically equivalent ways: 1) a stroboscopic mapping of each sublattice onto itself, expressed by doubled time-step evolution operator 2) cross-mapping of one sublattice to another and vice versa, described by a one time-step (instantaneous) evolution matrix with a doubled size. However, the group of symmetries representing the stroboscopic effective Hamiltonian in general can differ from the group of symmetries of the instantaneous Hamiltonian, because, for example, time-reversal symmetry can break on the "micrcoscopic" level and still be valid for the stroboscopic time-averaged system. As a result, the stroboscopic and the instantaneous bulk Hamiltonians can have very different topological properties, despite having equivalent dynamics of the bulk modes. Therefore, before getting in touch with the topological classification, we first have to evaluate and distinguish the groups of symmetries in both pictures.

1.6.1 Chiral symmetry

We begin our consideration with chiral (sublattice) symmetry, which defines whether each eigenstate of the system with an eigenenergy E has its mirror symmetric counterpart, which in turn is also an eigenstate of the system with the opposite eigenenergy $E' = -E$. The mirror symmetry implies that each individual pseudospin of the state undergoes a certain local transformation. Mathematically, the condition for chiral symmetry of the system $\hat{H}$ reads

$$\hat{\chi}\hat{H}\hat{\chi}^{-1} = -\hat{H}, \tag{1.118}$$

where $\hat{\chi}$ is a unitary operator $(\hat{\chi}^{-1} = \hat{\chi}^{\dagger})$, acting locally on each spin as

$$\hat{\chi} = \sum_n |n\rangle \langle n| \otimes \hat{\chi}_n = \sum_n |n\rangle \langle n| \otimes \hat{\chi}, \tag{1.119}$$

where we deliberately chose the uniformly defined local operator $(\chi_n = \chi, \forall n)$, since the bulk Hamiltonian is homogeneous as well. The condition (1.118) can be equivalently translated to the evolution operator by using Taylor expansion of the exponent $\hat{U} = \exp\left(i\hat{H}\right)$, namely

$$\hat{\chi}\hat{U}\hat{\chi}^{-1} = \hat{U}^{-1}. \tag{1.120}$$

Assuming that $|\psi\rangle$ is an eigenvector of the Hamiltonian with the eigenenergy E, we get

$$\hat{H}\,|\psi\rangle = E\,|\psi\rangle \Rightarrow \hat{\chi}(\hat{H}\,|\psi\rangle) = -\hat{H}(\hat{\chi}\,|\psi\rangle) \Rightarrow -E(\hat{\chi}\,|\psi\rangle) = \hat{H}(\hat{\chi}\,|\psi\rangle), \qquad (1.121)$$

i.e. there is another eigenvector $\hat{\chi}\,|\psi\rangle$ with the opposite energy, which is the chiral counterpart of $|\psi\rangle$. Note, that this condition holds for all networks considered above. This given alone, however, does not guarantee the presence of chiral symmetry as already mentioned above.

1D pseudospin walk

Due to the Floquet dichotomy mentioned above, we shall consider both stroboscopic and instantaneous pictures for the generalized one-dimensional walk. To start with the first one, let us use the chiral symmetric time frame (see eq. (1.100)) and probe the following Pauli matrices

$$\hat{\chi}_{1,2} = \sum_n |n\rangle\,\langle n| \otimes \hat{\sigma}_{y,z}, \qquad (1.122)$$

which are unitary and uniformly defined for all positions. Rigorous calculations of the symmetry condition (1.120) yield

$$\Delta_{\chi_1}\hat{U}'_{1D} \overset{\text{def}}{=} \hat{\chi}_1\hat{U}'_{1D}\hat{\chi}_1^{-1} - \hat{U}'^{-1}_{1D} = 2i\sin(2\varphi)\sin(\theta_2)\hat{\sigma}_y, \qquad (1.123)$$

$$\Delta_{\chi_2}\hat{U}'_{1D} \overset{\text{def}}{=} \hat{\chi}_2\hat{U}'_{1D}\hat{\chi}_2^{-1} - \hat{U}'^{-1}_{1D} = 2i\sin(2k)\cos(\theta_2)\hat{\sigma}_z. \qquad (1.124)$$

We see that the second operator does not represent a generic chiral symmetry, since only some invariant quasimomenta satisfy it, unless the trivial reduction to zero-dimensional Hamiltonian at $\theta_2 = 0, \frac{\pi}{2}, \pi, ...$ takes place. On the other hand, the first operator states that the system becomes chiral if $\varphi = 0, \frac{\pi}{2}$. Further on, we will not concentrate on the trivial scenarios of a reduced dimensionality, neither in 2D nor in 1D systems, but it is worth mentioning that the rotation of the time frame, which instead places $\hat{C}(\theta_2)$ in the center of the evolution matrix, will obviously lead us to the same condition for θ_1, while leaving the condition for the phase amplitude unchanged.

Next, we extend the system in order to simultaneously cover both sublattices, comprising odd and even positions, respectively. In detail, the instantaneous evolution operator driving states of both sublattices at the same time reads

$$\hat{\hat{U}}_{1D} = \begin{pmatrix} 0 & \hat{\Phi}(\varphi)\hat{S}\hat{C}(\theta_1) \\ \hat{\Phi}(-\varphi)\hat{S}\hat{C}(\theta_2) & 0 \end{pmatrix}, \qquad (1.125)$$

where the double hat of $\hat{\hat{U}}$ indicates the doubled size of the matrix. Note, that the elementary evolution operator covers only one time step since the phase periodic potential is static as one can see in Fig. 1.10. It is easy to check that $\hat{\hat{U}}^2_{1D}$ corresponds to a block diagonal matrix comprising two original evolution operators stroboscopically promoting the states, that occupy their respective sublattices. One can verify that none of the chiral operators (1.122), when extended to the doubled dimension, is respected by the evolution operator and thus χ_1 can be fulfilled only on the time-averaged stroboscopic level. Nevertheless, one can construct another symmetry operator, which would mutually exchange the sublattices.

Indeed, consider the following operator:

$$\hat{\chi} = \sum_n |n\rangle \langle n| \otimes \frac{1}{\sqrt{2}} \begin{pmatrix} \hat{0} & \hat{\sigma}_z + \hat{\sigma}_y \\ \hat{\sigma}_z + \hat{\sigma}_y & \hat{0} \end{pmatrix}. \tag{1.126}$$

By verifying the condition (1.120), we get

$$\Delta_\chi \hat{U}_{1D} = 0, \text{ only if } \theta_1 = \frac{\pi}{4} + \pi N, \theta_2 = \frac{\pi}{4} + \pi M, (M, N \in \mathbb{Z}). \tag{1.127}$$

Note, that the instantaneous chiral symmetry flipping the sublattices does not impose any restrictions on the phase amplitude, but instead it becomes sensitive to the coupling parameters. Finally, both the instantaneous and the stroboscopic chiral symmetries are simultaneously respected only if both bands become gapless, merging at Dirac degeneracy points.

2D two-component pseudospin walk

Next, regarding the two-dimensional walk (1.103), our analysis shows that the stroboscopic effective Hamiltonian does not satisfy any chiral symmetry, even in the rotated time frame (1.108). In particular, when testing the operators (1.122) we come up with

$$\Delta_{\chi_1} \hat{U}'_{2D} \overset{\text{def}}{=\!=} \hat{\chi}_1 \hat{U}'_{2D} \hat{\chi}_1^{-1} - \hat{U}'^{-1}_{2D} = 2i \sin(k_n - k_p) \sin(\theta_2) \hat{\sigma}_y, \tag{1.128}$$

$$\Delta_{\chi_2} \hat{U}'_{2D} \overset{\text{def}}{=\!=} \hat{\chi}_2 \hat{U}'_{2D} \hat{\chi}_2^{-1} - \hat{U}'^{-1}_{2D} = 2i \sin(k_n + k_p) \cos(\theta_2) \hat{\sigma}_z, \tag{1.129}$$

i.e. the lattice on the stroboscopic level should be chiral, i.e. violating the chiral symmetry. Therefore, one has to consider the extended picture, covering the sublattices (l,r) and (u,d) simultaneously, namely

$$\hat{\hat{U}}_{2D} = \begin{pmatrix} \hat{0} & \hat{S}_n \hat{C}_2(\theta_2) \\ \hat{S}_k \hat{C}_1(\theta_1) & \hat{0} \end{pmatrix}, \tag{1.130}$$

where the double hat indicates the bigger size of the evolution matrix. Similarly to 1D case, $\hat{\hat{U}}^2_{2D}$ forms block diagonal matrix with each block independently evolving the state in the respective sublattice. If we in addition "dress" the system with the phase modulation given by the eq. (1.72), the phase pattern groups the sublattices positionwise, i.e. the phase operator is applied as $\hat{\Phi}(+\varphi)$ and then $\hat{\Phi}(-\varphi)$ (or $\hat{\Phi}(+\varphi)$) to state components occupying positions with $\mod(|n| + |k|)/2, 2) = 1$ and as $\hat{\Phi}(-\varphi)$ and then $\hat{\Phi}(+\varphi)$ (or $\hat{\Phi}(-\varphi)$) to state components occupying positions with $\mod(|n| + |k|)/2, 2) = 0$, as follows from eq. (1.72). As a result, the evolution picture with 4×4 matrices becomes again stroboscopic, namely the evolution operator reads

$$\hat{\hat{U}}_{2D} = \begin{pmatrix} \hat{0} & \hat{\Phi}(-\varphi)\hat{S}_n\hat{C}_2(\theta_2)\hat{\Phi}(+\varphi)\hat{S}_k\hat{C}_1(\theta_1) \\ \hat{\Phi}(+\varphi)\hat{S}_n\hat{C}_2(\theta_2)\hat{\Phi}(-\varphi)\hat{S}_k\hat{C}_1(\theta_1) & \hat{0} \end{pmatrix}, \tag{1.131}$$

i.e. it has now again the temporal period of two. In order to make the picture again instantaneous, one would have to double again the operator in order to cover states at both position groups $\mod(|n| + |k|)/2, 2) = 0, 1$ simultaneously. We, however, satisfy ourselves with this stroboscopic picture and later show that all fundamental symmetries

can be identified in it, although the topological classification becomes ambiguous, i.e. two different symmetry classes become equivalently possible for the stroboscopic system. Thus, we proceed with the chiral mirroring, which locally flips the components (l,r) and (u,d) at individual positions belonging to $\mod(|n|+|k|)/2, 2) = 1$ or $\mod(|n|+|k|)/2, 2) = 0$, and verify the operator (1.126), which can be trivially extended to the additional spatial dimension p. Thus, applying the symmetry condition to (1.131), we get

$$\Delta_\chi \hat{\hat{U}}_{2D} = 0, \text{ only if } \theta_1 = \frac{\pi}{4} + \pi N_1, \theta_2 = \frac{\pi}{4} + \pi N_2 \ \& \ \varphi = \frac{\pi}{2}M, (N_1, N_2, M \in \mathbb{Z}). \quad (1.132)$$

Interestingly, the chirality conditions simultaneously combine those found for the one-dimensional walk. Physically, the condition for balanced couplings θ can be explained by a certain equilibrium between "microscopic" power flows, localized in each lattice unit cell and rotating in clockwise and counter-clockwise directions (see Fig. 1.12). Any deviation of θ_1 or θ_2 from the equilibrium point would introduce a certain handedness to the system. Similarly, the phase modulation is introducing chirality to the system unless the critical case of gap closing and degenerate Dirac cones is met.

2D four-component pseudospin walk

In the four-component pseudospin walk, one encounters the same problem as in the 2D two-component pseudospin walk, namely there is no any chiral symmetry respected by the effective evolution operator (1.79). Therefore, we have to extend the effective framework to two sublattices, containing four components and being driven simultaneously. First, we consider the redundant stroboscopic picture

$$\hat{\hat{U}}_{2D,\text{strob}} = \begin{pmatrix} \hat{\hat{0}} & \hat{\hat{\Phi}}(+\varphi)\hat{\hat{S}}_{n'}\hat{\hat{C}}_1(\theta_1) \\ \hat{\hat{\Phi}}(-\varphi)\hat{\hat{s}}_{k'}\hat{\hat{C}}_2(\theta_2) & \hat{\hat{0}} \end{pmatrix} \cdot \begin{pmatrix} \hat{\hat{0}} & \hat{\hat{\Phi}}(+\varphi)\hat{\hat{S}}_{n'}\hat{\hat{C}}_1(\theta_1) \\ \hat{\hat{\Phi}}(-\varphi)\hat{\hat{s}}_{k'}\hat{\hat{C}}_2(\theta_2) & \hat{\hat{0}} \end{pmatrix},$$
$$(1.133)$$

where, in addition to the variable coupling (1.113), we included the phase modulation according to eq. (1.79). Note, that the doubled evolution period is redundant, but we use it for reasons, that will become clear later on. Introducing the following chiral symmetry operators

$$\hat{\hat{\chi}}_1 = \sum |n',p'\rangle \langle n',p'| \otimes \begin{pmatrix} \hat{0} & \hat{0} & \hat{0} & \hat{\sigma}_z \\ \hat{0} & \hat{0} & \hat{\sigma}_z & 0 \\ \hat{0} & \hat{\sigma}_z & \hat{0} & \hat{0} \\ \hat{\sigma}_z & 0 & \hat{0} & \hat{0} \end{pmatrix}, \ \hat{\hat{\chi}}_2 = \sum |n',p'\rangle \langle n',p'| \otimes \begin{pmatrix} \hat{0} & \hat{0} & \hat{0} & \hat{\sigma}_0 \\ \hat{0} & \hat{0} & \hat{\sigma}_x & 0 \\ \hat{0} & \hat{\sigma}_0 & \hat{0} & \hat{0} \\ \hat{\sigma}_0 & 0 & \hat{0} & \hat{0} \end{pmatrix},$$
$$(1.134)$$

we get

$$\Delta_\chi \hat{\hat{\hat{U}}}_{2D,\text{strob}} = 0, \ \forall \theta_1, \theta_2 \ \& \ \varphi = 0, \pi, ... \quad (1.135)$$

$$\Delta_\chi \hat{\hat{\hat{U}}}_{2D,\text{strob}} = 0, \ \forall \theta_1, \theta_2 \ \& \ \varphi = \frac{\pi}{2}, \frac{3}{2}\pi, ... \quad (1.136)$$

One can see that even unbalanced couplings can not break the chiral symmetry of the lattice, what likely follows from the very robust "achirality" of the walk, as one can infer by looking at the network in Fig. 1.5.

Now, let us consider the elementary instantaneous evolution operator:

$$\hat{\hat{U}}_{2D,\text{inst}} = \begin{pmatrix} \hat{\hat{0}} & \hat{\hat{\Phi}}(+\varphi)\hat{\hat{S}}_{n'}\hat{\hat{C}}_1(\theta_1) \\ \hat{\hat{\Phi}}(-\varphi)\hat{\hat{S}}_{k'}\hat{\hat{C}}_2(\theta_2) & \hat{\hat{0}} \end{pmatrix}. \tag{1.137}$$

Applying the same chiral operators (1.134) to that operator, we come up with:

$$\Delta_\chi \hat{\hat{U}}_{2D,\text{inst}} = 0, \ \forall \theta_1, \theta_2 \ \& \ \varphi = 0, \pi, ... \tag{1.138}$$

$$\Delta_\chi \hat{\hat{U}}_{2D,\text{inst}} \neq 0. \tag{1.139}$$

Surprisingly, the chiral symmetry gets broken for $\varphi = \pi/2, 3\pi/2, ...$, although the band structure is the same as for the unmodulated lattice, according to eq. (1.80). Therefore, the stroboscopic system, dynamically equivalent to the instantaneous one, is generally more symmetric.

1.6.2 Particle-hole symmetry

Another fundamental symmetry is called particle-hole or charge conjugation symmetry. Similarly to the chiral symmetry, this one causes the existence of a symmetric counterpart of a particle (antiparticle), which propagates with an opposite quasienergy and quasimomentum, being governed by the same Hamiltonian. Such a propagation is equivalent to the propagation of the original particle backwards in time. If, under the time-reversal, the antiparticle in addition holds the same handedness as the particle (chiral symmetry is fulfilled), then one can expect time-reversal symmetry as well, as will be discussed in the next subsection. The operator of particle-hole symmetry also containing the time-reversal is described by an antiunitary operator

$$\hat{T}_- = \hat{R}K \otimes \sum_n |n\rangle \langle n| = \int_k |-k\rangle \langle k|\, dk \otimes \hat{R}K, \tag{1.140}$$

where $\hat{R}$ is some unitary local homogeneously defined operator and K is the operator of complex conjugation, acting in position space. Therefore, the quasimomenta $\sim \sum \exp(ink)|n\rangle$ have to flip with respect to zero. Then, the symmetry condition reads

$$\hat{T}_- \hat{H} \hat{T}_-^{-1} = -\hat{H}, \Longleftrightarrow \hat{T}_- \hat{U} \hat{T}_-^{-1} = \hat{U}. \tag{1.141}$$

Assuming a Hamiltonian written in the reciprocal space obeys the symmetry and $|\psi(k)\rangle$ is a Bloch eigenmode of the system, we get

$$\hat{H}|\psi(k)\rangle = E|\psi(k)\rangle \Rightarrow \hat{T}_- E|\psi(k)\rangle = -\hat{T}_-|\psi(k)\rangle \Rightarrow -E(\hat{R}|\psi^*(-k)\rangle) = \hat{H}(\hat{R}|\psi^*(-k)\rangle), \tag{1.142}$$

where $\hat{R}|\psi^*(-k)\rangle$ is the symmetric counterpart, associated with the antiparticle.

1D pseudospin walk

For the one-dimensional generalized walk, we introduce the following effective particle-hole symmetry operator

$$\hat{T}_- = \hat{\sigma}_z K \otimes \sum_n |n\rangle \langle n| = \int_k |-k\rangle \langle k| \, dk \otimes \hat{\sigma}_z K. \tag{1.143}$$

Implementing rigorous calculation of the symmetry condition in the rotated time frame (1.100) yields

$$\Delta_{T_-} \hat{U}'_{1D} \stackrel{\text{def}}{=} \hat{T}_- \hat{U}'_{1D} \hat{T}_-^{-1} - \hat{U}'_{1D} = -2i \sin(2\varphi) \sin(\theta_2) \hat{\sigma}_y. \tag{1.144}$$

One can see that particle-hole symmetry holds and breaks together with the effective chiral symmetry $\hat{\chi}_1$. The operator $\hat{T}_-$ can be straightforwardly extended to both sublattices as

$$\hat{\hat{T}}_{-,1} = \int_k |-k\rangle \langle k| \, dk \otimes \begin{pmatrix} \hat{\sigma}_z & \hat{0} \\ \hat{0} & \hat{\sigma}_z \end{pmatrix} K. \tag{1.145}$$

However it turns out that the instantaneous evolution operator respect the symmetry only if $\varphi = 0, \pi, ...$, i.e. the condition skips the intermediate points of φ. Therefore, another extension of T_- should be equally possible. Indeed, we can write

$$\hat{\hat{T}}_{-,2} = \int_k |-k\rangle \langle k| \, dk \otimes \begin{pmatrix} -i\hat{\sigma}_z & \hat{0} \\ \hat{0} & i\hat{\sigma}_z \end{pmatrix} K. \tag{1.146}$$

One can check that this operator is antiunitary and it is indeed respected by the system if $\varphi = \pi/2, 3\pi/2...$. In summary, we can write

$$\Delta_{T_{-,1}} \hat{\hat{U}}_{1D} = 0, \text{only if } \varphi = \pi N, N \in \mathbb{Z}, \tag{1.147}$$

$$\Delta_{T_{-,2}} \hat{\hat{U}}_{1D} = 0, \text{only if } \varphi = \frac{\pi}{2} + \pi N, N \in \mathbb{Z}. \tag{1.148}$$

2D two-component walk

In the two-dimensional walk of a two-component pseudospin, the particle-hole symmetry (PHS) can be also described within the effective framework of a single sublattice stroboscopic evolution. Indeed, using again eq. (1.143), we get

$$\Delta_T \hat{U}_{2D} \stackrel{\text{def}}{=} \hat{T}_- \hat{U}_{2D} \hat{T}_-^{-1} - \hat{U}_{2D} = 0, \ \forall \theta_1, \theta_2, \text{ only if } \varphi = 0, \frac{\pi}{2}, \pi, ... \tag{1.149}$$

Thus, similarly to PHS of the 1D case, arbitrary coupling coefficients do not violate the symmetry, but the periodic potential can break it. One could also use the extended picture and eventually get:

$$\Delta_{T_{-,1}} \hat{\hat{U}}_{2D} = \Delta_{T_{-,2}} \hat{\hat{U}}_{2D} = 0, \text{only if } \varphi = \frac{\pi}{2} N, N \in \mathbb{Z}. \tag{1.150}$$

2D four-component pseudospin walk

For the four-component pseudospin walk, we consider first the instantaneous picture (1.137) and verify $\hat{\tilde{T}}_{-,1}$ and $\hat{\tilde{T}}_{-,2}$ introduced first for the one-dimensional walk. It turns out, that $\hat{\tilde{T}}_{-,2}$ is always violated , while the former one, written in the diagonal basis of the four-component walk as

$$\hat{\tilde{T}}_{-,1} = \iint |-k_{n'}, -k_{p'}\rangle \langle k_{n'}, k_{p'}| \, dk_{n'} dk_{p'} \otimes \begin{pmatrix} \hat{\sigma}_z & \hat{0} & 0 & 0 \\ \hat{0} & \hat{\sigma}_z & 0 & 0 \\ 0 & 0 & \hat{\sigma}_z & \hat{0} \\ 0 & 0 & 0 & \hat{\sigma}_z \end{pmatrix} K \tag{1.151}$$

can be valid, namely

$$\Delta_{T_{-,1}} \hat{\tilde{U}}_{2D,\text{inst}} \stackrel{\text{def}}{=} \hat{T}_{-,1} \hat{\tilde{U}}_{2D,\text{inst}} \hat{T}_{-,1}^{-1} - \hat{\tilde{U}}_{2D,\text{inst}} = 0, \ \forall \theta_1, \theta_2, \text{ only if } \varphi = \pi N, N \in \mathbb{Z}. \tag{1.152}$$

It means the PHS and the chiral symmetry $\hat{\tilde{\chi}}_1$ both hold and break at the same phase amplitude parameters.

Now, if we consider the stroboscopic redundant picture (1.133) and again apply the operator (1.151), than we get

$$\Delta_{T_{-,1}} \hat{\tilde{U}}_{2D,\text{strob}} = 0, \ \forall \theta_1, \theta_2, \text{ only if } \varphi = \frac{\pi}{2} N, N \in \mathbb{Z}. \tag{1.153}$$

Note that in the stroboscopic, but still not effective, picture, the symmetry operator now picks up all the critical points of the phase amplitude.

1.6.3 Time-reversal symmetry

The last on-site fundamental symmetry to be discussed in this subsection is time-reversal symmetry (TRS). It has been already mentioned, that the combination of chirality and PHS necessarily leads to time-reversal symmetry. More specifically, the following relation holds:

$$\hat{T}_+ = \hat{\chi} \hat{T}_-^{-1}, \tag{1.154}$$

where $\hat{T}_+$ is an antiunitary operator of TRS, which is fulfilled if

$$\hat{T}_+ \hat{H} \hat{T}_+^{-1} = \hat{H}, \Longleftrightarrow \hat{T}_+ \hat{U} \hat{T}_+^{-1} = \hat{U}^{-1}. \tag{1.155}$$

Note, however, that TRS can be still respected if both chiral and PHS symmetries are violated. Writing the general form of the antiunitary operator as

$$\hat{T}_+ = \hat{R} K \otimes \sum_n |n\rangle \langle n| = \int_k |-k\rangle \langle k| \, dk \otimes \hat{R} K, \tag{1.156}$$

and assuming that $|\psi(k)\rangle$ is some eigenmode of the system, we get

$$\hat{H} |\psi(k)\rangle = E |\psi(k)\rangle \Rightarrow \hat{T}_+ E |\psi(k)\rangle = \hat{T}_+ |\psi(k)\rangle \Rightarrow E(\hat{R} |\psi^*(-k)\rangle) = \hat{H}(\hat{R} |\psi^*(-k)\rangle). \tag{1.157}$$

It is known, that if $\hat{T}_+^2 = -1$ (valid for a fermionic system with half-integer total spin), then the states $\hat{T}_+ |\psi\rangle$ and $|\psi\rangle$ can not be equal and therefore every energy level has to be doubly degenerate, the result known as Kramers degenercy. However, we will see further on, that in the full picture of two-component pseudospin walks, the value of $\hat{T}_+^2$ can be +1 as well as -1. We attribute this ambiguity to the spatial origin of the pseudospin, i.e. it is not associated with the real spin of the walking photon.

One-dimensional pseudospin walk

In the effective stroboscopic picture, straightforward derivation of the TRS operator from the chiral operator $\hat{\chi}_1$ in (1.122) and the PHS operator (1.143) yields

$$\hat{T}_+ = \hat{\chi}_1 \hat{T}_-^{-1} = \int_k |-k\rangle \langle k| \, dk \otimes \hat{\sigma}_x K. \tag{1.158}$$

Then, applying the symmetry condition (1.155) to the evolution operator in the rotated time frame, we arrive at

$$\Delta_{T_{+,1}} \hat{U}'_{1D} \overset{\text{def}}{=\!=} \hat{T}_{+,1} \hat{U}'_{1D} \hat{T}_{+,1}^{-1} - \hat{U}'^{-1}_{1D} = 0. \tag{1.159}$$

Thus, the stroboscopic time-reversal symmetry is satisfied for any Hamiltonian parameters, even in the case, where both PHS and chiral symmetries are broken. However, it is important to distinguish the symmetries valid exclusively for the stroboscopic system and the instantaneous one, because otherwise one can meet the following contradiction. Let's assume the chiral symmetry represented by the extended operator (1.126) holds, provided θ_1 and θ_2 are equal to $\pi/4$ or $\pi/4 + \pi$. If $\varphi \neq M\pi/2$ for an integer M, then PHS is broken, according to conditions (1.147). But nevertheless, the time-reversal symmetry holds as follows from the above derived condition. Since the two fundamental symmetries can not be valid together without recovering PHS as well, we obtain the contradiction. Therefore, the different pictures should lead to different symmetry classes and eventually they may exhibit different topological properties as will be discussed in the next section.

To that end, we will derive other two extended time-reversal operators, using the chiral (1.126) and the PHS (1.145),(1.146) operators, as follows

$$\hat{\hat{T}}_{+,1} = \hat{\hat{\chi}} \hat{\hat{T}}_{-,1}^{-1} = \int dk \, |-k\rangle \langle k| \otimes \begin{pmatrix} \hat{0} & e^{i\frac{\pi}{4}\hat{\sigma}_x} \\ e^{i\frac{\pi}{4}\hat{\sigma}_x} & \hat{0} \end{pmatrix} K, \tag{1.160}$$

$$\hat{\hat{T}}_{+,2} = \hat{\hat{\chi}} \hat{\hat{T}}_{-,2}^{-1} = \int dk \, |-k\rangle \langle k| \otimes \begin{pmatrix} \hat{0} & -ie^{i\frac{\pi}{4}\hat{\sigma}_x} \\ ie^{i\frac{\pi}{4}\hat{\sigma}_x} & \hat{0} \end{pmatrix} K. \tag{1.161}$$

Applying the symmetry condition (1.155) yields

$$\Delta_{T_{+,1}} \hat{\hat{U}}_{1D} = 0, \text{ only if } \theta_1 = \frac{\pi}{4} + \pi N_1, \theta_2 = \frac{\pi}{4} + \pi N_2, \varphi = \pi M, (M, N_1, N_2 \in \mathbb{Z}), \tag{1.162}$$

$$\Delta_{T_{+,2}} \hat{\hat{U}}_{1D} = 0, \text{ only if } \theta_1 = \frac{\pi}{4} + \pi N_1, \theta_2 = \frac{\pi}{4} + \pi N_2, \varphi = \frac{\pi}{2} + \pi M, (M, N_1, N_2 \in \mathbb{Z}). \tag{1.163}$$

We see that this symmetry condition is much more demanding compared to the stroboscopic one. It holds only if the "microscopic" chiral $\hat{\hat{\chi}}$ and one of the PHS $\hat{\hat{T}}_-$ are respected

simultaneously.

2D two-component pseudospin walk

It is clear now that TRS of the two-dimensional walk has to be represented in terms of the extended stroboscopic picture (1.131), since the chirality operator in the reduced picture is generally violated according to eq. (1.128). Therefore, we directly extend the operators in (1.160) to two dimensions, namely

$$\hat{\tilde{T}}_{+,1} = \hat{\tilde{\chi}}\hat{\tilde{T}}_{-}^{-1} = \iint dk_n dk_p \, |-k_n, -k_p\rangle \langle k_n, k_p| \otimes \begin{pmatrix} \hat{0} & e^{i\frac{\pi}{4}\hat{\sigma}_x}, \\ e^{i\frac{\pi}{4}\hat{\sigma}_x} & \hat{0} \end{pmatrix} K, \tag{1.164}$$

$$\hat{\tilde{T}}_{+,2} = \hat{\tilde{\chi}}\hat{\tilde{T}}_{-}^{-1} = \iint dk_n dk_p \, |-k_n, -k_p\rangle \langle k_n, k_p| \otimes \begin{pmatrix} \hat{0} & -ie^{i\frac{\pi}{4}\hat{\sigma}_x}, \\ ie^{i\frac{\pi}{4}\hat{\sigma}_x} & \hat{0} \end{pmatrix} K. \tag{1.165}$$

Applying the symmetry condition, we get

$$\Delta_{T_{+,1}}\hat{\tilde{U}}_{2D} = \Delta_{T_{+,2}}\hat{\tilde{U}}_{2D} = 0, \text{ only if } \theta_1 = \frac{\pi}{4} + \pi N_1, \theta_2 = \frac{\pi}{4} + \pi N_2, (N_1, N_2 \in \mathbb{Z}). \tag{1.166}$$

So, one can see that if the system holds both the "microscopic" TRS and the PHS symmetry, then the "microscopic" chiral symmetry holds as well.

2D four-component pseudospin walk

For the four-component walk, we derive two TRS operators, based on the extended chirality operators (1.134) and the PHS operator (1.151), and arrive at

$$\hat{\tilde{\tilde{T}}}_{+,1} = \sum |-k_{n'}, -k_{p'}\rangle \langle k_{n'}, k_{p'}| \otimes \begin{pmatrix} \hat{0} & \hat{0} & \hat{0} & \hat{\sigma}_0 \\ \hat{0} & \hat{0} & \hat{\sigma}_0 & 0 \\ \hat{0} & \hat{\sigma}_0 & \hat{0} & \hat{0} \\ \hat{\sigma}_0 & 0 & \hat{0} & \hat{0} \end{pmatrix} K, \tag{1.167}$$

$$\hat{\tilde{\tilde{T}}}_{+,2} = \sum |-k_{n'}, -k_{p'}\rangle \langle k_{n'}, k_{p'}| \otimes \begin{pmatrix} \hat{0} & \hat{0} & \hat{0} & \hat{\sigma}_z \\ \hat{0} & \hat{0} & \hat{\sigma}_z & 0 \\ \hat{0} & \hat{\sigma}_z & \hat{0} & \hat{0} \\ \hat{\sigma}_z & 0 & \hat{0} & \hat{0} \end{pmatrix} K. \tag{1.168}$$

Applying the symmetry condition to the redundant stroboscopic evolution operator (1.133) with doubled time step, we obtain

$$\Delta_{T_{+,1}}\hat{\tilde{U}}_{2D,\text{strob}} = 0, \text{ only if } \varphi = 0, \pi, ..., \tag{1.169}$$

$$\Delta_{T_{+,2}}\hat{\tilde{U}}_{2D,\text{strob}} = 0, \text{ only if } \varphi = \frac{\pi}{2}, \frac{3\pi}{2}, ... \tag{1.170}$$

Then, if we apply it to the instantaneous evolution operator of the same size (1.137), we get

$$\Delta_{T_{+,1}}\hat{\tilde{U}}_{2D,\text{inst}} = 0, \text{ only if } \varphi = 0, \pi, ..., \tag{1.171}$$

$$\Delta_{T_{+,2}}\hat{\tilde{U}}_{2D,\text{inst}} \neq 0. \tag{1.172}$$

Therefore, TRS symmetry breaks together with chiral symmetry in both stroboscopic and instantaneous pictures.

1.6.4 Parity (reflection) symmetry

So far, we have dealt with local fundamental symmetries, that transform a state components locally within each position. Although we do not concentrate, for example, on discrete rotation symmetries taking place for two-dimensional systems, we shall consider in detail the parity symmetry, which is also known as reflection symmetry. This symmetry has a clear geometrical sense, namely a parity symmetric lattice has to remain invariant after flipping with respect to some inversion point in the 1D or inversion line in the 2D case. It is clear that for a homogeneous walk, the inversion point or line can be chosen arbitrarily, but due to the discreteness it has to have an integer or half-integer discrete position, so that all beam splitters (nodal point of the lattice) could overlap with each other under the reflection.

Mathematically, the parity operator is expressed by a unitary operator, which should commute with the Hamiltonian, namely

$$\hat{P}\hat{H}\hat{P}^{-1} = \hat{H} \iff \hat{P}\hat{U}\hat{P}^{-1} = \hat{U}. \tag{1.173}$$

If these relations hold, then one can always find a common basis of eigenstates for the Hamiltonian and the parity operator, so that the eigenstates are spatially symmetric or anti-symmetric with respect to the mirroring line or point.

1D pseudospin walk

The reflection operator with respect to the position $n = 0$ can be straightforwardly defined in the one-dimensional system as

$$\hat{P} = \hat{\sigma}_x \otimes \sum_n |-n\rangle \langle n| = \hat{\sigma}_x \otimes \int_k |-k\rangle \langle k| \, dk, \tag{1.174}$$

where σ_x is exchanging l and r components of opposite pseudospins, belonging to the same sublattice with odd or even positions. Applying the condition (1.173) to the stroboscopic effective evolution operator, we come up with

$$\Delta_P \hat{U}_{1D} \stackrel{\text{def}}{=} \hat{P}\hat{U}_{1D}\hat{P}^{-1} - \hat{U}_{1D} = -2\sin 2\varphi \sin\theta_2 \hat{\sigma}_y, \tag{1.175}$$

where expectantly the parity symmetry is violated by the periodic potential unless $\varphi = 0, \pi/2, \dots$. Indeed, one can see in Fig. 1.10 that the periodic potential is not invariant under the mirroring operation. One more way to reflect the lattice would be by placing the reflection point at a half-integer position, so that the reflection exchanges the two sublattices comprising odd and even positions. This transformation would map the potential to itself. Indeed, the parity operator reads

$$\hat{\hat{P}} = \begin{pmatrix} 0 & \hat{\sigma}_x \\ \hat{\sigma}_x & 0 \end{pmatrix} \otimes \sum_n |-n - 0.5\rangle \langle n + 0.5|, \tag{1.176}$$

where the inversion point is arbitrarily chosen as $n = -0.5$. The symmetry condition applying to the extended evolution operator comprising both sublattices simultaneously can be

47

found as

$$\delta_P \hat{\tilde{U}}_{1D} = 0, \text{only if } \theta_1 = \theta_2. \tag{1.177}$$

So, we see that the periodic potential with any φ respects the symmetry, however the couplers on both sublattices have to be equal.

2D two-component pseudospin walk

In two dimensions, the variety of the reflections is higher. If the system would be spatially continuous, the number of mirroring axes could be infinite. However, for the discrete 2D walk, there are only four such axes, namely the horizontal, the vertical and two diagonal ones. Let us first consider the first two in the extended evolution picture covering both sublattices simultaneously:

$$\hat{\tilde{P}}_p = \iint dk_n dk_p \ket{-k_n, k_p} \bra{k_n, k_p} \otimes \begin{pmatrix} \sigma_0 & \hat{0} \\ \hat{0} & \sigma_x \end{pmatrix}, \tag{1.178}$$

$$\hat{\tilde{P}}_n = \iint dk_n dk_p \ket{k_n, -k_p} \bra{k_n, k_p} \otimes \begin{pmatrix} \sigma_x & \hat{0} \\ \hat{0} & \sigma_0 \end{pmatrix}. \tag{1.179}$$

Seemingly, the network arrangement in Fig. 1.12a can lead us to the conclusion that those parity symmetries should be respected at least in the case of the absent potential ($\varphi = 0$). This is however not true and they are in fact always violated, because such a flip of the lattice (assuming that the state is fixed) is going to exchange the phase shifts acquired by the microscopic flows rotating in one and another direction. Indeed, assume one local component of a wave function, passing two beam splitters one after another, turns right two times on the lattice and acquires the phase shift of $\arg{(i^2)}$, while another constituent is propagating through the beam splitters and turns left two times, thus acquiring zero phase. It is clear that under the horizontal or the vertical mirroring, the phase shifts will exchange for these two paths and therefore the parity symmetries have to break. However, certain points in the reciprocal space can still be invariant under the inversions. It is interesting to note, that even the presence of chiral symmetry ($\theta_1 = \theta_2 = \pi/4$) is not able to repair the parity symmetries. Another possibility, one should not forget about, is to flip the lattice with respect to a horizontal or vertical line, passing through a half-integer position n or p, respectively. Given that all power flow directions would simply turn backwards under such reflection and the potential pattern in Fig. 1.12a obeys such a flip, this is a trivial transformation, which holds the respective symmetry for any Hamiltonian parameters.

Next, we proceed with diagonal flips. First, we distinguish reflection lines passing through positions with integer and half-integer values of $(n+p)/2$. According to Fig. 1.12a, the phase pattern will be reflection symmetric with respect to one of such two parallel lines. If one rotates them by 90 degree, than the pattern will be symmetric with respect to another line. So, without loss of generality, we can choose the lines passing through an integer diagonal position $(n+p)/2$. Then, the reflection would flip each of the two sublattices with $\mod{((|n|+|p|)/2, 2)} = 1$ and $\mod{((|n|+|p|)/2, 2)} = 0$, distinguish by the phase pattern, to itself. Therefore, the semi-extended stroboscopic picture (1.131), describing only one or another sublattice, can be used. Indeed, writing the parity operators in the this

representation of the evolution as

$$\hat{\tilde{P}}_{n+p} = \iint dk_n dk_p \, |k_p, k_n\rangle \, \langle k_n, k_p| \otimes \begin{pmatrix} \hat{0} & \sigma_0 \\ \sigma_0 & \hat{0} \end{pmatrix}, \tag{1.180}$$

$$\hat{\tilde{P}}_{n-p} = \iint dk_n dk_p \, |-k_p, -k_n\rangle \, \langle k_n, k_p| \otimes \begin{pmatrix} \hat{0} & \sigma_x \\ \sigma_x & \hat{0} \end{pmatrix}, \tag{1.181}$$

we can rigorously calculate that

$$\Delta_{\hat{\tilde{P}}_{n+p}} \hat{\tilde{U}}_{2D} = 0, \text{ only if } \theta_1 = \theta_2 \ \& \ \varphi = 0, \frac{\pi}{2}, \dots \tag{1.182}$$

$$\Delta_{\hat{\tilde{P}}_{n-p}} \hat{\tilde{U}}_{2D} = 0, \text{ only if } \theta_1 = \theta_2, \tag{1.183}$$

$$\Delta_{\hat{\tilde{P}}_{n+p}} \hat{\tilde{U}}'_{2D} = 0, \text{ only if } \theta_1 = \theta_2, \tag{1.184}$$

$$\Delta_{\hat{\tilde{P}}_{n-p}} \hat{\tilde{U}}'_{2D} = 0, \text{ only if } \theta_1 = \theta_2 \ \& \ \varphi = 0, \frac{\pi}{2}, \dots \tag{1.185}$$

where the evolution operator $\hat{\tilde{U}}_{2D}$ and $\hat{\tilde{U}}'_{2D}$ describes the sublattices with positions satisfying mod $(((|n| + |p|)/2, 2) = 0$ and mod $(((|n| + |p|)/2, 2) = 1$, respectively. Note, that although the parity transformations reverse the "microscopic" power flow in each unit cell, the phase shifts acquired by the clockwise and counter-clockwise trajectories exchange as well, meaning that the system as a whole remains unchanged and the problem, that occurred with the horizontal and vertical flips, does not appear here.

2D four-component pseudospin walk

To finalize the discussion of symmetries, we proceed with the two-dimensional walk of four-component pseudospinors. The horizontal and vertical reflection with respect to the lines that pass through a half-integer position n or p would simply exchange all power flow directions and leave the potential pattern unchanged as follows from Fig. 1.12b. Therefore, the system as a whole would not change and the thus the symmetry would be valid for any Hamiltonian. In contrast, if one flips the lattice with respect to a line with an integer position, thus exchanging only "up" and "down" or "left" and "right" components, then orthogonally oriented beam splitters would exchange their positions as one can infer from Fig. 1.5a. Therefore, although formally one gets again the initial lattice (at least without phase modulation), it will be shifted by one position in the vertical or horizontal position. It means the symmetry can never be fulfilled.

Next, we proceed with diagonal flips. In contrast to the previous walk and due to a different network type, diagonal parity transformations that exchange two sublattices, each hosting four components, lead to the inversion of power flows and eventually lead to the initial lattice (at least without phase modulation), but again shifted by some position. Therefore, we consider the diagonal flips that map each sublattice to itself, namely

$$\hat{\tilde{P}}_{n'} = \iint dk_{n'} \, |k_{p'}, -k_{n'}\rangle \, \langle k_{p'}, k_{n'}| \otimes \begin{pmatrix} \hat{0} & \hat{\sigma}_x \\ \hat{\sigma}_x & \hat{0} \end{pmatrix}. \tag{1.186}$$

$$\hat{\tilde{P}}_{p'} = \iint dk_{p'} dk_{n'} \, |-k_{p'}, k_{n'}\rangle \, \langle k_{p'}, k_{n'}| \otimes \begin{pmatrix} \hat{\sigma}_x & \hat{0} \\ \hat{0} & \hat{\sigma}_x \end{pmatrix}, \tag{1.187}$$

Thus, recalling the pseudospin structure from Fig. 1.12b, we can infer that the perpendicular diagonal mirroring axes should necessarily cross each other at some half-integer coordinates n and k (the middle of a unit cell). Consequently, the phase potential generally has to break both symmetries. Indeed, the symmetry conditions read

$$\Delta_{P_{n'}}\hat{U}_{2D} = 0, \ \text{only if} \ \varphi = 0, \frac{\pi}{2}, ... \tag{1.188}$$

$$\Delta_{P_{p'}}\hat{U}_{2D} = 0, \ \text{only if} \ \varphi = 0, \frac{\pi}{2}, ... \tag{1.189}$$

Note, that the symmetry does not impose any restrictions on the coupling coefficients, again supporting the idea that the network is strongly achiral in comparison to other walks.

1.7 Topological classification and bulk-edge correspondence

Topological insulators (TI) and superconductors (TSCs) are by definition gapped phases of bulk noninteracting fermions, whose ground state wavefunctions are characterized by nontrivial topological invariants, which are caused by certain intrinsic symmetries of the system. A great variety of such symmetry protected topological phases has been arranged into a periodic table and classified according to the celebrated Atland-Zinbauer (AZ) 10-fold symmetry classification [65–67]. One fundamental consequence of the topology is that a finite gapped bulk of a topologically non-trivial material can host gapless states at its interface, where the topological phase (and the invariant) is abruptly changing. The states are protected against disorders respecting that symmetry of the bulk and they can host or conduct particles in a robust way. The special case is the boundary (edge) state occurring between a topologically non-trivial bulk and trivial vacuum. The topological invariant is the characteristic of an infinite bulk. Therefore, a topologically non-trivial structure of the infinite bulk is responsible for the existence and protection of a localized boundary state hosted in a lower dimension, the principle known as bulk-edge correspondence. The concept has been extended even further towards strongly and weakly topologically protected defects in crystalline phases [68], TIs and TSCs [69], boundary states and Fermi surfaces in gapless phases of semimetals and nodal lines in semiconductors [70, 71].

The discrete quantum walks (DQWs) of a single photon (or light walks of a coherent optical wave) can be also classified within the framework of non-interacting TIs and TCSs, as soon as there is no quantum (or classical nonlinear) interaction between the photons. In what follows, we will identify topological phases of the walks based on AZ classes. We will also see, that the basic topological classes can be noticeably enriched in the presence of a reflection symmetry [71–74] as well as due to the Floquet periodicity of the systems, which can effectively double the number of gaps and the number of topological invariants [75–77] and eventually can lead to anomalous topological edge states [78–80]. The reflection symmetry, alone or in combination with other symmetries, can lead to additional "mirror" topological invariants $M\mathbb{Z}$, that can protect boundary states or Fermi points and lines in the reciprocal space, that are invariant under the reflection. The extra topological number, in contrast to the conventional ones predefined by TRS, PHS and chiral symmetries, can be defined also for gapless systems and characterize the topology of their Fermi points and lines. Further on, we find it more instructive to discuss all systems in total, rather than treating them separately. In particular, we summarize all the obtained symmetry classes

and associated topological invariants in Table 1.1.

First of all, one can notice that in the extended pictures, implying $\hat{\tilde{U}} \in SU(2) \otimes SU(2)$, the two-component 1D and 2D walks have time-reversal symmetry operators that can square to +1 or -1. It means that the pseudospin can not be directly associated with a half-integer $(\hat{T}_+^2 = -1)$ or an integer $(\hat{T}_+^2 = +1)$ spin. In addition, the two-dimensional walk in the stroboscopic representation can obey TRS operators with both signs simultaneously. We expect, that this ambiguity can be resolved in the most extended picture $U \in SU(2) \otimes SU(2) \otimes SU(2) \otimes SU(2)$, covering all sublattices. Recall, that in the previous section 1.4 we calculated the Berry phase around the Dirac points at $\varphi = \pi/2$ and $k = 0$ for the 1D and 2D systems. In both walks, the obtained Berry phase was $+\pi$ and $-\pi$ for the upper and the lower band, respectively. This is in agreement with DIII phase (see Table 1.1), which predicts a binary invariant $\mathbb{Z}$ for both walks. The four-component pseudspin walk, in contrast, supports only TRS squared to +1 and thus can be associated with an integer spin. So, in approving this generic result, we can recall that the Berry phase found around the degeneracy point at $\varphi = 0$ and $k = 0$ is 0 for both bands, meaning that the four-component pseudospin indeed behaves as an integer spin. On the other hand, the value of 0 does not indicate the non-trivial topological invariant $\mathbb{Z}$, which is predicted by the topological class A (see Table 1.1). To emphasize the difference between the four-component and the two-component pseudospin walks even more, we note that the first one covers only standard Wigner-Dyson (A,AI) and chiral (BDI) classes, while the latter two also cover Bogoliubov-de Gennes classes (D, DIII), typically associated with non-interacting fermionic quasiparticles in superconductors. Among well-studied systems in the Wigner-Dyson symmetry class are random matrix models for weakly disordered time-reversal invariant metals and Anderson tight-binding models with real hopping and strong disorder. By adding chiral symmetry to the standard class, one comes up with chiral classes, typically describing tight-binding models on a bipartite lattice, such as, for example, Su-Schrieffer-Heeger (SSH) model.

Secondly, it is worth mentioning that stroboscopic and instantaneous Hamiltonians cover different topological classes, mainly because the stroboscopic evolution is generally less "sensitive" to temporally microscopic symmetry breakings. In particular, the stroboscopic BDI (AI) class of the 1D walk parametrically contains BDI, DIII and D (AI and A) classes of the instantaneous Hamiltonian. The stroboscopic BDI class of the four-component 2D walk includes BDI and AI classes of the instantaneous walk. Given a defect, an interface or a boundary can be described within the stroboscopic Floquet picture, one is allowed to use the reduced table of symmetry classes and corresponding topological invariants, in order to predict the existence of a topological state according to bulk-edge correspondence. However, one should bear in mind that the topological protection of the state in the Floquet framework would work only against static local disorders, that respect a certain intrinsic symmetry, which is valid in the stroboscopic picture, or against local disorders, that are varying in time not faster than the periodic Floquet drive and also obey that symmetry. Otherwise, one has to deal with the instantaneous Hamiltonian, which generally can protect a boundary or defect state against a larger class of disorders, but may impose more demanding constraints for the Hamiltonian parameters for the symmetry to be preserved, according to the topological classification in Table 1.1. For example, chiral symmetry in the instantaneous picture of the 1D system is imposing additional constraints on $\theta_{1,2}$ (in the table $\mathbb{A} \stackrel{\text{def}}{=\!=} \pi/4 + \pi N$, $N \in \mathbb{Z}$), while in the instantaneous picture of the 2D four-component system, chiral symmetry is not valid anymore for $\varphi = \pi/2, 3\pi/2, ...$ One more comment to be made on the stroboscopic Floquet systems is that the evolution operator in this picture can be defined ambiguously from the dynamical point of view. Indeed, in 1D one can rotate the time frame, so that

the rotation effectively exchanges the parameters $\theta_1 \Longleftrightarrow \theta_2$, $\varphi \longrightarrow \varphi$, in 2D systems it also exchanges the orthogonal position axes $n \longrightarrow p$. It is easy to see that such a rotation in the stroboscopic picture leads to the same dynamical properties of the bulk, because it is only changing the reference time frame. However, from the topological point of view, such a rotation is not trivial as it can lead another topological invariant, thus making a topologically trivial system non-trivial and vice versa. Indeed, we see in Table 1.1 that the exchange of parameters does not bring the system to another topological class, but nevertheless it can change the topological invariant. Thus, the number of topological invariants attributed to a particular stroboscopic Floquet system has to be doubled, as has also been proven in [75]. The doubling of the invariants is indicates as $\times 2$. Note that the topological property (which of the two invariants to choose) remains abstract and degenerate on the physical level, until, for example, a boundary or a defect is introduced to the system, which resolves the ambiguity, allowing one to uniquely choose one of the two Floquet time frames, where the defect/boundary obeys the intrinsic symmetries of the bulk. Later in section 3.2, we discuss such a situation for the 1D lattice in more details. On the other hand, the instantaneous pictures do not presume such an ambiguity since the reference time frame is unique.

Now, we comment on the reflection symmetry, which in addition to the basic topological invariants, is able to impose the so-called mirror invariants $M\mathbb{Z}$ and $M\mathbb{Z}_2$, according to [71] and [72]. First, we discuss the 1D system. The instantaneous description, including both sublattices, allows for a lattice reflection with respect to a half-integer position. The system is compatible with such a reflection as soon as $\theta_1 = \theta_2$. Due to the latter condition, one can not introduce a defect or a boundary to the lattice, using the coupling. Therefore, the only possibility within the generalized model is to introduce a phase defect by varying φ. According to, for example, [72], for the defect to be topologically protected by the mirror invariant, it has to be symmetric with respect to the symmetry. The simplest example is just a single point-like phase defect φ_0 localized at some half-integer position. Note, however, that if the bulk has $\varphi \in \mathbb{B}_{\pi/2}$, where $\mathbb{B}_{\pi/2} \overset{\text{def}}{=\!=} \frac{\pi}{2}, \frac{3\pi}{2}, ...$ (class DIII and partly class D), then the system is gapless in the center of the Brillouine zone and such a state can not be protected by $\mathbb{Z}_2$ and $M\mathbb{Z}_2$. Instead, $M\mathbb{Z}_2$ can only protect Dirac points, or more generally Fermi surfaces of zero dimension [71], that are mirror symmetric points in the Brillouine zone. On the other hand, BDI class and another part of D class of the extended instantaneous picture can protect such a defect mode by $\mathbb{Z} \oplus M\mathbb{Z}$ and $M\mathbb{Z}$, respectively, because the system is gapped in the center of Brillouine zone.

Next, in the stroboscopic picture of the 1D system, one can describe the reflection symmetry with respect to an integer position, which does not impose any condition on the couplings, but instead requires that $\varphi \in \mathbb{B}_0$, $\mathbb{B}_{\pi/2}$, where $\mathbb{B}_{\pi/2}$ is defined above and $\mathbb{B}_0 \overset{\text{def}}{=\!=} 0, \pi, ...$ Naturally, the defect compatible with such a symmetry could be a single-site interface between lattice regions with different couplings or simply a termination (edge) of the lattice $\varphi = \pi/2$, so that the region beyond the edge can be considered as a topologically trivial vacuum. If the regions on one and another side of the interface are topologically distinct or the terminated bulk is topologically non-trivial, then one can expect the existence of a topologically protected state localized at the defect, according to bulk-edge correspondence. If the spatial profile of the coupling φ_n at the interface or the edge is arbitrary, then the state should be protected by the basic integer invariant $\mathbb{Z}$. If, however, the profile respect the parity symmetry (an adjoint mirror symmetric terminated lattice can be always presumed beyond the edge), then the additional mirror invariant $M\mathbb{Z}$ is also responsible for the protection. Note, however that since the reflection symmetry brakes together with chiral symmetry due to an arbitrary phase amplitude φ, the former one does not add any additional robustness

for the state protection.

Finally, we briefly discuss the role of reflection symmetries for the 2D systems. As an example, we chose diagonal flips, although one could also concentrate on the horizontal and vertical flips, that are compatible with any lattice parameters. Interestingly, the diagonal reflection symmetry does not bring any additional protection in the 2D four-component pseudospin network. In contrast, the 2D two-component pseudspin walk allows for a reflection symmetry protection $M\mathbb{Z}$ in the chiral BDI class and partly in DIII class, where most likely φ has to belong to $\mathbb{B}_0$, but it is not possible to resolve it within the stroboscopic picture. On the other hand, the binary mirror invariants $M\mathbb{Z}_2$ appearing in class D and partly in DIII, can only protect the Dirac point in the middle of the Brillouine zone, which close the central gap. Indeed, one can explicitly check that the gap remains always closed at the Dirac point as soon as $\theta_1 = \theta_2$ and $\varphi \in \mathbb{B}_0, \mathbb{B}_{\pi/2}$. This is the case, even if time-reversal symmetry brakes (class D). However, the basic invariant $\mathbb{Z}$ in classes D and A work only for gapped systems ($\theta_1 \neq 0$) or ($\varphi \notin \mathbb{B}_0, \mathbb{B}_{\pi/2}$) and therefore it is not compatible with $M\mathbb{Z}_2$. We emphasize that in order to be protected, a defect or a Dirac (Fermi) point has to be symmetric with respect to the one of the two orthogonal diagonal flips, that is specifically indicated by the subscript $P^{\nu_{T_+}\nu_{T_-}}$ above the respective mirror invariant. Using the conventional notations in [71] and [72], the signatures ν_{T_+} and ν_{T_-} are defined via

$$\hat{P}\hat{T}_+ = \nu_{T_+}\hat{T}_+\hat{P}, \tag{1.190}$$

$$\hat{P}\hat{T}_- = \nu_{T_-}\hat{T}_-\hat{P}, \tag{1.191}$$

where all of the symmetry operators have to be compatible, i.e. they have to be chosen in accordance with one of the evolution pictures.

Discrete Walk	Picture (period)	Symmetries				Conditions	AZ class	Top. invariant
		χ	T_-^2	T_+^2	P			
D=1	Full $U \in SU(2)$ $\otimes SU(2)$ (M=1)	✓	+1	+1	✓P^{+-} ($\theta_1 = \theta_2$)	$\theta_1, \theta_2 \in \mathbb{A}$, $\varphi \in \mathbb{B}_0$	BDI	$\mathbb{Z} \oplus M\mathbb{Z}$
		✓	+1	-1	✓P^{-+} ($\theta_1 = \theta_2$)	$\theta_1, \theta_2 \in \mathbb{A}$, $\varphi \in \mathbb{B}_{\pi/2}$	DIII	$\mathbb{Z}_2 \oplus M\mathbb{Z}_2$
		✗	+1	✗	✓P^{+-} ($\theta_1 = \theta_2$)	$\theta_1, \theta_2 \notin \mathbb{A}$, $\varphi \in \mathbb{B}_0$	D	$M\mathbb{Z}^{P\times-}$
		✗	+1	✗	✓P^{-+} ($\theta_1 = \theta_2$)	$\theta_1, \theta_2 \notin \mathbb{A}$, $\varphi \in \mathbb{B}_{\pi/2}$		$M\mathbb{Z}_2^{P\times-}$
		✓	✗	✗	✓P^- ($\theta_1 = \theta_2$)	$\theta_1, \theta_2 \in \mathbb{A}$, $\varphi \notin \{\mathbb{B}_0, \mathbb{B}_{\pi/2}\}$	AI	✗
		✗	✗	✗	✓P ($\theta_1 = \theta_2$)	$\theta_1, \theta_2 \notin \mathbb{A}$, $\varphi \notin \{\mathbb{B}_0, \mathbb{B}_{\pi/2}\}$	A	$M\mathbb{Z}$
	Strobo $U \in SU(2)$ (M=2)	✓	+1	+1	✓P^{+-}	$\varphi \in \{\mathbb{B}_0, \mathbb{B}_{\pi/2}\}$	BDI	$(\mathbb{Z} \oplus M\mathbb{Z}) \times 2$
		✗	✗	✓	✗	$\varphi \notin \{\mathbb{B}_0, \mathbb{B}_{\pi/2}\}$	AI	✗
D=2, Walk I	Strobo $U \in SU(2)$ $\otimes SU(2)$ (M=2)	✓	+1	+1	✓$P^{+\pm}$ ($\theta_1 = \theta_2$)	$\theta_1, \theta_2 \in \mathbb{A}$, $\varphi \in \{\mathbb{B}_0, \mathbb{B}_{\pi/2}\}$	BDI	$M\mathbb{Z}^{P^{++}} \times 2$
		✓	+1	-1	✓$P^{-\mp}$ ($\theta_1 = \theta_2$)		DIII	$(\mathbb{Z}_2 \oplus M\mathbb{Z}^{P^{--}}$ $\oplus M\mathbb{Z}_2^{P^{-+}}) \times 2$
		✗	✗	+1	$P^{+\times}$ ($\theta_1 = \theta_2$)	$\theta_1, \theta_2 \in \mathbb{A}$, $\varphi \notin \{\mathbb{B}_0, \mathbb{B}_{\pi/2}\}$	AI	✗
		✗	✗	-1	$P^{-\times}$ ($\theta_1 = \theta_2$)		AII	$\mathbb{Z}_2 \times 2$
		✗	+1	✗	$P^{\times\pm}$ ($\theta_1 = \theta_2$)	$\theta_1, \theta_2 \notin \mathbb{A}$, $\varphi \in \{\mathbb{B}_0, \mathbb{B}_{\pi/2}\}$	D	$(\mathbb{Z} \oplus M\mathbb{Z}_2^{P^{\times+}}) \times 2$
		✗	✗	✗	P ($\theta_1 = \theta_2$)	$\theta_1, \theta_2 \notin \mathbb{A}$, $\varphi \notin \{\mathbb{B}_0, \mathbb{B}_{\pi/2}\}$	A	$\mathbb{Z} \times 2$
D=2, Walk II	Full $U \in SU(4)$ $\otimes SU(4)$, (M=1)	✓	+1	+1	✓$P^{+,-}$	$\varphi \in \mathbb{B}_0$	BDI	✗
		✗	✗	+1	✓$P^{-,\times}$	$\varphi \in \mathbb{B}_{\pi/2}$	AI	✗
		✗	✗	✗	✗	$\varphi \notin \{\mathbb{B}_0, \mathbb{B}_{\pi/2}\}$	A	$\mathbb{Z}$
	Strobo $U \in SU(4)$ $\otimes SU(4)$, (M=2)	✓	+1	+1	✓$P^{\pm,-}$	$\varphi \in \{\mathbb{B}_0, \mathbb{B}_{\pi/2}\}$	BDI	✗
		✗	✗	✗	✗	$\varphi \notin \{\mathbb{B}_0, \mathbb{B}_{\pi/2}\}$	A	$\mathbb{Z} \times 2$

Table 1.1: Topological classification of the beam splitter based 1D and 2D walks.

1.8 $\mathcal{PT}$ symmetry and pseudo-Hermitian evolution

In conclusion of the extended theoretical overview of 1D and 2D beam splitter based discrete quantum walks, we consider one more extension of the system, which also can be implemented with time-multiplexed platforms, designed specifically for coherent light pulses with many photons. Namely, the optical power can be dynamically amplified and attenuated, thus making the system open and non-Hermitian, i.e.

$$\hat{H} \neq \hat{H}^{\dagger}. \tag{1.192}$$

Generally, any disbalance between the introduced gain and loss of the power lead to an exponential explosion or attenuation of the field. However, first seminal works by Bender and Boettcher [8, 9] showed that a judicious distribution of gain and loss regions in the system can conversely lead to a quasiconservative evolution, meaning that while the instantaneous total power can in general periodically oscillate in time, its averaged value remains constant during propagation.The key (although in general neither sufficient nor necessary) prerequisite for the quasiconservative evolution is the compatibility of the system with $\hat{P}\hat{T}_{+}$-symmetry:

$$\hat{P}\hat{T}_{+}\hat{H}\hat{P}\hat{T}_{+} = \hat{H} \iff \hat{P}\hat{T}_{+}\hat{U}\hat{P}\hat{T}_{+} = \hat{U}^{-1}. \tag{1.193}$$

A steadily growing interest to such quasiconservative systems is explained, besides the realness of the eigenspectrum, by the associated peculiar phenomena, such as unidirectional reflectionless resonances [81, 82], Bloch power oscillations [59, 83, 84], unidirectional invisibility [85, 86], enhanced sensitivity at exceptional points [87–89] and anomalous edge states in topological superconductors [90]. Moreover, the most recent advances in the topological classification of non-Hermitian systems report unique topological phases with no symmetry consraint and bulk-edge correspondence, which have no Hermitian counterparts [91, 92].

Another concept argues that a non-Hermitian system with a completely real eigenvalue spectrum should necessarily satisfy the condition called pseudo-Hermiticity [93], which is by definition

$$\hat{\eta}\hat{H}^{\dagger}\hat{\eta}^{-1} = \hat{H} \iff \hat{\eta}\hat{U}^{\dagger}\hat{\eta}^{-1} = \hat{U}^{-1}, \tag{1.194}$$

where $\hat{\eta}$ is a Hermitian linear automorphism. Not every pseudo-Hermitian Hamiltonian is $\hat{P}\hat{T}_{+}$-symmetric, however every $\hat{P}\hat{T}_{+}$-symmetric Hamiltonian with finite dimensions is pseudo-Hermitian. As we will see later on, in our DQW systems pseudo-Hermiticity is typically satisfied with $\hat{\eta} = \hat{P}$, if the system is parity-time symmetric. Parity-time symmetry of a quasiconservative Hamiltonian with real eiganvalues can spontaneously break, meaning that its eigenvalues at some quasimomentum can turn complex when the Hamiltonian parameters (phase amplitude and coupling in our case) are tuned to certain values. The point of breaking is typically appears as a degeneracy point, where two bands begin merging. The point is commonly called exceptional point, because in contrast to degeneracy points of Hermitian systems, the eigenmodes of the merging bands in the pseudo-Hermitian ones coalesce, implying a dimensionality collapse of the Hilber space at that point. If one tunes the Hamiltonian parameters to merge the bands further the absolute values of the imaginary parts of the eigenvectors and the quasimomentum region of broken $\hat{P}\hat{T}_{+}$-phase both grow higher, while the real part of the eigenenergies remain flat and degenerate within the broken region. This is the typical scenario, that we always observed in the DQWs respecting a parity-time symmetry. In what follows, we give a brief overview of the pseudo-Hermitian

systems.

1.8.1 $\mathcal{PT}$ symmetry in 1D

Original Walk

First, we discuss the $\mathcal{PT}$-symmetric gain/loss and phase distribution, which was first introduced in [85] for the one-dimensional system and is schematically shown in Fig. 1.17b. Obviously, neither time-reversal nor parity symmetry with respect to an integer position are satisfied. However, their combination does. Indeed, representing the elementary pseudospin within the unit cell (the rectangular outline) extended due to the phase modulation as

$$|k\rangle = \begin{bmatrix} l_1(k) & r_1(k) & l_2(k) & r_2(k) \end{bmatrix}^{\mathrm{T}} \otimes \sum_{\mathrm{mod}\,(n,4)=1} e^{-nk} |n\rangle, \qquad (1.195)$$

we can write the evolution operator as

$$\hat{\hat{U}}_{1D}(k) = \hat{\hat{G}}(+g)\hat{\hat{\Phi}}(0,-\varphi)\hat{\hat{S}}(-k)\hat{\hat{C}}_2\hat{\hat{G}}(+g)\hat{\hat{\Phi}}(+\varphi,0)\hat{\hat{S}}(k)\hat{\hat{C}}_1, \qquad (1.196)$$

$$\hat{\hat{C}}_2 \stackrel{\mathrm{def}}{=\!=} \frac{1}{\sqrt{2}}\begin{pmatrix} i & 1 & 0 & 0 \\ 1 & i & 0 & 0 \\ 0 & 0 & i & 1 \\ 0 & 0 & 1 & i \end{pmatrix}, \quad \hat{\hat{C}}_1 \stackrel{\mathrm{def}}{=\!=} \frac{1}{\sqrt{2}}\begin{pmatrix} i & 0 & 0 & 1 \\ 0 & i & 1 & 0 \\ 0 & 1 & i & 0 \\ 1 & 0 & 0 & i \end{pmatrix}, \qquad (1.197)$$

$$\hat{\hat{S}}(k) \stackrel{\mathrm{def}}{=\!=} \frac{1}{\sqrt{2}}\begin{pmatrix} e^{ik} & 0 & 0 & 0 \\ 0 & e^{-ik} & 0 & 0 \\ 0 & 0 & e^{ik} & 0 \\ 0 & 0 & 0 & e^{-ik} \end{pmatrix}, \quad \hat{\hat{G}}(g) \stackrel{\mathrm{def}}{=\!=} \begin{pmatrix} e^{+g} & 0 & 0 & 0 \\ 0 & e^{-g} & 0 & 0 \\ 0 & 0 & e^{g} & 0 \\ 0 & 0 & 0 & e^{-g} \end{pmatrix}, \; g \in \mathbb{R} \qquad (1.198)$$

$$\hat{\hat{\Phi}}(\varphi_1,\varphi_2) \stackrel{\mathrm{def}}{=\!=} \begin{pmatrix} e^{i\varphi_1} & 0 & 0 & 0 \\ 0 & e^{i\varphi_2} & 0 & 0 \\ 0 & 0 & e^{-i\varphi_1} & 0 \\ 0 & 0 & 0 & e^{-i\varphi_2} \end{pmatrix}, \; \varphi_{1,2} \in \mathbb{R}, \qquad (1.199)$$

where the newly introduced parameter g is responsible for the amplification $\sim e^g$ and attenuation $\sim e^{-g}$. In order to find the parity-time symmetry operator, it is practical to rotate the reference time frame to the chiral symmetric one introduced earlier

$$\hat{\hat{U}}'_{1D} = \hat{\hat{C}}_1^{\frac{1}{2}}\hat{\hat{U}}_{1D}\hat{\hat{C}}_1^{\frac{1}{2}}, \qquad (1.200)$$

$$\hat{\hat{C}}_1^{\frac{1}{2}} = \begin{pmatrix} i\sin\pi/8 & 0 & 0 & \cos\pi/8 \\ 0 & i\sin\pi/8 & \cos\pi/8 & 0 \\ 0 & \cos\pi/8 & i\sin\pi/8 & 0 \\ \cos\pi/8 & 0 & 0 & i\sin\pi/8 \end{pmatrix}. \qquad (1.201)$$

Then, combining the previously found parity and time-reversal operators

$$\hat{P} = \int_k dk\, |-k\rangle\langle k| \otimes \begin{pmatrix} 0 & \hat{\sigma}_x \\ \hat{\sigma}_x & 0 \end{pmatrix}, \quad \hat{T}_+ = \int_k dk\, |-k\rangle\langle k| \otimes \begin{pmatrix} 0 & \hat{\sigma}_x \\ \hat{\sigma}_x & 0 \end{pmatrix} K, \qquad (1.202)$$

which separately are not respected, we find that for all Hamiltonian parameters

$$\hat{P}\hat{T}_+ = \int_k dk \, |k\rangle \langle k| \otimes \begin{pmatrix} \hat{\sigma}_0 & 0 \\ 0 & \hat{\sigma}_0 \end{pmatrix} K, \ \ \hat{P}\hat{T}_+ \, \hat{U}'_{1D}\hat{P}\hat{T}_+ = \hat{U}'^{-1}_{1D}. \tag{1.203}$$

Also, note that the pseudo-Hermiticity holds as well

$$\hat{P}\,\hat{U}'^{\dagger}_{1D}\hat{P}^{-1} = \hat{U}'^{-1}_{1D}. \tag{1.204}$$

In general, if parity-symmetry breaks for some eigenvalues, then corresponding eigenmodes can not be simultaneously an eigenmodes for $\hat{P}\hat{T}_+$ operator, even though it commutes with the Hamiltonian. Nevertheless, the Hamiltonian of the walk can always be diagonalized and the following four bands can be found

$$E_{1,2} = \pm\frac{1}{2}\arccos\left(\frac{-\cos\varphi\cos 2gi}{2} - \frac{\sqrt{5 - 3\cos 2\varphi + 2\cos 4k - 2\cos 4gi\sin^2\varphi}}{4}\right), \tag{1.205}$$

$$E_{3,4} = \pm\frac{1}{2}\arccos\left(\frac{-\cos\varphi\cos 2gi}{2} + \frac{\sqrt{5 - 3\cos 2\varphi + 2\cos 4k - 2\cos 4gi\sin^2\varphi}}{4}\right). \tag{1.206}$$

Below in Fig. 1.17a, we provide examples of the fully real spectrum of quasienergies as well as partly complex ones, corresponding to spontaneously broken parity-time symmetry phase. The entire phase diagram of broken and recovered phases is shown in Fig. 1.17c. Now, the role of the phase modulation is clear, because for the unmodulated lattice the parity-time symmetry breaks immediately. One can see that for some parametric regions the phase brakes only for one symmetric pair of bands (bright blue areas), while for approximately $|g| > 0.44$ the positive and the negative bands merge pairwise and the symmetry breaks at any φ (yellow and green regions). Thus, there is a universal gain/loss threshold, which once exceeded does not allow to recover the all-real spectrum of quasienergies. This is a typical scenario for systems based on Schrödinger or paraxial wave equation [94], including all the quantum walks under study .
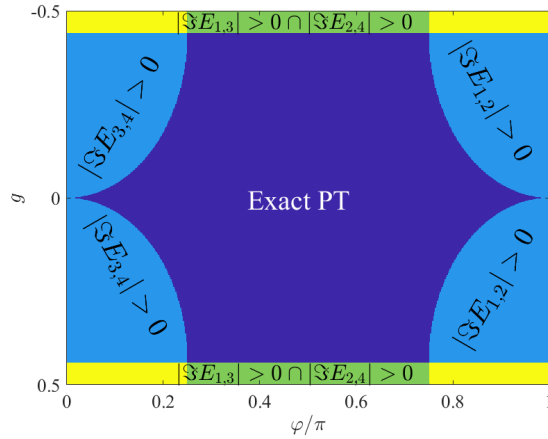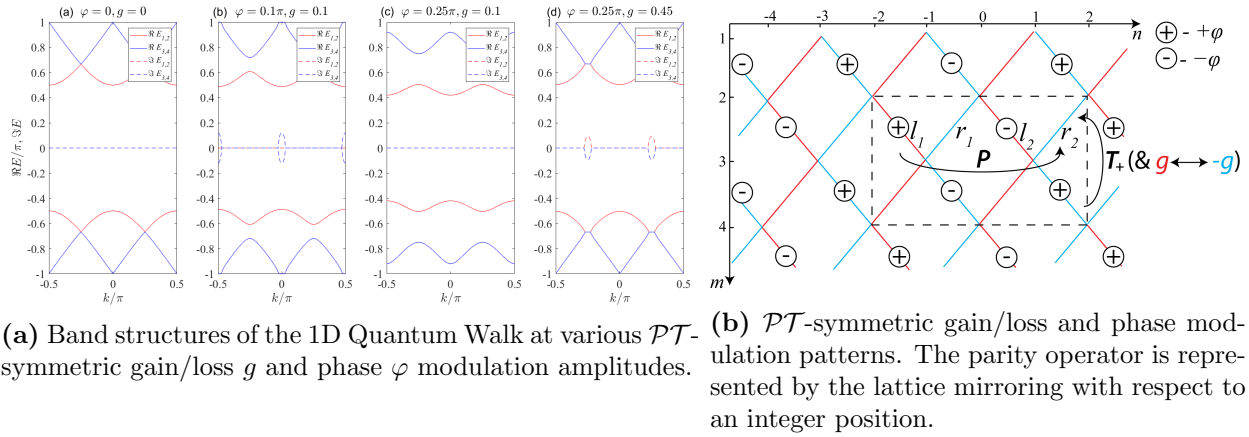
1D Walk with periodically twisted ports

Interestingly, if one changes the underlying topology of the network without changing the spatial profiles of parity-time symmetric gain/loss and phase modulations, one will get very different phase diagram, although the upper threshold will remain exactly the same. Indeed, let us twist output ports of beam splitters at every second time step, while leaving the spatial distribution of the complex potential the same as in the previous example (Fig. 1.17b). To do so, we write the evolution matrix as follows

$$\hat{U}_{1D}(k) = \hat{G}(-g)\hat{\Phi}(0,-\varphi)\hat{S}(k)\hat{C}_2\hat{G}(+g)\hat{\Phi}(+\varphi,0)\hat{S}(k)\hat{C}_1, \tag{1.207}$$

where previously introduced elementary operators are used. Then, the dispersion relation reads as

$$E_{1,2} = \pm\frac{1}{2}\arccos\left(\frac{-\cos\varphi\cos 2k}{2} - \frac{\sqrt{5 - 3\cos 2\varphi + 2\cos 4ig - 2\cos 4k\sin^2\varphi}}{4}\right), \tag{1.208}$$

$$E_{3,4} = \pm\frac{1}{2}\arccos\left(\frac{-\cos\varphi\cos 2k}{2} + \frac{\sqrt{5 - 3\cos 2\varphi + 2\cos 4ig - 2\cos 4k\sin^2\varphi}}{4}\right). \tag{1.209}$$

(a) Band structures of the 1D Quantum Walk at various $\mathcal{PT}$-symmetric gain/loss g and phase φ modulation amplitudes.

(b) $\mathcal{PT}$-symmetric gain/loss and phase modulation patterns. The parity operator is represented by the lattice mirroring with respect to an integer position.


(c) Phase diagram of $\mathcal{PT}$-symmetric recovered (blue), partly recovered (light blue) and broken (yellow, green) regimes.

Figure 1.17

Note that the new band structure can be transformed into the old one by permuting $ig \Longleftrightarrow k$. As shown in Fig. 1.18a both symmetric pairs of bands break simultaneously at their respective degeneracy points $E = 0$ and $E = \pi$, as soon as the gain/loss parameter reaches the parametrized threshold value, which we can also derive analytically as

$$|g|_{\mathrm{thr}} = \min\left(\frac{\arccos(7 \pm 8\cos\varphi + 2\cos 2\varphi)}{4i}, \frac{\arccos(5.5 \pm 4\cos\varphi + 2\cos 2\varphi)}{4i}\right). \quad (1.210)$$

As already mentioned above, the system obeys the same upper threshold $g \approx \pm 0.44$ as the original walk (see Fig. 1.18b). We attribute this coincidence to the fact that in both cases the pseudo-Hermiticity is imposed by exactly the same parity-time symmetric complex potential, despite the different underlying topologies of the networks. In what follows, we further construct another parity-time symmetric potential, where that threshold value is not valid anymore.
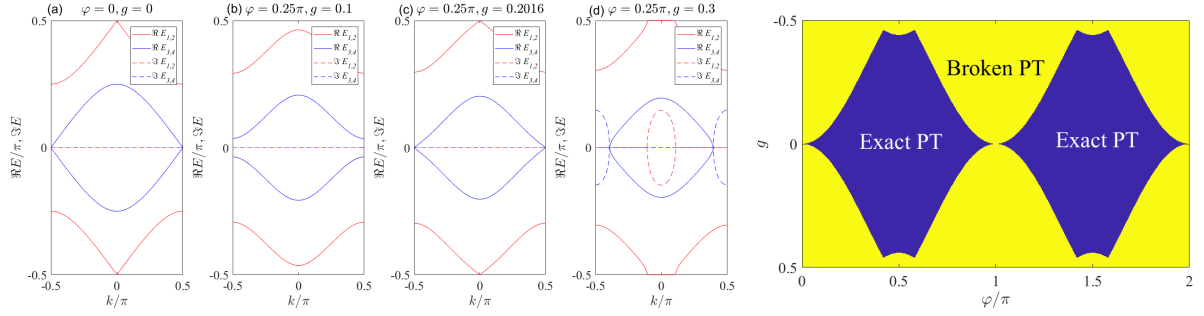
(a) Band structures of the 1D walk with twisted ports and different $\mathcal{PT}$-symmetric potential configurations.

(b) Recovered and broken $\mathcal{PT}$-symmetric phases of the 1D walk with twisted ports.

Figure 1.18

1D Walk with coupled sublattices

In order to construct another parity-time symmetric potential, we turn to a more exotic modification of the lattice. A closer look at the (1+1)D lattice shows that none of the phase potential patterns can satisfy parity-time symmetry, if the constituent parity operator flips the lattice with respect to a half-integer position. However, if we modify the lattice, so that otherwise independent sublattices with odd and even position become linked via modified periodic conditions, then such parity-time symmetric potential exists, as shown in Fig. 1.19b. Indeed, the elementary pseudspin of the system comprises 6 components

$$|k\rangle = \begin{bmatrix} l_1(k) & c_1(k) & r_1(k) & l_2(k) & c_2(k) & r_2(k) \end{bmatrix}^{\mathrm{T}} \otimes \sum_{\mathrm{mod}\,(n,3)=1} e^{-nk}\,|n\rangle \tag{1.211}$$

and the evolution operator reads

$$\hat{U}_{1D}(k) = \hat{G}(-g)\hat{\Phi}(-\varphi)\hat{S}(k)\hat{C}\hat{G}(+g)\hat{\Phi}(+\varphi)\hat{S}(k)\hat{C}, \tag{1.212}$$

$$\hat{\hat{C}} \stackrel{\mathrm{def}}{=\!=} \frac{1}{\sqrt{2}} \begin{pmatrix} 0 & 0 & 1 & i & 0 & 0 \\ 0 & 0 & 0 & 0 & i & 1 \\ 0 & 0 & 0 & 0 & 1 & i \\ i & 1 & 0 & 0 & 0 & 0 \\ 1 & i & 0 & 0 & 0 & 0 \\ 0 & 0 & i & 1 & 0 & 0 \end{pmatrix}, \quad \hat{S}(k) \stackrel{\mathrm{def}}{=\!=} \begin{pmatrix} e^{ik} & 0 & 0 & 0 & 0 & 0 \\ 0 & e^{-ik} & 0 & 0 & 0 & 0 \\ 0 & 0 & e^{ik} & 0 & 0 & 0 \\ 0 & 0 & 0 & e^{-ik} & 0 & 0 \\ 0 & 0 & 0 & 0 & e^{ik} & 0 \\ 0 & 0 & 0 & 0 & 0 & e^{-ik} \end{pmatrix}, \tag{1.213}$$

$$\hat{G}(g) \stackrel{\mathrm{def}}{=\!=} \begin{pmatrix} e^{g} & 0 & 0 & 0 & 0 & 0 \\ 0 & e^{-g} & 0 & 0 & 0 & 0 \\ 0 & 0 & e^{g} & 0 & 0 & 0 \\ 0 & 0 & 0 & e^{-g} & 0 & 0 \\ 0 & 0 & 0 & 0 & e^{g} & 0 \\ 0 & 0 & 0 & 0 & 0 & e^{-g} \end{pmatrix}, \quad \hat{\Phi}(\varphi) \stackrel{\mathrm{def}}{=\!=} \begin{pmatrix} e^{i\varphi} & 0 & 0 & 0 & 0 & 0 \\ 0 & 1 & 0 & 0 & 0 & 0 \\ 0 & 0 & e^{-i\varphi} & 0 & 0 & 0 \\ 0 & 0 & 0 & e^{-i\varphi} & 0 & 0 \\ 0 & 0 & 0 & 0 & 1 & 0 \\ 0 & 0 & 0 & 0 & 0 & e^{i\varphi} \end{pmatrix}, \quad g,\varphi \in \mathbb{R}. \tag{1.214}$$
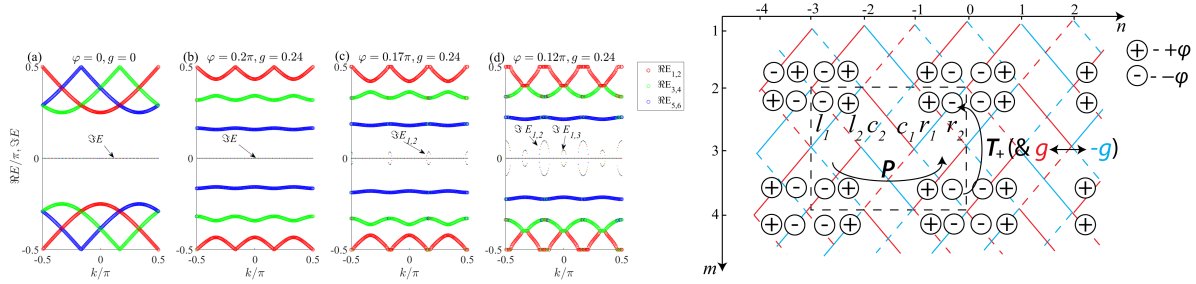
(a) Band structures of the 1D walk with entangled sublattices and different $\mathcal{PT}$-symmetric potential configurations.

(b) The 1D network with entangled sublattices and $\mathcal{PT}$-symmetric potential. The system is invariant under the action of time-reversal and the lattice mirroring with respect to the half-integer position.
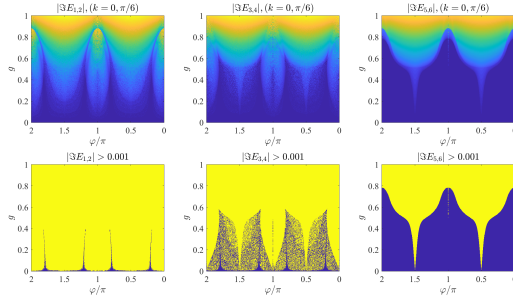
(c) Phase diagrams for pairwise symmetric bands of the $\mathcal{PT}$-symmetric 1D walk with entangled sublattices. Diagrams in the lower row are binary version of the opposite gradual diagrams in the upper row.

Figure 1.19

The general expressions for quasienergies are cumbersome, therefore we provide the analytical result only for the special case of unmodulated lattice ($\varphi = 0$):

$$E_{1,2} = \pm\frac{1}{2}\arccos\frac{\cos 2k - \cos 2ig}{2}, \tag{1.215}$$

$$E_{3,4} = \pm\frac{1}{2}\arccos\frac{-\cos 2k - \cos 2ig - \sqrt{3}\sin 2k}{4}, \tag{1.216}$$

$$E_{5,6} = \pm\frac{1}{2}\arccos\frac{-\cos 2k - \cos 2ig + \sqrt{3}\sin 2k}{4} \tag{1.217}$$

and demonstrate some numerical examples of the band structure in Fig. 1.19a. The pseudo-Hermiticity condition reads

$$\hat{\hat{P}}\hat{\hat{U}}^\dagger\hat{\hat{P}}^{-1} = \hat{\hat{U}}^{-1}, \tag{1.218}$$

$$\hat{P} = \int dk \, |-k\rangle\langle k| \otimes \begin{pmatrix} 0 & 0 & \hat{\sigma}_x \\ 0 & \hat{\sigma}_x & 0 \\ \hat{\sigma}_x & 0 & 0 \end{pmatrix} \tag{1.219}$$

and we invite the reader to proof the parity-reversal symmetry as well. The band structures given in Fig. 1.19a show that parity-time symmetry breaks due to merging of chiral symmet-

60

ric band pairs or between bands having the same sign. Indeed, according to the numerically calculated phase diagram in Fig. 1.19c, the highest and the lowest (red) bands $E_{1,2}$ are imaginary almost everywhere, except few very narrow regions in the diagram. The intermediate (green) bands $E_{3,4}$ are conservative within a broader region and can only break due to band merging with the upper (red) or with the lower (blue) bands. The sparse yellow distribution beyond the unbroken region is likely due to some numerical noise. Finally, the remaining (blue) bands $E_{5,6}$ are the most protected, since the unbroken region is the largest. All in all, the parity-time symmetry indeed provides real-valued spectrum for all bands, however the smallest unbroken region in the parametric space is very narrow. To support our earlier guess about universality of the threshold, we note that in this walk the upper limit of the narrow stripe regions reaches approximately $g \approx 0.68$ and therefore it is not consistent with the threshold of the previous walks.

1.8.2 $\mathcal{PT}$ symmetry in 2D

Next, we consider the 2D walk of a two-component psedospin and introduce the parity-time symmetric pattern, that we used so far in our experiments [B3]. The pattern is shown in Fig. 1.20a, where the phase modulation increases the size of the elementary unit cell and thus the elementary pseudospin in the stroboscopic picture comprises 8 components, namely

$$
|k\rangle = \begin{pmatrix} lr(k_n, k_p) \\ ll(k_n, k_p) \\ rr(k_n, k_p) \\ rl(k_n, k_p) \\ ur(k_n, k_p) \\ ul(k_n, k_p) \\ dr(k_n, k_p) \\ dl(k_n, k_p) \end{pmatrix} \otimes \sum_{\substack{\text{mod }(n,2)=1 \\ \text{mod }(p,2)=1}} e^{-nk_n - pk_p} |n, p\rangle. \tag{1.220}
$$

Then, the evolution operator can be derived as

$$
\hat{\hat{U}} = \begin{pmatrix} 0 & \hat{\hat{U}}(g) \\ \hat{\hat{U}}(-g) & 0 \end{pmatrix}, \tag{1.221}
$$

$$
\hat{U}(g) = \begin{pmatrix} \hat{\Phi}(\varphi)\hat{G}(g)\hat{S}(k_n, k_p)\hat{C} & -\hat{\Phi}(\varphi)\hat{G}(g)\hat{S}(k_n, -k_p)\hat{C}^\dagger \\ -\hat{\Phi}(-\varphi)\hat{G}(g)\hat{S}(k_n, -k_p)\hat{C}^\dagger & \hat{\Phi}(-\varphi)\hat{G}(g)\hat{S}(k_n, k_p)\hat{C} \end{pmatrix}, \tag{1.222}
$$

$$
\hat{C} \stackrel{\text{def}}{=\!=} e^{i\frac{\pi}{4}\hat{\sigma}_x}, \qquad \hat{S}(k_n, k_p) \stackrel{\text{def}}{=\!=} e^{i(k_n + k_p)\hat{\sigma}_z}, \tag{1.223}
$$

$$
\hat{G}(g) \stackrel{\text{def}}{=\!=} e^{ig\hat{\sigma}_z}, \qquad \hat{\Phi}(\varphi) \stackrel{\text{def}}{=\!=} e^{i\varphi\hat{\sigma}_z}. \tag{1.224}
$$

The block diagonal form of the evolution operator allows one to further reduce the psedospin dimensionality by doubling the temporal period. Therefore, the effective band structure has

only four bands

$$
E_{1,2} = \arccos\Big(\frac{-2\cos\varphi\sin^2\left(k_n+k_p\right)+\cos 2(k_n-k_p)-2\cos 2ig}{4}+
$$
$$
\frac{\sqrt{2}}{8}\cos\left(k_n+k_p\right)\Big[14-6\cos 2\varphi+4\cos\left(2\varphi-2ig\right)+4\cos\left(2\varphi+2ig\right)-2\cos 2(k_n+k_p)+
$$
$$
\cos\left(4\varphi-2(k_n+k_p)\right)+\cos\left(4\varphi+2(k_n+k_p)\right)+4\cos\left(2(\varphi-k_n+k_p)\right)
$$
$$
+4\cos\left(2(gi-k_n+k_p)\right)+4\cos\left(2(gi+k_n-k_p)\right)+4\cos\left(2(\varphi+k_n-k_p)\right)\Big]^{\frac{1}{2}}\Big),
$$
$$
E_{3,4} = \arccos\Big(\frac{-2\cos\varphi\sin^2\left(k_n+k_p\right)+\cos 2(k_n-k_p)-2\cos 2ig}{4}+
$$
$$
\frac{\sqrt{2}}{8}\cos\left(k_n+k_p\right)\Big[14-6\cos 2\varphi+4\cos\left(2\varphi-2ig\right)+4\cos\left(2\varphi+2ig\right)-2\cos 2(k_n+k_p)+
$$
$$
\cos\left(4\varphi-2(k_n+k_p)\right)+\cos\left(4\varphi+2(k_n+k_p)\right)+4\cos\left(2(\varphi-k_n+k_p)\right)
$$
$$
+4\cos\left(2(gi-k_n+k_p)\right)+4\cos\left(2(gi+k_n-k_p)\right)+4\cos\left(2(\varphi+k_n-k_p)\right)\Big]^{\frac{1}{2}}\Big). \tag{1.225}
$$

By illustrating the upper two bands in Fig. 1.20c, we show that both symmetric pairs of bands can be broken (plot (b)) and recovered (plot (d)) simultaneously, or only the highest (and the lowest symmetric) band can be broken (plot (c)). This evidence is summarized in the phase diagram 1.20b. Finally, the parity-time reversal operator can be found as

$$
\hat{\hat{P}T} = \begin{pmatrix} \hat{P}T & 0 \\ 0 & \hat{P}T \end{pmatrix}, \tag{1.226}
$$

$$
\hat{P}T = \hat{P}_{n-p}\hat{T}_{+,1} = \iint dk_n dk_p\, |k_p,k_n\rangle\langle k_n,k_p| \otimes \begin{pmatrix} ie^{-i\frac{\pi}{4}\hat{\sigma}_x} & 0 \\ 0 & ie^{-i\frac{\pi}{4}\hat{\sigma}_x} \end{pmatrix} K \tag{1.227}
$$

and the pseudo-Hermiticity condition holds with $\hat{\hat{\eta}} = \hat{\hat{P}}$ as well. To conclude the section, we also anticipate a $\mathcal{PT}$ symmetry protected quasiconservative evolution of the 2D achiral walk, however since we further concentrate exclusively on the time-multiplexed walks, showing this would be beyond the scope of the thesis.
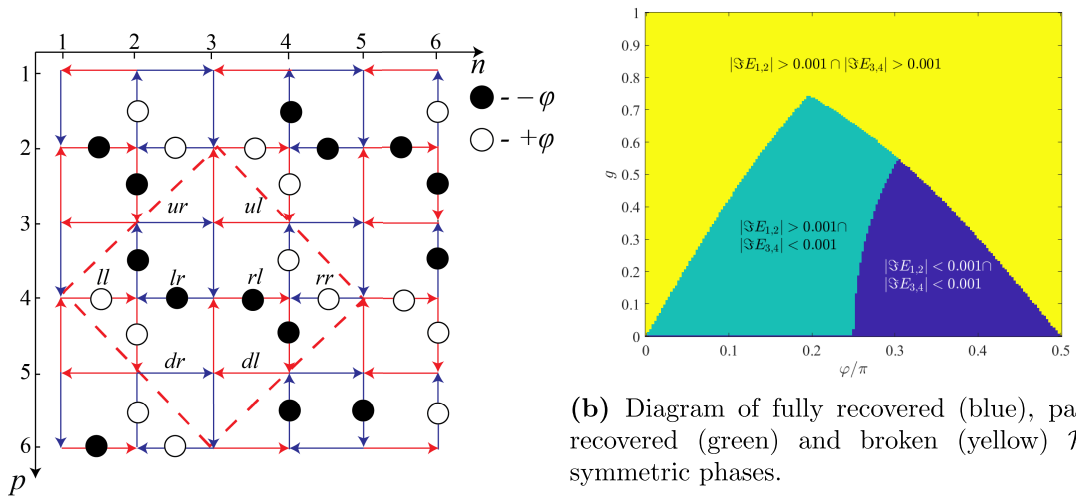
(a) 2D two-component pseudospin walk with $\mathcal{PT}$-symmetric potential. The red dashed square denotes elementary unit cell of the lattice.

(b) Diagram of fully recovered (blue), partly recovered (green) and broken (yellow) $\mathcal{PT}$-symmetric phases.
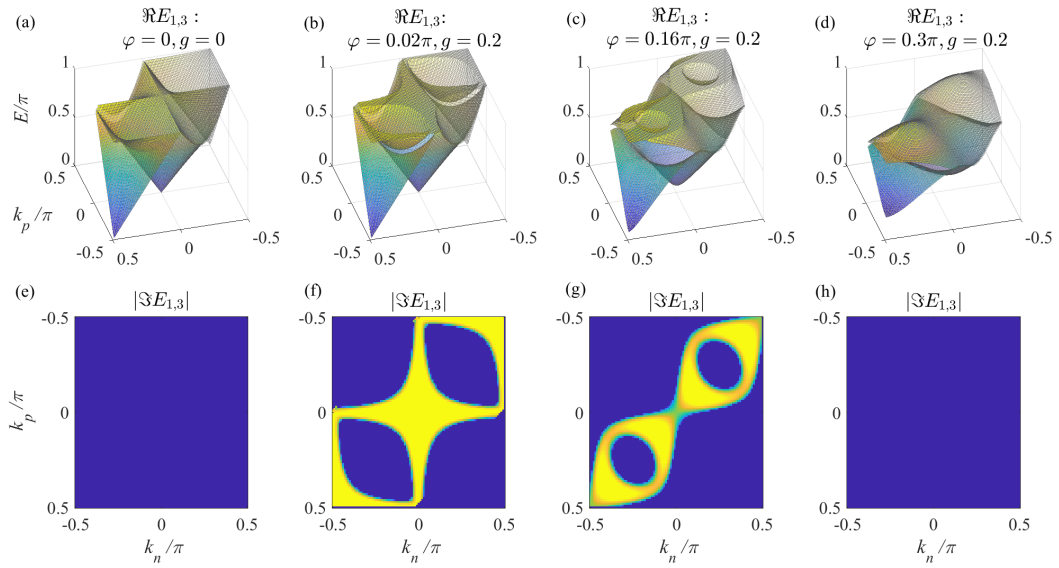
(c) Real (upper row) and imaginary (lower row) parts of the positive band for the 2D walk in the conservative (a,e), recovered (d,h) and broken (b,f,c,g) $\mathcal{PT}$-symmetric phases. Yellow regions in (f,g) designate non-zero imaginary parts of the eigenenergies.

Figure 1.20

63

Chapter 2

Time-multiplexed fiber loop set-ups

This chapter is devoted to the experimental set-ups based on time-multiplexed coupled fiber loops, realizing the 1D and 2D walks of a two-component pseudospin. The idea of time-multiplexed walk has been firstly proposed [46] and quantum optical version of such a walk has been realized in 1D [33, 95] and 2D [96] by A.Schreiber and the group of C.Silberhorn. In turn, the time-multiplexed 1D walk of a coherent light pulse with many photons has been implemented using telecommunication fiber optical components in our group by A.Regensburger [29] and further improved by M.Wimmer. Later on, the set-up was proven to be robust and coherent even in the nonlinear and non-conservative regimes, in order to demonstrate such fundamental phenomena as parity-time ($\mathcal{PT}$) symmetry [85, 97], $\mathcal{PT}$-symmetric defect modes [98] and solitons [99], $\mathcal{PT}$-symmetric Bloch oscillations [84], Zitterbewegung, Bloch Oscillations and Landau-Zener Tunneling [100], Berry curvature [51] and time-reversed light propagation [101]. Besides, Anderson localization has been demonstrated by A.Pankov in the group of D.Churkin [102] in an optical set-up with a similar architecture. Afterwards, the set-up has been successfully extended in our group by Andre Muniz to the 2D two-component pseudospin walk and $\mathcal{PT}$-symmetric solitons [B3] as well as 2D nonlinear collapse [B4] have been observed up to now. Exhaustive technical details on the one-dimensional set-up have been provided in the Supplementary materials of [51, 84, 99, 101] as well as in the doctoral [10] and master [11] theses of M.Wimmer. Therefore, here we give only a brief description of the set-up, including incorporated optical components, their purposes and functionalities. The two-dimensional set-up, introduced in Supplementary Materials of [B4] and [B3], is a straightforward extension of the one-dimensional system with two additional fiber loops. Despite its higher complexity and stricter demands for acoustic isolation and polarization control, the technique and optical components remain conceptually the same as for the 1D case. Therefore, we also give only a brief description for the extended set-up.

2.1 1D pseudospin walk

A train of rectangular pulses of a width 25 or 50 ns (depending on the fiber loop lengths in each individual experiment) with carrier wavelength 1555 nm is prepared with a DFB laser diode and an alternating sequence of EDFA amplifiers and amplitude modulators (see [10] for details). The peak power of the pulses can be varied between 10 and 110 mW, depending on whether linear regime of the walk or nonlinear self-phase modulation of the pulses in the loops is required for the experiment. Afterwards, the train of pulses is injected into one of the loops via a 50/50 coupler, equally splits between the loops via another coupler (VC)

and passes through the EDFA amplifiers. Before making the round-trips, the trains are stopped by the Mach-Zehnder modulators (MZM) in the loops for around 10 ms ("warm-up" phase). During this timespan, the EDFAs manage to adopt its gain to the average power of the pulse train and eventually to the measurement phase, provided the separation between pulses in the train approximately matches the average round trip time in the loops. Otherwise, if no "warm-up" phase is present and the measurement starts directly, due to a large temporal signal variation of the walk and a milisecond time constant of EDFAs, one can experience gain fluctuations and as a result unwanted power oscillations in the loops (see [10] for details). In order to terminate the "warm-up" phase, the pulse generation is blocked and the MZMs in both loops open up and transmit the last pulse in the train, thus letting it further circulate through the loops, split and realize a free walk propagation in time. The purpose of the EDFAs is to compensate for all power losses appearing during the pulse propagation, including decoupling, insertion losses of components, Brillouin scattering, etc. The pilot CW-signals at the wavelength of 1536 nm and with the power, much higher than the average power of the pulses, get coupled via wavelength-division multiplexers (WDMs) and further stabilize the gain of the EDFAs and suppress any transient noise. In addition, by tuning the power of the pilot lasers, one can adjust the effective gain at 1555 nm in order to precisely compensate for the losses. Thereafter, the pilot signals as well as the noise from amplified spontaneous emission of the EDFAs are filtered out by tunable bandpass filters (BPF) in order to ensure a sufficiently low noise background level for the pulses. Next, 4 km spools of dispersion-compensating fiber are inserted in each loop, thus inducing the nonlinear effect of pulse self-phase modulation with the nonlinear factor $\gamma \approx 7$ (W· km)$^{-1}$ [10], so that a nonlinear phase shift of π is acquired at 110 mW peak power of the pulses. Thus, at much lower peak powers of about 10 mW the light propagation is essentially linear. Next, one of the loops (the blue one in Fig. 2.1) incorporates an additional 40 m spool of a single-mode fiber (SMF), introducing a time delay of about 200 ns between pulses propagating to the short and to the long loop and thus mimicking the position step of the original 1D spatial lattice, according to sec. 1.3. Taking into account the average round-trip of about 20 ms and the delay time of 200 ns, the number of accessible time steps (before neighboring time steps start to overlap) in a free walk is 20000/200=100. Although this propagation time is not a principal limit for the set-up ($>$ 1000 time steps), it was sufficient for my particular experiment on topological edge states, to be discussed later. After the fiber spools, 10% of the signal is decoupled via a 90/10 beam splitter in order to monitor the walk distribution every round trip via photodiode detectors. Since most of the components and the fibers are not polarization-maintaining, we had to ensure a stable polarization state of the pulses in order to make them interfere at the central beam splitter (VC). For that, a series of manually adjustable polarization controllers (two small circles) and polarizing beam splitters (PBS) are used for suppressing the orthogonal part of the unwanted polarization rotation, monitored with the respective photodiode detectors. Polarization rotations mainly due to temperature drifts are normally negligible within 15-20 min, so that a number of measurements can be acquired within this time window without extra alignment of the polarization state. On the other hand, acoustic noise is less harmful for the interference quality, because the noise below 100 kHz has no influence on individual measurements taken within approximately 20 ms×100 round trips=2000 ms, while higher frequencies can be suppressed by isolating fiber spools with foam material and a stable optical table. Further, amplitude and phase of individual pulses can be arbitrarily modulated via the incorporated voltage-driven MZMs and phase modulators (PM) connected to mutually synchronized arbitrary waveform generators. So, for example, non-conservative parity-time symmetric walk can be imposed in the system by
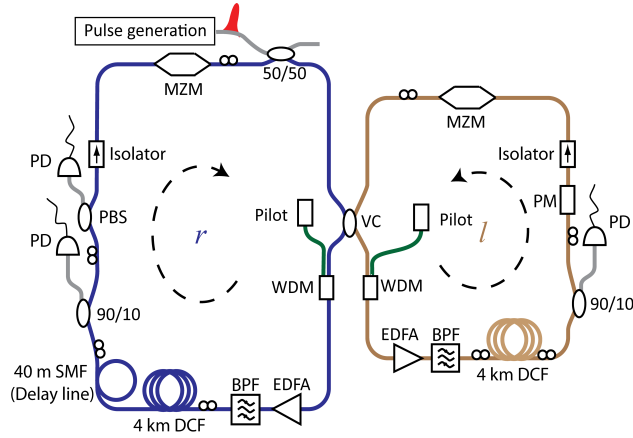
Figure 2.1: Principle scheme of the one-dimensional time-multiplexing set-up.
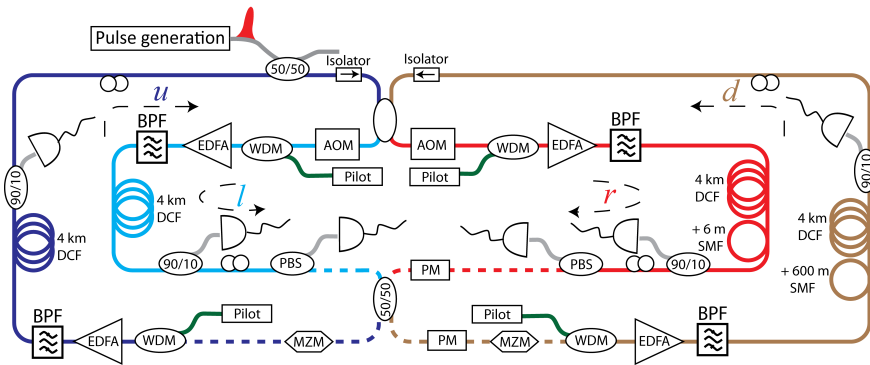

Figure 2.2: Principle scheme of the two-dimensional time-multiplexing set-up.

setting a periodic gain/loss modulation with the MZMs around 50% transmission (the 3 dB netto loss are compensated by the EDFAs). Finally, the central voltage-driven beam splitter (VC), which couples the fiber loops, can be also varied between approximately 0/100 and 0/100 splitting ratios, with the maximum modulation rate of about 100 kHz and typical rise-fall time 200-400 ns. In my experiment, it was a core element for creating the topologically non-trivial edge state in the lattice.

2.2   2D two-component pseudospin walk

The two-dimensional time-multiplexed set-up comprises four coupled fiber loops, in accordance with the section 1.3. Due to higher dimensionality of the lattice, the lengths of the SMF fiber spools in each loop had been extended up to approximately 30 km, in addition to the 4 km DCF spools (see Fig. 2.2). The length difference between the outer two loops is about 600 m, so that the maximum number of available positions n is approximately 113 (the round trip distance divided by the outer loop length difference). The delay length between inner two loops is 6 m, yielding maximally 100 available positions p for the free walk. 30 km long SMF fiber lengths lead to an additional self-phase modulation effect with $\gamma \approx 1.1$ (W· km)$^{-1}$, so that a pulse having the peak power of around 51 mW acquires the nonlinear phase shift of π while propagating over one of the loops. The longer propagation distances and higher number of components in the set-up demand a better polarization control and
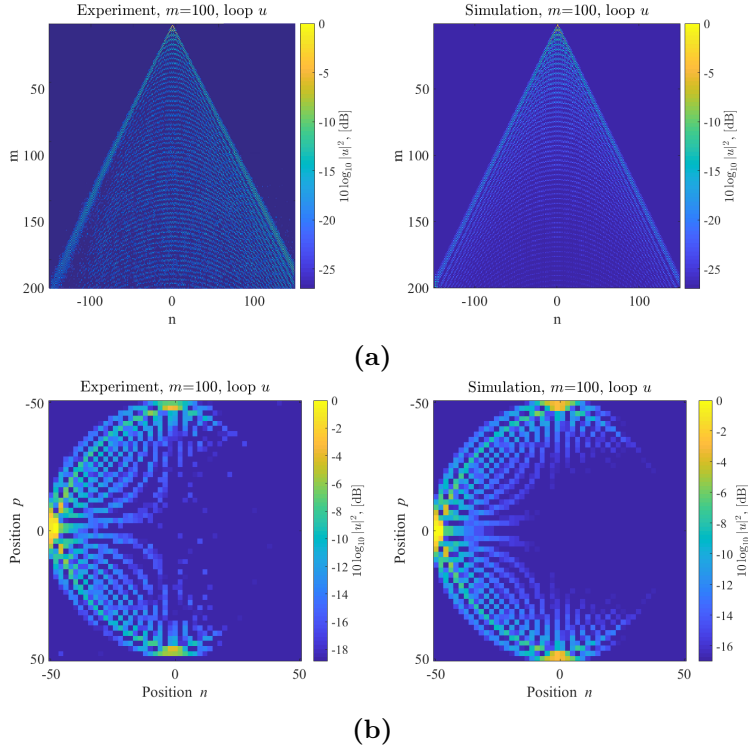
Figure 2.3: Visual comparison of free walks in 1D (a) and 2D (b) set-ups for the same light propagation distance of about 6000 km. The fiber spools' length of 30 km is redundant for the 1D set-up, given the number of round-trips is only 200.

noise isolation compared to its one-dimensional counterpart. Therefore, some of the used components are polarization-maintaining (dashed lines in the scheme) and the fiber spools are additionally isolated also in the frequency range below 100 Hz.

Despite the increased complexity of the two-dimensional set-up, its performance nevertheless is comparable to that of the one-dimensional version, given the overall light propagation distance is the same. Indeed, using the 30 km fiber spools in both set-ups, we can qualitatively estimate both 1D and 2D walks evolving for the same distance of 6000 km (see Figs. 2.3a and 2.3b). We clearly see the most of the interference fridges in the last round trip of the 2D walk and therefore the coherence quality should be at least not lower, than for the last step of the 1D walk.

Chapter 3

Nonlinearity in 1D and 2D Discrete Light Walks

In the chapter "Theoretical background", we provided a broad overview of the beam splitter based discrete quantum walks, including their dynamics and underlying symmetries. It appears evident that in such linear systems the symmetries and topology play a primary role in comparison to the dynamics as they completely predetermine the dynamical behaviour of the walker. In other words, by studying the symmetries of the system one can identify all basic features of the elementary bulk solutions and by learning about topology of infinite bulks one can even predict the existence and robustness of localized defect solutions. The situation changes drastically, when nonlinearity comes into play. The dynamical behaviour does not only depend on the "external" parameters of the Hamiltonian, but also on the state itself. More specifically, nonlinear systems are characterized by the regime called determenistic chaos, in which the dynamics becomes highly sensitive to initial conditions and any long-term predictions of the state become impossible. This behaviour may occur even in such seemingly simple system as pendulum, when the amplitude of oscillations becomes too high. In the context of complex far-from-equilibrium systems, the chaotic regime may turn under some circumstances into a more ordered self-organized regime. Classical examples of self-organisation, originally known from non-equilibrium thermodynamics are Rayleigh-Benard convection and Belousov-Zhabotinsky reaction [103].In systems described by the nonlinear Schroedinger, Korteweg-de Vries or sine-Gordon equation, the presence of nonlinearity may introduce a self-localized spatial defect - soliton. The system may experience not only the parametric topological transitions and spontaneous symmetry breaking (e.g. the parity-time symmetry breaking), but also the first and second order thermodynamic as well as topological Berezinskii-Kosterlitz-Thouless phase transitions without symmetry breaking. From microscopic quantum mechanical point of view, phenomenological nonlinear models correspond to many particle fermionic or bosonic interactions. This is the case, for example, for the Gross-Pitaevsky nonlinear model, describing a diluted gas of interacting bosons in the mean-field approximation. In this model, even weak, effectively short-range, interactions eventually lead to a collective condensation of bosons in the ground state, the so-called Bose-Einstein condensate. This phenomenon has been demonstrated quantum mechanically [104–106] as well as classically [107] for photons. Another famous examples in condensed matter physics are the phenomenological Ginzburg-Landau and Ising models, which describe the macroscopic phenomena of superconductivity and ferromagnetism, respectively. Finally, we mention Hubbard Hamiltonian with on-site interactions known from solid state physics, which is based on tight-binding approximation and which can explain metal-insulator transition in crystals. In optics, a direct interaction of individual photons with each other is

not possible since they possess neither charges nor masses. Therefore nonlinear processes in optics typically deal with light-matter interactions, which allow for a large number of photons to collectively alter the optical response function of a medium and thus introduce a medium-mediated self-action to the bunch of photons (modulation instability, self-focusing, self-phase modulation, frequency-mixing). Photon-photon interactions on the level of individual photons and sub-picowatt powers is a long-standing goal of the modern optics, which is so far achieved only via special techniques of cavity quantum electrodynamics [108–110]. In summary, the importance and diversity of nonlinear dynamics for classical as well as for quantum many-body systems is hard to overestimate. In this context, it is appropriate to quote the famous phrase by Stanislav Ulam: "Using a term like nonlinear science is like referring to the bulk of zoology as the study of non-elephant animals." In what follows, we devote this chapter to nonlinear effects in the 1D and 2D time-multiplexed Discrete Quantum Walks, namely we study localized formations on the lattice, such as conservative and non-Hermitian solitons as well as nonlinear topological edge states. In our experiments, the nonlinearity is realized as Kerr-type self-phase modulation via dispersion-compensating fibers placed in each loop, provided that available peak powers of the circulating pulses are in the range of 100 milliwatt. The corresponding nonlinear phases acquired by individual pulses can be expressed in the discrete model by the local intensity-dependent operator

$$\hat{K}(|l_n^m|^2, |r_n^m|^2) = \begin{pmatrix} \exp(\gamma|l_n^m|^2) & 0 \\ 0 & \exp(\gamma|r_n^m|^2) \end{pmatrix}, \tag{3.1}$$

where γ is the nonlinear Kerr coefficient and $(l_n^m, r_n^m)^{\mathrm{T}}$ is a pseudospin at a time step m localized in the position n.

3.1 Non-Hermitian solitons in $\mathcal{PT}$-symmetric environments

Soliton or solitary wave, an ubiquitous hallmark of nonlinear systems, is a long-living localized self-reinforcing wave state, which occurs due to a balanced action of a nonlinearity-induced focusing and a dispersive (or diffractive) spreading. Most remarkably, such formations can be very stable and robust against external perturbations, and some of them [111] (vertices, kinks, monopoles etc.) even inherit topologically non-trivial structures and thus they can be identified as topologically protected phase defects. Moreover, in many aspects solitons interact as particles. For example, in integrable conservative systems, moving solitons collide elastically with each other, without changing their shapes and velocities. In contrast, highly dissipative systems possess a special class of so-called dissipative solitons or autosolitons [112, 113], which can exhibit scattering, annihilation and creation. The canonical one-dimensional stationary solution, the so-called fundamental soliton $\psi(x,t) = A \operatorname{sech}(At) \exp(iA^2x/2)$, can be obtained from the integrable conservative nonlinear Schrödinger equation, which in optics is traditionally associated with slowly varying (paraxial) approximations of pulses (beams) propagating in fibers (planar waveguides) [114]. Note, that the spatial width of the soliton is the inverse of the amplitude A and the amplitude can be chosen arbitrarily. Thus, the fundamental solitons form a continuous single parametric family of solutions. Again, in contrast to the conservative families, the conventional dissipative solitons (e.g. in the complex cubic-quintic Ginzburg-Landau model) in order to propagate stably have to additionally keep a certain energy balance with the environment

and therefore to sacrifice that one parametric degree of freedom [113]. Surprisingly, in the presence of a parity-time symmetric complex potential with balanced regions of gain and loss, the continuous parametric family of solitons is nevertheless possible, and they can even be stable and quasiconservative in integrable systems based on the nonlinear Schroedinger equation with a focusing [115–117] or defocusing [118–120] nonlinearity. Moreover, even if parity-time symmetry is broken in the linear regime, a certain level of nonlinearity in integrable systems is capable of restoring the parity-time symmetry and hence the real-valued spectrum [121, 122]. In fact, a continuous family of fundamental solitons has been found and experimentally demonstrated in the 1D time-multiplexed Light Walk, as well [99]. Although the non-Hermitian family was found intrinsically unstable owing to non-integrability of the discrete model, the solitons can nevertheless live for considerably long propagation times in the system, provided the gain/loss parameter is not too high. The endpoint of solitons is marked by their very rapid power "blow-up". As we will see further, the considerable lifetimes imply that solitons are still capable of preserving a certain (although not ideal) energy balance with the non-Hermitian environment. Moreover, we will find out that parity-time symmetric real potential, although strictly speaking recovering $\mathcal{PT}$ symmetry only in the linear regime, can noticeably increase the lifetimes of solitons. Then, specifically for 2D solitons, we will investigate the peculiar phenomenon of quasi-collapse and its non-trivial connection to the "blow-up" event. Further presented theoretical results for the 1D and 2D time-multiplexed walks will be mostly supported by numerical data, while key evolution scenarios for 2D conservative and non-conservative solitons, such as the quasi-collapse and blow-up, will be referenced with experimental data from [B4] and [B3].

3.1.1 1D conservative solitons

We begin our study with the conservative nonlinear parity-time symmetric lattice (see eq. (1.196)) by setting the gain/loss parameter g to 0 and by incorporating the nonlinear operator (3.1) in every time step before the coin operators. Note, that positioning the Kerr operator alternatively after the shift or the position operator will lead to different evolution operators because of non-commutavity of the permutations. Therefore,in general nonlinear solutions would have to be adopted to each of the cases. In the 1D Quantum Walk, soliton families always bifurcate in the linear limit from one of the linear bands of extended Bloch waves and as soliton's amplitude is growing, its eigenfrequency separates farther away from the band of origin. Since for the soliton to exist, the linear dispersive spreading inherent to the band of origin has to compensate for the nonlinear focusing, the choice of the band depends exclusively on the sign of γ. So, in our notations solitons bifurcate from the negative lower band (anti-symmetric eigenmode $(-1, 1)^{\mathrm{T}}$ at $k = 0$, see eq. (1.33)) if $\gamma > 0$ and from the upper band (symmetric eigenmode $(1, 1)^{\mathrm{T}}$ at $k = 0$) otherwise. Note, that in the experiment [99] the γ is always positive for the dispersion compensating fibers in the telecom wavelength range and thus the anti-symmetric soliton family is investigated, while in this work we will study numerically both 1D solitonic families, for completeness.

In order to find the solitonic solutions, we apply the ansatz

$$|E_{\mathrm{s}}\rangle^m = e^{iE_{\mathrm{s}}m} \sum_n \binom{l_n}{r_n} |n\rangle , \tag{3.2}$$

where E_{s} is the propagation constant or eigenenergy of the soliton. Since the soliton's family is spectrally branching from one of the bands, as a starting point of the numerical

algorithm, we choose the linear anti-symmetric $(1, -1)^{\mathrm{T}}$ (symmetric $(1, 1)^{\mathrm{T}}$) mode of the negative (positive band), which is modulated with a Gaussian profile $A \exp(-n^2/(2\sigma^2))$ since the numerical size of the lattice is confined to 100 positions. The boundary conditions are periodic. By slightly increasing the propagation constant E_{s} from the highest -0.25π (the lowest 0.25π) eigenenergy of the negative (positive) band towards the gap, we minimize the norm

$$|| \hat{U} |E_{\mathrm{s}}\rangle - e^{iE_{\mathrm{s}}} |E_{\mathrm{s}}\rangle || \longrightarrow 0. \tag{3.3}$$

The nonlinear coefficient γ is fixed to 1 (-1), while the amplitude A as well as individual pseudospins in each position can be varied arbitrarily by the iterative solver, based on the standard in-built MatLab algorithm 'trust-region-dogleg'. After the first "close-to-band" solution with the smallest power is found, it is then chosen as a starting point for finding the next solution, having a slightly larger (smaller) propagation constant. Thus, the entire family of solutions can be traced out up to the opposite linear band. The same numerical method has been used in [99] for the anti-symmetric soliton. It is worth mentioning that the genuine stationary solution has to reside at both even and odd positions at once, because otherwise it would necessarily oscillate in time due to the exchange of sublattices. Therefore the optimization task has to be formulated in the instantaneous picture, including both sublattices. Consequently, if the lattice is additionally modulated with the parity-time symmetric potential depicted in Fig. 1.17b, the spatial period gets extended to 4 positions and thus the elementary pseudospin should comprise 8 components.

The resulted total powers P, full widths at half maximum (FWHM), lifetimes and typical amplitude profiles of the symmetric and anti-symmetric soliton are presented in Fig. 3.2 and Fig. 3.1, respectively. One can see that in both cases, the further away the propagation constant from the band of origin, the higher is its total power and the narrower is the FWHM, which is defined via the standard gaussian fitting. Interestingly, close to the turning point of the total power curve ($P \approx 2.5$), the solitonic family bifurcates again: one branch of solutions (red circles in the plots) continues to grow linearly, while another one (black circles) is slightly bending down. This family bifurcation and further discussed stability conditions are typical for bright gap solitons in 1D periodic photonic crystals with Kerr-type nonlinear response [123–125]. The nominal lifetime, defined as a number of evolution time steps until the relative deviation between subsequent soliton field distributions exceeds 0.01% and plotted in the insets of Figs. 3.2 and 3.1, helps us to estimate stability of the solutions. One can see, that the high power branch gets unstable right after the pitchfork bifurcation, while the low power branch is stable approximately up to the middle of the band gap $E = 0$. The instability of the high energetic family right is due to nonlinearity-induced breaking of a certain symmetry of the discrete lattice [125]. We attribute this to chiral symmetry breaking, because the soliton family branches only from one linear band and therefore the chiral symmetry condition does not hold. Indeed, spatial amplitude profile of the high energetic soliton family remains mirror symmetric (at least for small propagation constants) with respect to exchange of the sublattices, i.e. the shape should preserve chiral symmetry for small enough soliton's power, but eventually this solution gets destabilized if its total power exceeds the bifurcation point. On the other hand, the stable low energetic branch gets "adopted" to the symmetry breaking condition by allowing one pseudospin component to dominate in one sublatice, while letting another component to equivalently prevail on the second sublattice. All in all, although this is only a heuristic way to identify the symmetry that gets broken, one can certainly state that the instability of the high energetic family
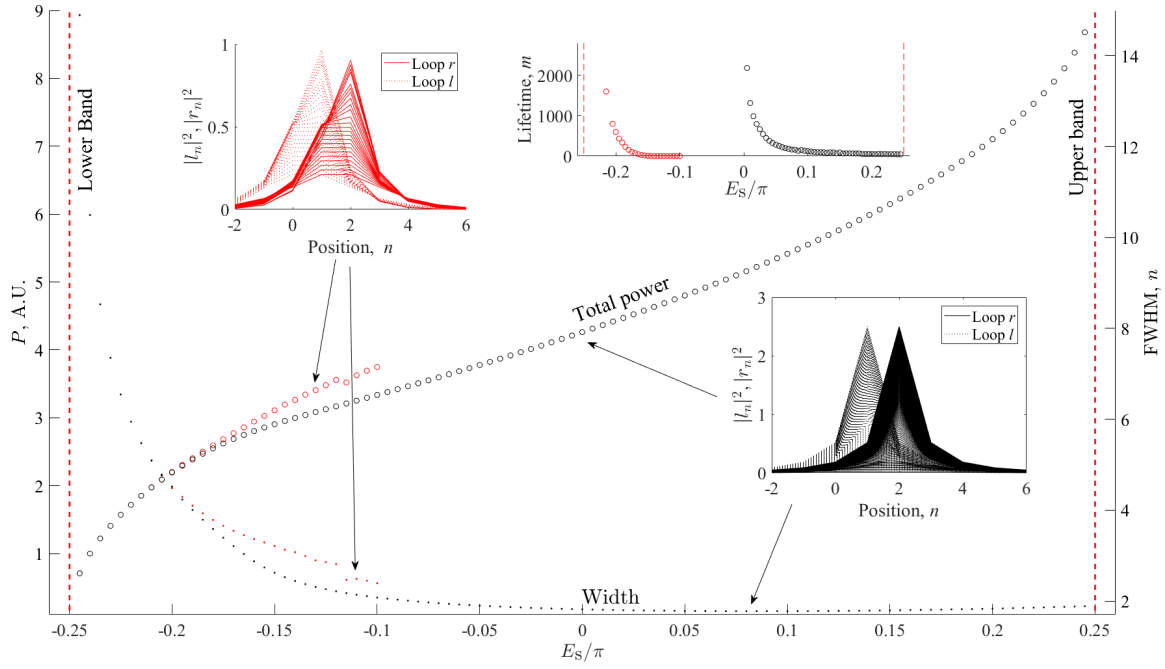
Figure 3.1: Conservative anti-symmetric soliton at $\varphi = 0$. Black (red) dots and circles correspond to the stable (unstable) family branch.

branch is triggered by some nonlinearity-induced spontaneous symmetry breaking, typical for periodic photonic lattices with Kerr-type nonlinearity [125].

Finally concluding on the conservative solitons in the unmodulated free lattice, the numerically obtained parametric curves suggest that symmetric and anti-symmetric soliton families are mirroring counterparts of each other with respect to the zero energy, despite the fact that they have slightly different stability conditions, namely the estimated destabilization threshold of the former one is positioned slightly above the middle of the gap (see the inset of Fig. 3.2), while the anti-symmetric soliton has it exactly at zero in accordance with previous numerical data provided in [99]. We attribute this discrepancy to certain symmetry features of the numerical noise, which must perturb the two distinct soliton families differently. To find it out, one requires a more thorough analysis of the stability problem, which is however beyond the scope of this thesis.

Next, we concentrate on the conservative lattice with the non-zero parity-time symmetric real potential $\sim \varphi$, as shown in Fig. 1.17b. By taking the fundamental solitonic solution at $\varphi = 0$ separated by $\delta E_\mathrm{s} = 0.01\pi$ from the band of origin, we trace out the soliton by slowly increasing or decreasing the potential height φ and keeping the separation δE_s fixed. The outcome of the numerical calculations are presented in Fig. 3.3 and Fig. 3.4 for the anti-symmetric and symmetric soliton, respectively. It follows that the widths and the total powers of both fundamental solitonic families again coincide (black curves). At the same time, certain values of the potential heights make both solitons unstable even if the total power is considerably low. Interestingly, if we break translation symmetry of the lattice even non-locally (i.e. far away from the soliton's localization) by setting its numerical size to 101 instead of 100, the nonlinear mode solver also finds double-hump solitons in both cases (magenta curves), which are however unstable almost for all values of φ. In contrast to the fundamental solutions, the dipole solutions appear only if $\varphi > 0$ in the anti-symmetric and if $\varphi < 0$ in the symmetric case, respectively. Also, they have different separation distances
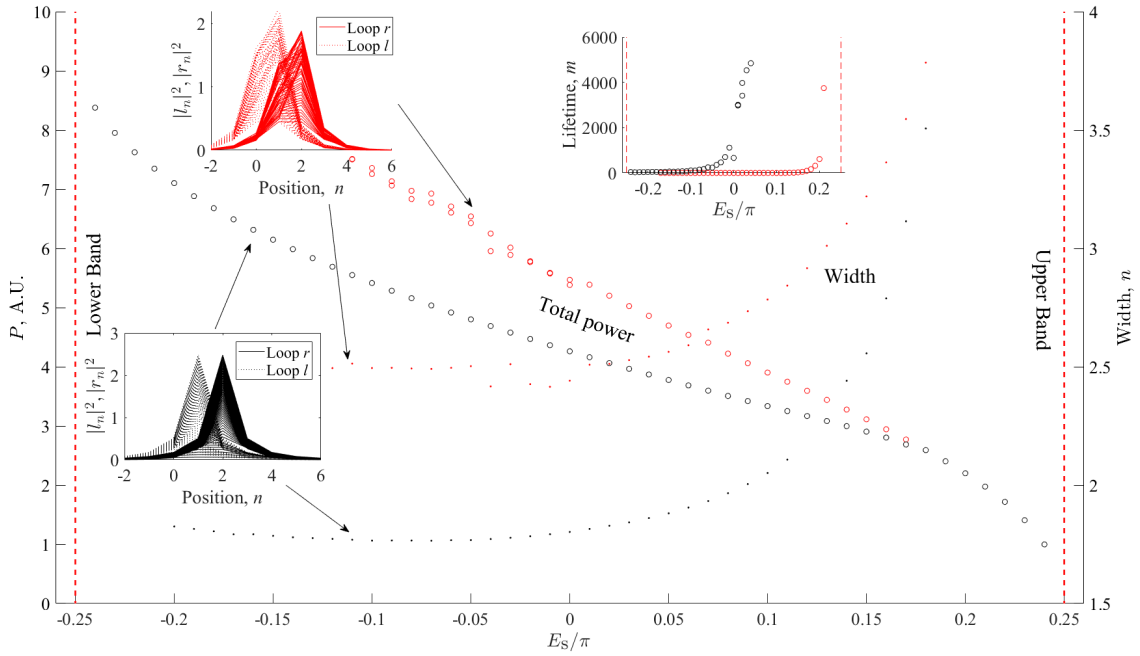
Figure 3.2: Conservative symmetric soliton at $\varphi = 0$. Black (red) dots and circles correspond to the stable (unstable) family branch.

between the peaks, namely the highest amplitude peaks are situated externally in one and internally in another case, as seen from the inset figures. The antisymmetric double-hump soliton has been observed experimentally in the time-multiplexed set-up at $\varphi = 0.4\pi$ [99]. We can also see that it is stable only in the small range $\varphi \in (0.38\pi, 0.42\pi)$ (filled circles). On the other hand, the symmetric double-hump soliton is stable only for φ close to zero. Finally, note that total power of the fundamental solitons (blue curves) is lifted and they generally become less stable in case of the broken translition symmetry. This power discrepancy has to however go down for a larger size of the lattice. In summary, the presence of the parity-time symmetric real potential: 1) reduces the total power of the fundamental solitons provided $|\varphi|$ is not too close to π; 2) it does not break a mirroring symmetry between the fundamental solitons, but it does so for the dipole solutions, which for a certain sign of φ become more favorable than the fundamental solutions if the discrete translation symmetry of the lattice is non-locally broken.

3.1.2 1D non-Hermitian solitons

It has been already mentioned that stable solitonic solutions exist in integrable systems with pseudo-Hermitian parity-time symmetric potentials, based on the nonlinear Schroedinger equation. Also, we have already shown that dynamics of a fixed band in the linear lattice can be well approximated by the Schroedinger equation close to the center of the Brillouine zone. In that regard, despite the discreteness of the quantum walk and spatial localization of solitons, it is useful to recall basic results of previous investigations. The most studied continuous system in this context describes pulse (beam) propagation along two coupled fibers (planar waveguides), one having a lossy and another one amplifying region [116, 122, 126–129]. In this example (see [128] for more details), two exact (symmetric and anti-symmetric) bright solitonic solutions exist simultaneously for the same (self-focusing) sign of the cubic
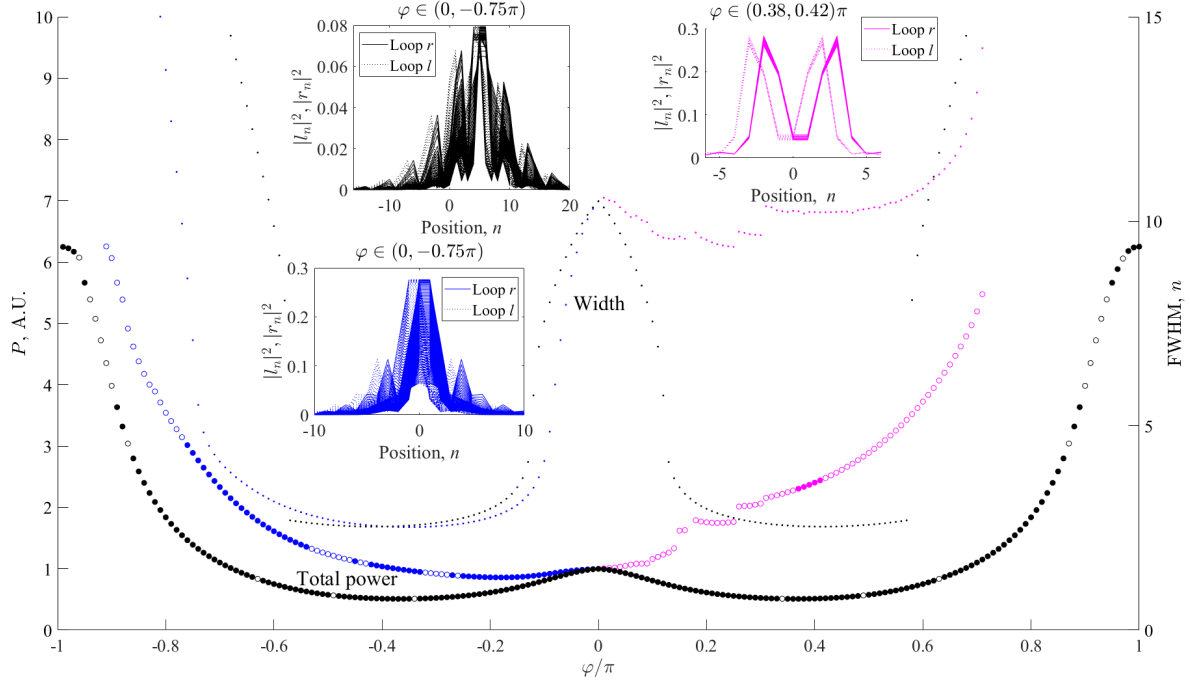
Figure 3.3: Conservative anti-symmetric fundamental (black and blue) and dipole (violet) solutions with varying φ and $E_s = E_{\text{band}} + 0.01\pi$. The fundamental (black colored) family is traced out in the lattice (100 positions) with periodic boundaries. The fundamental (blue) and dipole (violet) solutions are traced out in the lattice (101 positions) with broken translation symmetry.
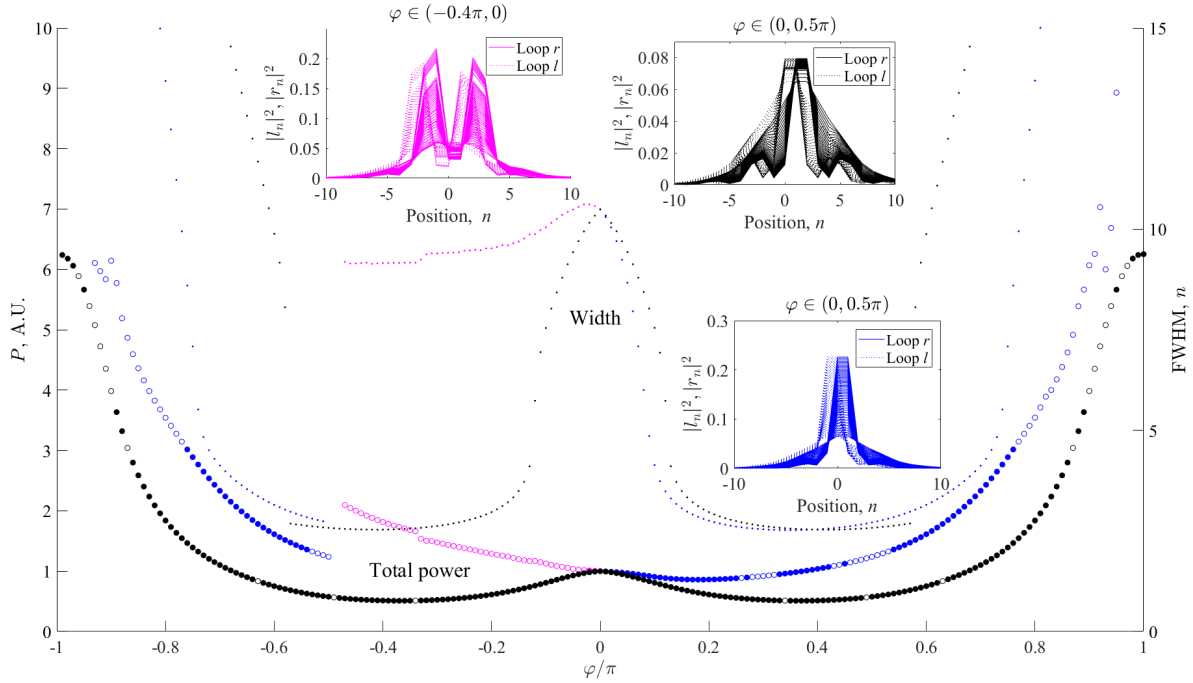

Figure 3.4: Conservative symmetric fundamental (black and blue) and dipole (violet) solutions with varying φ and $E_s = E_{\text{band}} - 0.01\pi$. Lattice parameters are the same as for the anti-symmetric solutions.

nonlinearity. In contrast to our case of chiral symmetric pair of families, these solitons coalesce into one single critically unstable solution at the exceptional point, when the gain/loss and the coupling parameter become equal. In our case, such a coalescence would correspond to a merging of the intermediate two bands at a Dirac point in the middle of the Brillouine zone, when the real and/or complex parts of the $\mathcal{PT}$-symmetric potential are appropriately tuned. Note, that according to [130], generic parity-time symmetric potentials in the nonlinear fully continuous Schrödinger equation do not allow a continuous parametric family of solitons to exist if they brake the parity-time symmetry. Nevertheless, for one special class of $\mathcal{PT}$-symmetric potentials, breaking of the parity-time symmetry by solitonic (non-$\mathcal{PT}$-symmetric) families is possible [131],[132] in such systems. That prohibition however is not applicable to the system of coupled waveguides, since the $\mathcal{PT}$ symmetry is imposed in the discrete pseudospin space and not in the continuous one. The same argument holds for our fully discrete system with pseudospin. If the gain/loss parameter is not too high in the dual-core waveguide system, the symmetric soliton is stable provided its peak power P_0 does not exceed the analytically defined threshold $\frac{4}{3}\sqrt{1-g^2}$. If the threshold is exceeded, the instability leads to an unbounded exponential growth of the amplitude (blow-up) and to a chaotic field dynamics or to a long-living oscillating solution called breather. On the other hand, the anti-symmetric solution is always unstable and 1) if its peak power is below another, numerically determined, threshold $\sim 1.71\sqrt{1-g^2}$, the soliton can persist in the system for an exponentially long lifetime $\tau \sim \exp\left(\alpha\sqrt{1-g^2}/P_0\right)/P_0$ until it completely disperses or forms an oscillating breather 2) above the power threshold, the asymmetric soliton dissociates into two oscillating mobile breathers or into two mobile pulses, one decaying and another one growing exponentially in time (blow-up). Another insightful result of [128] is that the stationary solitons in this pseudo-Hermitian integrable system remain conservative (the total power is constant) as soon as the amount of power in one pseudospin component is equal to that in the other component. This condition is obviously less demanding than the condition of $\mathcal{PT}$ symmetry, imposed on solitons in the fully continuous Schrödinger model [130].

It turns out that the chiral symmetric and anti-symmetric non-Hermitian families in our discrete quantum walk system, although having some common features with symmetric and anti-symmetric solutions in that continuous dual-core waveguide system, still have very different stability properties. Below we provide the most important facts about the non-Hermitian 1D solitons and list them hierarchically, so that every next thesis is supported or based on the previous ones.

1. The non-Hermitian families of chiral stationary fundamental symmetric and anti-symmetric solitons coincide with their conservative counterparts in the limit of $g \to 0$. The presence of gain/loss accordingly modifies the total power and the shape of the solitons in order to preserve a certain energy balance with the non-Hermitian environment.

2. The non-Hermitian families could be traced along the low energetic branch (black curves in Figs. 3.3 and 3.4) also beyond the pitchfork bifurcation point. The non-Hermitian modification of solitons preserves an almost equal amount of power in l and r pseudospin components if $\varphi = 0$, while it makes that power balance between the components asymmetric (see Figure 3.5a) if $\varphi = \pm 0.37\pi$. Recalling that the 1D parity-time symmetric operator (1.203) does not exchange l and r components of the pseudospin, we can expect that direct violation of chiral symmetry in the latter case ($\varphi = \pm 0.37\pi$) does not necessarily have a strong detrimental effect for the solitonic
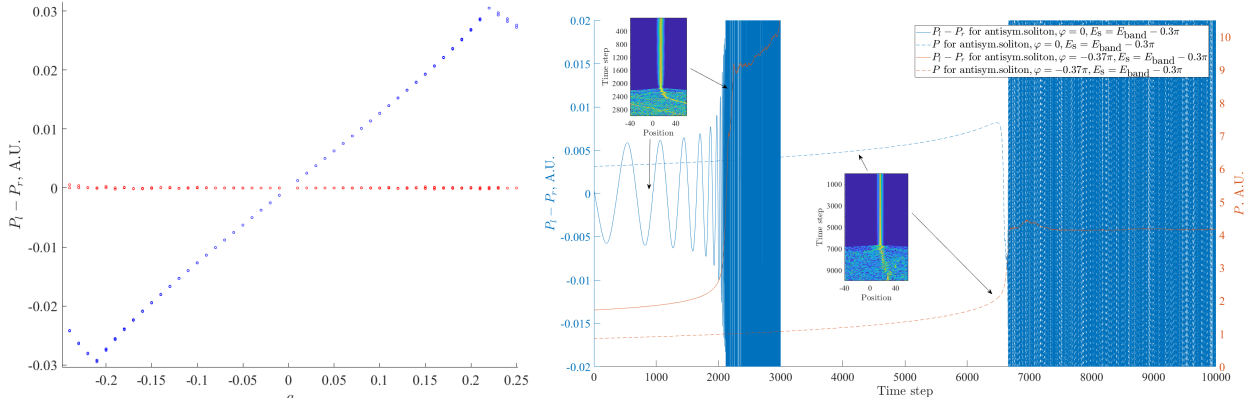
(a) A difference between total powers in l and r pseudospin components varying with g at $\varphi = 0$ (red dots) and $\varphi = \pm 0.37\pi$ (blue dots). The data are valid for both symmetric and anti-symmetric solitons.

(b) Exponential or linear power growth and super-exponential blow-up of the anti-symmetric soliton. Total power and the power asymmetry between pseudospin components are denoted by the red and blue color, respectively.

Figure 3.5

family in terms of $\mathcal{PT}$ symmetry breaking. Below, in the context of soliton's lifetime we will see that this is indeed true.

3. Regardless of the power balance between the pseudospin components $P_l - P_r$ and for any potential parameters, the total power of both symmetric and anti-symmetric solitons constantly grows with time, if $g \neq 0$ (see two examples for the anti-symmetric soliton in Fig. 3.5b). The initial power growth is linear and monotonic if $\varphi = 0$, and exponential, otherwise. The first type ($\varphi = 0$) is associated with the oscillating dynamics of the power disbalance $P_l - P_r$ if the soliton's initial power is high enough (see Fig. 3.5b). Low energetic solutions typically keep the power disbalance unchanged and almost zero during the evolution (not shown here), but nevertheless the total power is linearly growing, meaning that the power conservation condition derived in [128] can not be fulfilled exactly due to non-integrability of our system. In the second case ($\varphi \neq 0$), both the total power and the pseudospin power disbalance grow exponentially in time. This is in agreement with the dynamical equation for the powers, derived in [128]. Thus, in contrast to the previously described continuous dual-core waveguide system and owing to discreteness and non-integrability of our quantum walk, the parity-time symmetry should be locally (at least weakly) broken by nonlinearity of the soliton, even for the case $\varphi = 0$, when the power disbalance is very close zero. At the same time, note that this picture of local nonlinearity-induced breaking is in a way opposite to the conditions for global symmetry breaking, because in the linear limit $\mathcal{PT}$ symmetry is broken at $\varphi = 0$ and is recovered at $\varphi = \pm 0.37\pi$.

4. While the power increases, the soliton sweeps along the parametric family range towards higher propagation constants. At a certain power value (destabilization threshold), depending on the initial soliton's amplitude and the value of $|g|$, the power growth becomes super-exponential ("blow-up" phase). The estimation of the power thresholds for the symmetric and anti-symmetric solitons are provided in Figs. 3.6b and 3.6a, respectively. The provided values are however slightly overstated for larger $|g|$, because they are taken at the end of the "blow-up" phase. Afterwards, the super-exponential

amplification gets saturated and leads either to a complete dispersion of the soliton and to a chaotic field dynamics or, in addition, to a creation of transient oscillating solutions, the above mentioned discrete breathers (see the insets of Fig. 3.5b). If (φ) is around zero, the resulted field globally breaks the parity-time ($\mathcal{PT}$) symmetry of the lattice and the power of free propagating modes is steadily growing in time. If, however, φ is in the range of the recovered $\mathcal{PT}$ symmetry (we probe the solitons with the lowest powers at $\varphi = \pm 0.37\pi$) and the amplitude $|g|$ is below the $\mathcal{PT}$ symmetry threshold of about 0.15, which is reduced in the nonlinear regime with respect to the linear threshold of 0.44, the total power is approaching a plateau as shown in the Fig. 3.5b), implying that the global $\mathcal{PT}$ symmetry is recovered.

5. Clearly, the inevitable power growth in the beginning of the evolution follows directly from non-Hermiticity and non-integrability of the fully discrete system with a non-zero g. However, the mechanism of soliton's destabilization, associated with the power threshold and the super-exponential "blow-up" phase, has, similarly to the continuous integrable system [128], a purely conservative origin. Indeed, if the gain/loss amplitude $|g|$ is very small, the parametric "sweep" towards higher or lower propagation constants is adiabatically slow and thus the power threshold tends to the conservative destabilization threshold in the limit $|g| \to 0$ (see the horizontal bars in Figs. 3.6b and 3.6a). If, however, $|g|$ is large but still below the nonlinear parity-time threshold of about 0.15, the power "sweep" happens faster than a typical lifetime of the unstable solution. Therefore, the soliton's power can grow up until a propagation constant of some intermediate unstable solution of the family, which typically turns into a less energetic and more stable oscillating solution, a discrete analogue of the previously mentioned breather [133]. Another part of power gets radiated outwards into the bulk. If the amplitude $|g|$ exceeds the nonlinear $\mathcal{PT}$ threshold of about 0.15, the soliton quickly sweeps across the entire parametric space until it meets the opposite linear band and disperses into free propagating waves. Total power of the resulted field is exponentially growing in time without bounds, meaning that the global parity-time symmetry of the lattice is broken.

6. The destabilization power thresholds for the symmetric and anti-symmetric solitons are approximately equal and up to the $\mathcal{PT}$ threshold $|g| = 0.15$ they in average follow the logarithmic laws $\sim a + b \log(|g| + c)$ with the fitting parameters depending on $|\varphi|$, according to the numerical data in Figs. 3.6b and 3.6a. This is in contrast to the symmetric and anti-symmetric families of the continuous system [116, 122, 126–129], where they follow individual square root laws and the symmetric solutions are stable below the threshold, while the anti-symmetric one is always unstable.

7. Soliton's lifetime τ, which is defined as the number of time steps until the power threshold is reached and the soliton blows up, is also approximately the same for both chiral symmetric families. For low energetic solutions at $\varphi = 0$ and at $|g| \leq 0.15$, it follows a hyperbolic law $\tau \sim \alpha/|g|$ (see Figs. 3.7a and 3.7b), where α depends on the initial power of the soliton. In contrast, if $\varphi = \pm 0.37\pi$ the lifetime gets much higher for small $|g|$ and as such follows instead the inverse-square law $\tau \sim \alpha_2/(|g| + g_0)^2$, where g_0 is a small positive offset and $\alpha_2 \approx \alpha/10$. Note, that non-zero offset g_0 in the fitting models might indicate than the solitons have finite lifetimes even in the conservative limit, however our earlier simulations of the evolution at $\varphi = \pm 0.37\pi$ up to 20000 time steps did not reveal any growing instability.

8. We see that both inversed power laws have an integer exponent index (1 or 2) and therefore we can conclude that the lifetime enhancement in the $\mathcal{PT}$-recovered phase should happen abruptly at some intermediate value of φ. Such an abrupt change might be a signature of a certain parity-time symmetry phase transition in the nonlinear regime, meaning that similarly to the conservative case the phase transition is possible only through a certain exceptional point. It is interesting to observe, that even for the non-conservative unstable solitons the global recovered $\mathcal{PT}$ symmetry still plays a positive revitalizing role in terms of abruptly enhanced lifetimes of the solitons, despite the fact that the power disbalance between pseudospin components associated with chirality is lower in the globally broken unmodulated lattice. Finally, note that the hyperbolic and inverse-square laws are qualitatively different from the exponential law found in [128] for the unstable asymmetric single point solution.

9. Combining the logarithmic law for the power threshold and the hyperbolic law for the lifetime in the unmodulated case $\varphi = 0$, we get specifically for the "close-to-band" low energetic solutions, that

$$\tau_{\text{sym}} \approx \frac{33.1}{0.0117 e^{\frac{P_{\text{thr}} - P_{\text{thr}}(g=0)}{3.353}} - 0.013}, \tag{3.4}$$

$$\tau_{\text{asym}} \approx \frac{32.7}{0.0136 e^{\frac{P_{\text{thr}} - P_{\text{thr}}(g=0)}{3.596}} - 0.017} \tag{3.5}$$

for the symmetric and anti-symmetric solitons, respectively. The power threshold $P_{\text{thr}}(g = 0)$ is equal to 4.262 in the conservative limit. Thus, we can presume that the average lifetime of the non-Hermitian solitons below the $\mathcal{PT}$ threshold in the unmodulated lattice obeys Bose-Einstein statistics:

$$\tau_{\text{B-E}} \sim \frac{1}{e^{\frac{\Delta P_{\text{thr}}}{P_0}} - 1}, \tag{3.6}$$

where P_0 is approximately in the range between 3.353 and 3.596. In the modulated $\mathcal{PT}$-recovered case $\varphi = \pm 0.37\pi$, the lifetimes should approximately follow a square of the Bose-Einstein distribution due to its quadratic enhancement by the $\mathcal{PT}$-symmetric phase recovery.

In conclusion, we investigated numerically the non-Hermitian extensions of the chiral fundamental symmetric and anti-symmetric solitons in the parity-time symmetric environment. Both families were found intrinsically non-conservative and unstable with finite lifetimes, in average obeying Bose-Einstein statistics in the unmodulated lattice. It is argued that the destabilization mechanism for non-Hermitian solitons is essentially conservative, despite that the instability is accompanied with a super-exponential blow-up of power. Remarkably, $\mathcal{PT}$-symmetric potential with the potential height of $\pm 0.37\pi$ belonging to the recovered $\mathcal{PT}$ range of the linear system (see Fig. 1.17c) significantly elongates soliton's lifetimes τ at small $|g|$ by imposing an inverse-square law on τ with respect to $|g|$ instead of the hyperbolic law in the $\mathcal{PT}$ symmetry broken case. Consequently, the lifetime statistics versus the energy threshold increment has to be modified into a peculiar squared Bose-Einstein distribution. Commonly, soliton's lifetime drops abruptly and an unbounded power growth after the "blow-up" phase takes place, if $|g|$ exceeds approximately 0.15, indicating that $\mathcal{PT}$ symmetry gets broken globally at the much lower value of gain/loss parameter, than in the linear regime (~ 0.44). Finally, in a great contrast to the symmetric-antisymmetric pair of families found in the
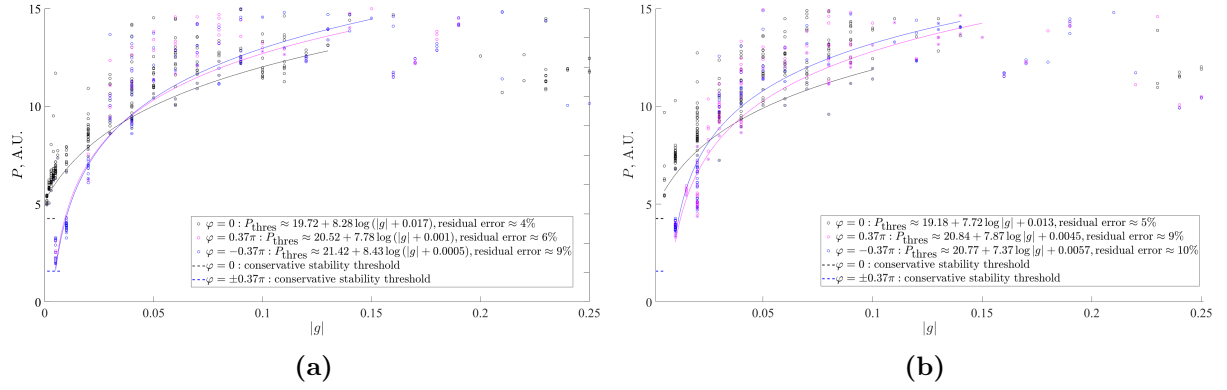
Figure 3.6: (a) Critical blow-up powers of anti-symmetric (left) and symmetric (right) solitons with various propagation constants, in the broken (black) and recovered (blue, magenta) $\mathcal{PT}$ phases, estimated right after the blow-up. The lower bound of the data (power threshold) is well approximated by a logarithmic fit up to $|g| \approx 0.15$. (b) Critical blow-up powers of symmetric solitons with various propagation constants, in the broken (black) and recovered (blue, magenta) $\mathcal{PT}$ phases, estimated right after the blow-up event. A logarithmic fit of the lower bound (threshold) is also in place up to $|g| \approx 0.15$.

continuous double-core waveguide 1D system, our chiral pair of solutions have almost the same lifetimes and stability properties, implying that chirality features of the solitons play a very little role for their stability in the parity-time symmetric non-Hermitian environment, provided that the global $\mathcal{PT}$ operator (1.203) does not exchange sublattices and thus it does not correlate with the chiral operator.

3.1.3 2D conservative solitons

We begin our study of two-dimensional solitons in the time-multiplexed Discrete Quantum Walk with the conservative case, where the band structure is appropriately modified via the real parity-time symmetric phase potential, introduced earlier in section 1.8.2. Previously, we found out that the chiral conjugate pair of 1D symmetric and anti-symmetric soliton families, bifurcating from opposite bands, have the same or approximately the same stability conditions in both conservative and non-Hermitian lattices. As we will see further, real part of the parity-time symmetric potential is quasi-one-dimensional in the 2D lattice and thus it can be effectively reduced to a one-dimensional walk. Therefore, we can again expect the same or almost the same stability conditions for the symmetric and anti-symmetric families in the 2D system and without loss of generality to concentrate further only on the anti-symmetric family, which is also relevant from the experimental point of view. Besides, it will be shown that the heights of the real potential delivering recovered $\mathcal{PT}$ symmetry in the linear regime are also beneficial in terms of soliton's lifetime enhacement. Thus, throughout further discussions we fix the height φ specifically to 0.3π, which is in the range of recovered global $\mathcal{PT}$ phase, according to Fig. 1.20b. In this point, the band structure consists of four bands (see Fig. 2d in [B3]). Provided the nonlinear coefficient γ is positive, the soliton family bifurcates from the negative intermediate band[1], resembling a parabolic valley elongated in one of the diagonal directions. Thus, the entire family could be traced out similarly to the 1D solitons up to the opposite band and starting from the extended asymmetric bulk mode

---

[1]Note, that in the articles [B3, B4] we used another sign convention for the Floquet-Bloch ansatz, and therefore the asymmetric family bifurcates from the upper band instead.
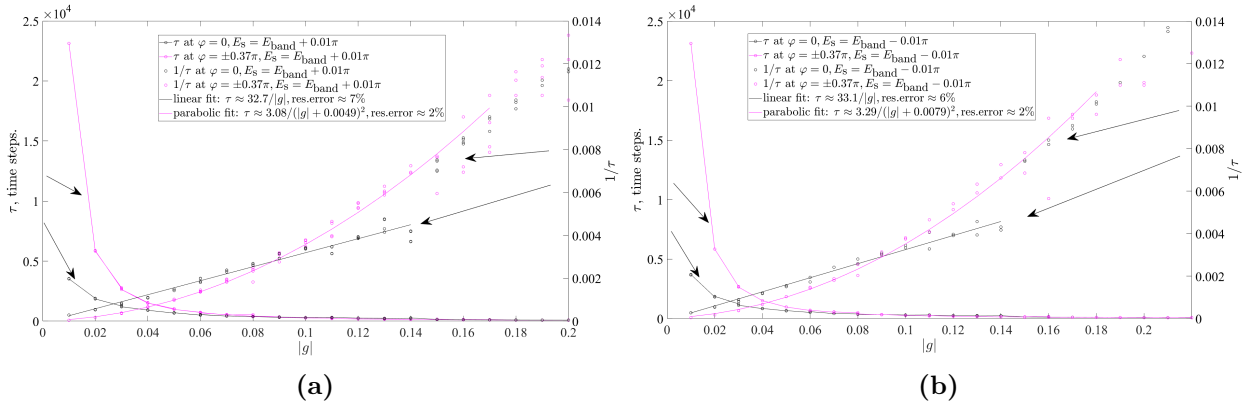
Figure 3.7: (a) Lifetimes of the low energetic anti-symmetric solitons in the PT recovered (magenta) and broken (black) phases versus gain/loss amplitude. (b) Lifetimes of the low energetic symmetric solitons in the PT recovered (magenta) and broken (black) phases versus gain/loss amplitude.

with zero quasimomentum and the quasienergy $E \approx -0.227\pi$. The size of the numerical square domain was 40×40, with periodic boundary conditions. As one can see in Fig. 3.8, the spatial profiles of the "close-to-band" solutions are elongated in the diagonal direction as they inherit the reciprocal geometry of the band of origin. Further, we will also see that the soliton inherits topological charge (Berry phase) of the respective band. As the propagation constant exceeds approximately -0.2π, the profile becomes much narrower and the soliton looses its stability, as indicated by the lifetime (see the inset of Fig. 3.9). This family of solitons is a modified and deformed version of the fundamental gap soliton's family, which occurs in our system for the Schrödinger-like parabolic bands introduced via the previously considered periodic potential at $\varphi = \pi/4$ (see eq. (1.72), Fig. 1.13 and also the work [B4]) and which is very similar to the fundamental gap solitons found in continuous periodic media with cubic nonlinearity [134] and in the discrete lattices with the local cubic or with the nearest-neighbour Ablowitz-Ladik nonlinearity type [135]. In particular, these solutions, commonly in two dimensions and in contrast to 1D solitons, have a minimum critical total power, required for them to form from the band of origin. In our case, the minimum power is about 1 (see Fig. 3.9). In addition, these solutions loose their stability if the so-called Vakhitov-Kolokolov criterium ($dP/dE_s < 0$) is satisfied. In our case, the stability seems to be lost regardless of this criterium and even slightly before the point $E_s \approx -0.18\pi$, where the power growth on the characteristic curve (see Fig. 3.9) slows down almost to zero. This might be due to discreteness of the lattice, that can effectively reduce the power instability threshold according to [136].

In more details, below this critical value the soliton is not exactly static, but it performs weak periodic oscillations of the amplitude profile, reminding a breathing process and therefore we can identify this quasi solution as a discrete breather [133], similarly to the above mentioned studies on the discrete systems. The broad "close-to-band" breathing solutions are less sensitive to discretization effects of the lattice and therefore they approximate, although being elongated along the diagonal direction, the so-called Townes soliton [137], [138], which is a stationary radially symmetric solution of the continuous 2D nonlinear Schroedinger equation with cubic nonlinearity. Obviously, a more closer analogue of the Townes soliton in our 2D Discrete Quantum Walk is realized via the radially symmetric parabolic potential (see [B4]). Moreover, such breathing (below a certain power threshold) Townes-like solitons are typical for the previously mentioned lattices with local cubic or

Ablowitz-Ladik nonlinearity [135].

It is well known, that genuine Townes solution of the continuous system in which nonlinear focusing and diffraction have to precisely balance each other, is unstable and, consequently, it is dispersively spreading all over the space, if its power fluctuates towards lower values, and collapsing into a point-like solution in a self-similar fashion within a finite time, otherwise. In contrast to the genuine collapse in the continuous system, if the critical value of total power is exceeded for the soliton in our Discrete Quantum Walk, the solution after some propagation time experiences a sudden quasi-collapse[2] into a less energetic highly-localized and mobile solitary wave. The excess of energy is released during the quasi-collapse in the form of free propagating waves. Again, this scenario is also typical for the discrete systems studied in [135] and therefore the quasi-collapse towards a more stable highly-localized inherently discrete solution is a generic phenomenon in discrete lattices with Kerr-type nonlinearity.

Similarly to the lattice under our consideration (with the elongated band structure due to the parity-time symmetric potential), our experimental work [B4], dealing with the radially symmetric parabolic dispersion, outlines the same two basic scenarios for the Townes-like soliton, namely we could experimentally observe its quasi-collapse into a more stable single-spike stationary solution with a lower power. Moreover, our numerical analysis showed (not presented in the article) the presence of many more static long-living highly-localized states with low powers, including periodically pulsating and double-spike dipole solutions. Interestingly, the pulsating single-spike after-collapse solutions (with the period of two time steps) were found having slightly smaller powers and therefore being slightly more stable than the stationary single-spike after-collapse solution, however, because of extremely huge typical lifetimes of both families, the experiment after the quasi-collapse event taking place within 60 round trips of propagation (see [B4] for details) revealed only the stationary single-spike state.

In conclusion, we have given a brief description of the exclusively two-dimensional[3] and discrete phenomenon of quasi-collapse, because our next step in the thesis will be to extrapolate this effect towards non-Hermitian solitons in the parity-time symmetric environment and to see its interplay with the originally one-dimensional phenomenon of super-exponential blow-up.

3.1.4   2D non-Hermitian solitons

Before proceeding with the non-Hermitian case, we note that the spatial pattern of the parity-time symmetric real potential, parametrized by φ and depicted in Fig. 1.20a, consists of periodically alternating zigzag-shaped diagonal stripes of a constant potential ($+\varphi$ and $-\varphi$). As a result, the pattern is quasi-one-dimensional, meaning that the lattice can be effectively reduced (with periodic conditions) down to one-dimensional chain oriented along the diagonal, perpendicular to the stripes of a constant potential, so that the resulted pattern will preserve the parity-time symmetry with respect to the remaining diagonal dimension. Although such an effective $\mathcal{PT}$ symmetry preserving lattice reduction takes away the mobility of solitons and linear waves in one diagonal dimension, provided the blow-up can be in principle observed in the original 2D lattice with the quasi-1D potential, it should essentially

---

[2]The prefix "quasi" reflects the fact that in the discrete system the collapse event ends up with another solitonic inherently discrete solution, having a finite width. The term "quasi-collapse" has been also used for other discrete lattices, for example in [135] and [136]

[3]A more general condition for the collapse is given by the Vlasov-Petrishchev-Talanov theorem [138], which reads $(p-1)D \geq 4$, where p is the order of nonlinearity and D is the dimensionality of the system
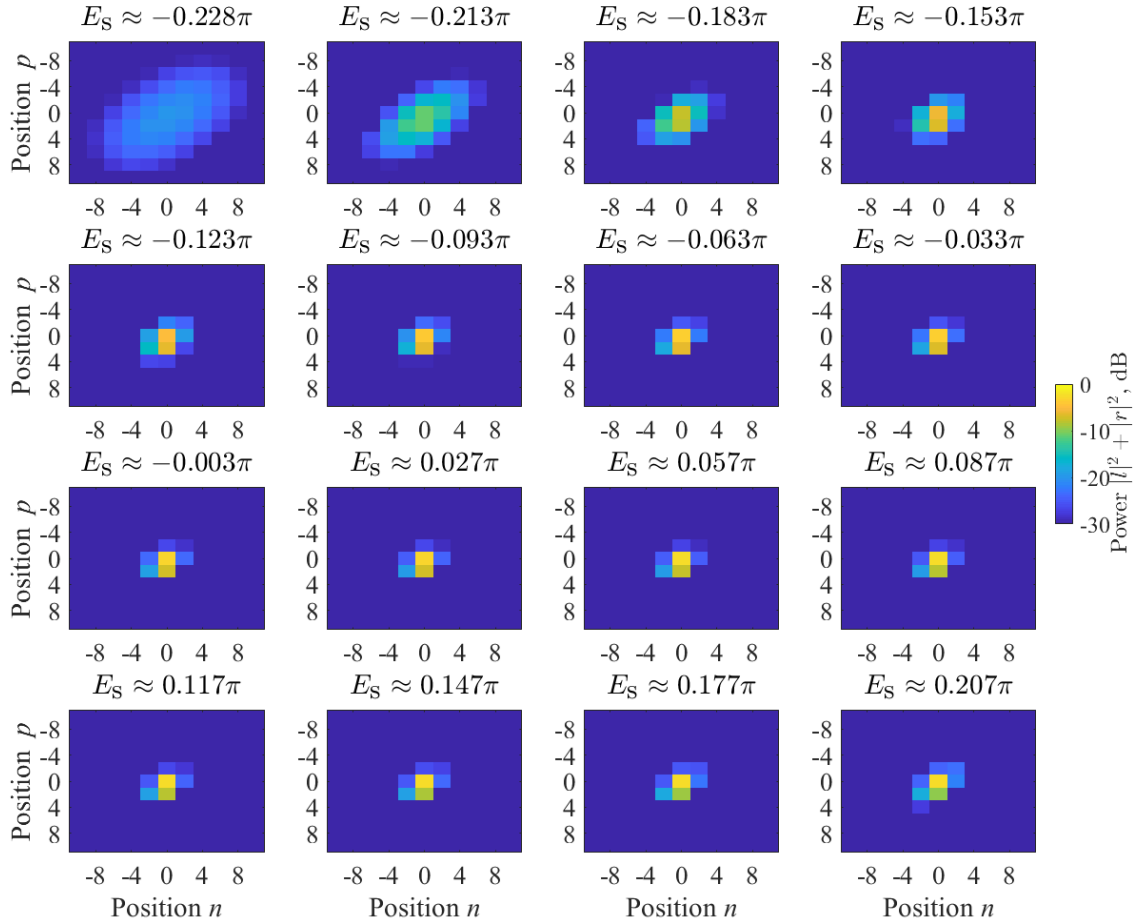
Figure 3.8: Amplitude profiles of the numerical solitonic solutions at different propagation constants. Close to the band of origin, the cigar-shaped soliton is broad and thus resembles the Townes soliton of the continuous Schrödinger equation. Far from the linear band, the soliton is very localized and radially more symmetric, than in the Townes-like case.

be similar and share many common features with the blow-up of 1D non-Hemritian solitons. Indeed, simulations and experiments show almost the same scenario for the instability: a non-Hermitian soliton, which branches from its non-conservative counterpart and appropriately adopts its energy and shape (see Fig. 5 of [B3] for details), experiences an exponential power growth (see the inset of Fig. 3.10) in presence of the parity-time symmetric phase. Note, that the non-Hermitian solutions in contrast to the conservative one skip the turning point of bifurcation in Fig. 5 of [B3], indicating that the resulted low energetic conservative branch does not have an (even unstable) non-Hermitian extension as it possibly breaks parity-time symmetry. In this context, we only mention the fully continuous 2D Schrödinger model, in which non-$\mathcal{PT}$-symmetric solitons can exist only for some special class of $\mathcal{PT}$-symmetric potentials (see [139, 140] for details).

As the total power of the soliton grows higher, the soliton sweeps through the parametric family until it reaches a certain power threshold, triggering a "blow-up" event. Similarly to the one-dimensional soliton, the lowest power threshold has been estimated as a logarithmic curve versus the gain/loss parameter g. Note, that we considered only positive g values, since the same power thresholds should be valid for negative gain/loss parameters as well. Above
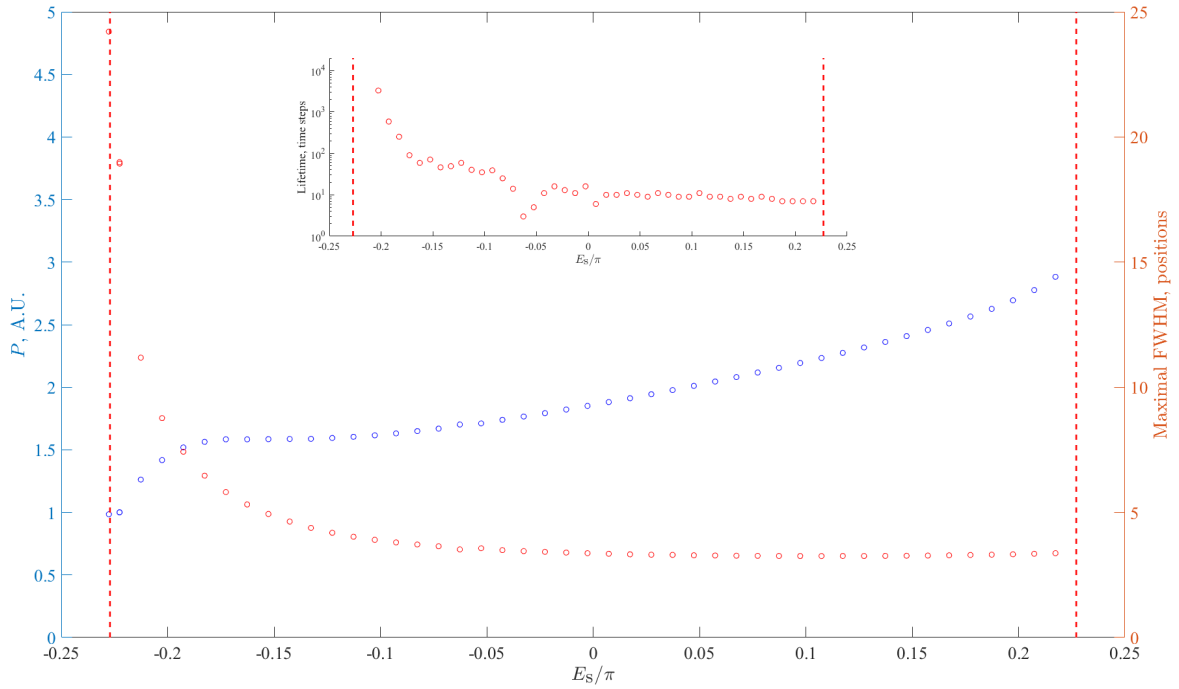
Figure 3.9: Total power and full width at half maximum of the soliton with varying propagation constants. The width has been estimated from a gaussian fitting model applied along the diagonal with the maximum profile extension. The inset shows the lifetime, loosly defined as a number of time steps until the total amplitude deviation between subsequent time steps is below 0.01 % of total power. Only broad solutions are (quasi)stable, i.e. they can slightly "breath" without being destroyed. More localized solutions tend to quasi-collapse into other more stable highly-localized states with lower powers.

a certain value of g, previously referred to as the nonlinear $\mathcal{PT}$ threshold, the logarithmic law is violated since the blow-up takes place almost immediately, finally leading to a chaotic field evolution accompanied with a boundless power amplification. One can see, that for the widest g-region of recovered parity-time symmetry in the linear regime (see Fig. 1.20b), corresponding to $\varphi = 0.3\pi$, the nonlinear $\mathcal{PT}$ threshold is higher than in case of smaller potential heights φ. Interestingly, the lifetimes τ of "close-to-band" low energetic solitons, defined as the number of time steps until the blow-up event, again satisfy the inverse-square law, previously found for one-dimensional non-Hermitian solitons in the $\mathcal{PT}$-recovered phase (see Fig. 3.11). Therefore, we can similarly conclude about the lifetime enhancement triggered by an abrupt transition to the $\mathcal{PT}$-recovered phase. Thus, statistics of average lifetimes in the $\mathcal{PT}$-recovered phase versus power thresholds should satisfy the peculiar squared Bose-Einstein distribution. Despite the above described statistical correspondence of 2D non-Hermitian solitons in the quasi-1D parity-time symmetric environment and 1D non-Hermitian solitons, a more detailed analysis shows the following distinctions. If g is not too high, thus providing an adiabatic sweep of the soliton's parameter, and the initial state has relatively low energy, then after an exponential growth the non-Hermitian 2D soliton will most likely loose its energy ("endothermic" blow-up, see the inset of Fig. 3.10), will fall into a "close-to-band" broad Towns-like solution, which will broaden even further while moving along the diagonal stripe of a constant potential. This scenario is illustrated in Fig. 3.12. The soliton's broadening indicates that the soliton still dissipates some power during the propagation, although the total power in the lattice appears almost constant in
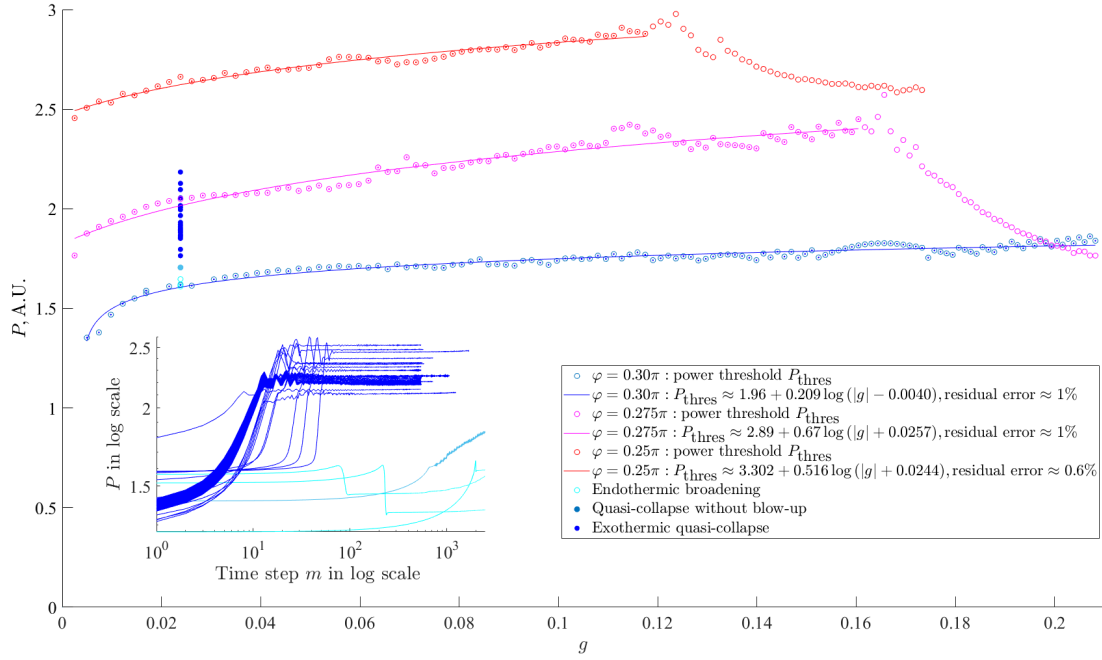
Figure 3.10: Power thresholds of 2D anti-symmetric solitons at various PT recovered phase potentials. Calculated for low energetic "close-to-band" solutions, they outline the lowest bound for all other solutions with higher powers and propagation constants. The insets show typical blow-up scenarios at the fixed value of g.
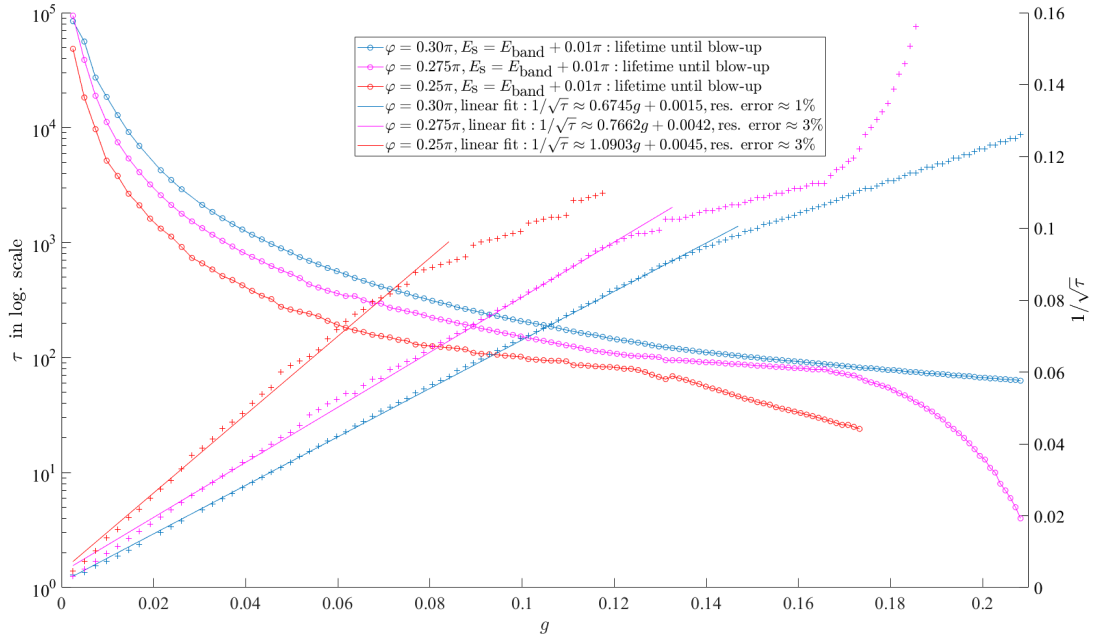

Figure 3.11: Lifetimes of the "close-to-band" solutions. Linear fits of the reversed quadratic law indicate an abrupt lifetime enhancement due to recovered PT symmetry, similarly to the 1D solitons.

time. In [B3], it has been suggested that the dissipation is due to soliton's interaction with the zigzag-shaped discrete potential barrier, which can be effectively modeled by the so-called Peierls-Nabarro potential, generally arising from nonintegrability of discrete systems [141]. Conversely, if g and/or the initial total power are high enough, the soliton will most likely experience an "exothermic" blow-up (again, see the inset of Fig. 3.10), which is accompanied with a super-exponential power growth and which has been commonly observed for the one-dimensional solitons. In this case, simultaneously with the blow-up the soliton undergoes a quasi-collapse into a less energetic highly-localized post-collapse state. The low energetic soliton similarly to a rocket gets boosted by an excess of energy travelling away from the soliton in the form of free propagating waves (see Fig. 3.13). Provided g is not too high, the resulted soliton typically quickly disperses due to its interaction with the zigzag-shaped discrete potential, which is generally more detrimental for highly-localized discrete modes than for the extended Townes-like solutions. However, at a large enough g the post-collapse soliton gets further amplified during the propagation and thus while releasing an excess of energy, it gets successively accelerated. This effect, coined "self-acceleration", along with the non-Hermitian quasi-collapse has been experimentally observed in our system [B3]. Despite this effect, the highly-localized soliton eventually disperses because of its strong interaction with the Peierls-Nabarro barriers, introduced by the corners of the zigzag-shaped potential. Note, that the direction of the post-collapse soliton is also diagonal and along the zigzag-shaped potential stripes, but is opposite to the direction of the moving broad Townes-like soliton, suggesting that the direction of motion is directly connected to whether the soliton undergoes amplification or attenuation. Remarkably, when g and the initial soliton power are finely tuned, one can observe the third scenario, in which the soliton does not blow up at all, but nevertheless it is quasi-collapsing into a less energetic state (see Fig. 3.14), which in contrast to other two scenarios does not continuously move in any diagonal direction, but instead it can slowly tunnel through the zigzag-shaped potential barrier and afterwards follow some complex crooked trajectory. The resulted after-collapse solution can live very long in the lattice, provided that the total power is growing very slowly in time and the soliton does not get much disturbed by the zigzag corners of the potential since it is not moving along the diagonal. In the Fig. 3.10, at the fixed $g \approx 0.024$ we plot all powers of the non-Hermitian solitons, triggering the blow-up event. We see that the first endothermic scenario is typically realized when the onset power just slightly exceeds the lowest threshold value, while the second scenario is in place when the crossing power is significantly higher than the threshold value. As expected, the finely tuned third scenario without blow-up demarcates the two "exothermic" and "endothermic" blow-up scenarios.

Finally, while the non-zero momentum acquired by the post-collapse solution after the blow-up can be comprehended at least classically as the above mentioned mutual repulsion of the soliton and the excessive travelling plane waves, the reason for a non-zero momentum of the broadened solution after the "endothermic" blow up is less obvious and requires instead a quantum picture for understanding. To shed some light on this question, we refer to the spatial phase distribution of one of the pseudospin components (see upper insets the in Fig. 3.12). The first three distributions reveal a rotation of the phase front (red line) in the counterclockwise direction, indicating that the initial unstable solution has an internal quantum angular momentum. This momentum is a result of an intrinsic chirality of the soliton. Note, that the phase front does not perform the full rotation by 2π radians, but only by π radians. This supports the idea that the anti-symmetric soliton inherits the topological charge (Berry phase) of the band of origin. Indeed, in section 1.4 we found out that two bands of the 2D time-multiplexed system merging in the center of the Brillouine zone into

a Dirac point have the Berry phase of $\pm\pi$, which is however not generic as follows from the topological classification of the linear 2D lattice. Since the parity-time symmetric potential with the height of $\varphi = 0.3\pi$ while deforming the bands, does not in fact close the central gap, we can expect the same topological charge in the parity-time symmetric lattice as well. Thus, we anticipate a clockwise half-way rotating phase front for the symmetric family of solitons, bifurcating from another band. Coming back to the problem of non-zero momentum, as the soliton undergoes the blow-up transition, the rotating phase front quickly transforms into diagonally moving planes as shown in the Fig. 3.12. Thus, the quantum angular momentum is transformed into the directional diagonally oriented quantum momentum. Now, recalling that the resulted broader Townes-like solution "feels" a much weaker Peierls-Nabarro barrier, represented by the corners of the zigzag-shaped potential, we can eventually understand why this transformation happens. The potential barrier played the role of a tension force for the initial soliton, thus allowing the rotation. When the barrier was relaxed due to the "endothermic" blow up, the broad soliton was carried away by some kind of centrifugal force. Note, that this explanation in terms of spatial phase distribution hardly works for the scenario of quasi-collapse, because it is difficult to identify the phase front for the highly-localized post-collapse solution.

In conclusion, we investigated the non-Hermitian 2D solitons in the parity-time symmetric environment with the quasi-1D real potential. We found that the solitons are intrinsically unstable, similarly to the 1D non-Hermitian solitons they experience an exponential power growth and the super-exponential blow-up phases as in the 1D lattice. Moreover, simulations indicate that $\mathcal{PT}$-recovered phase of the lattice enhances the lifetime of the non-Hermitian solitons in comparison to the $\mathcal{PT}$-broken phase and thus, similarly to the 1D case the average lifetime obeys squared Bose-Einstein statistics. On the other hand, the blow-up can be "endothermic", i.e. lead to an abrupt power loss and broadening of the resulted Townes-like soliton, or "exothermic", manifesting itself as a rapid power growth and soliton's quasi-collapse into another highly-localized discrete solution. Importantly, when the gain/loss and initial total power of the soliton are finely tuned, the quasi-collapse can happen without the super-exponential blow-up. In case of the "endothermic" and "exothermic" blow-ups, the resulted Townes-like solution and the highly-localized state acquire certain momenta, diagonally oriented in mutually opposite directions. For the moving highly-localized state, this circumstance has been explained as a repulsion of the soliton from oppositely propagating waves, carrying away the excess of energy after the blow-up. The motion of the Townes-like soliton, could be understood only on the quantum level as a transformation of the internal quantum angular momentum of the initial chiral soliton with the topological charge π into a translational quantum momentum, due to a sudden blow-up driven release of the potential barrier.

3.2   Topological edge states in the 1D Walk

The second part of my doctoral research is devoted to the so-called symmetry-protected topological order in the 1D Quantum Walk and the associated edge and interface states, which can appear at an open end of one and between two topologically distinct phases, respectively, due to the previously mentioned bulk-edge correspondence principle (see section 1.7 for details). Owing to the property of topological protection, such states can serve as scattering-free and efficient transport channels, robust against symmetry-preserving perturbations. Although they were originally discovered within condensed matter physics [142–144], later they be-
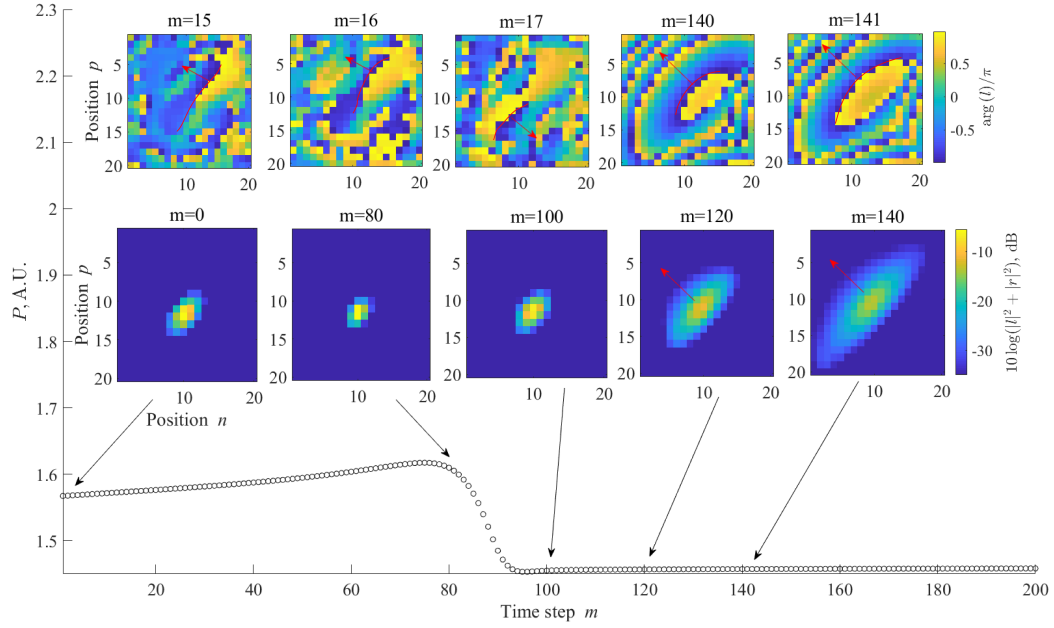
Figure 3.12: "Endothermic" blow-up of an initially broad Townes-like soliton accompanied with soliton's broadening and a momentum boost in the north-west diagonal direction. The insets show phase distribution of the field.
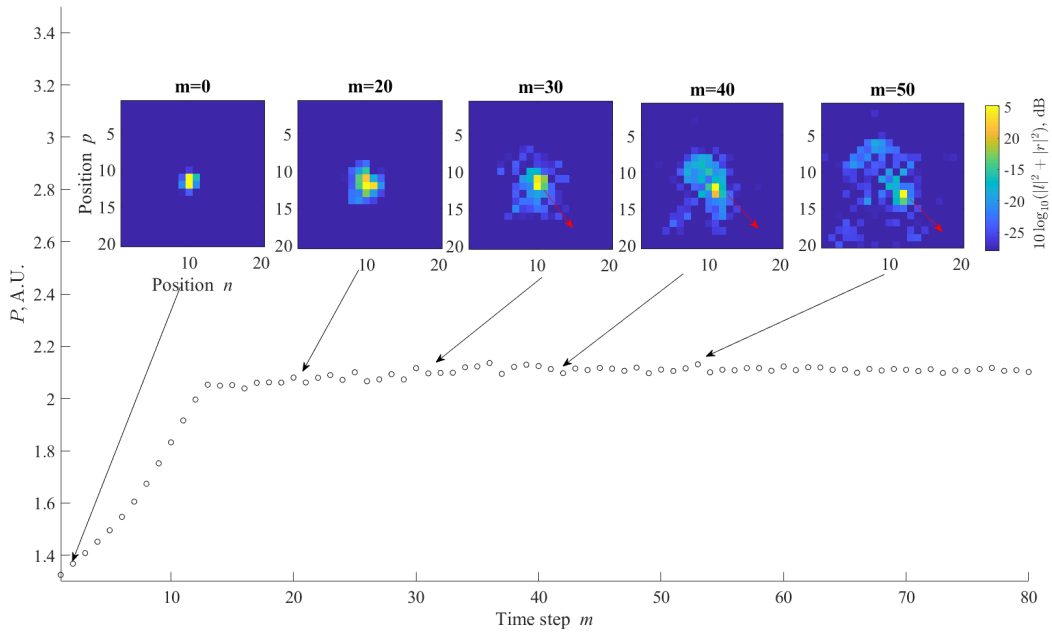

Figure 3.13: "Exothermic" blow-up of an initially narrow Townes-like soliton accompanied with soliton's quasi-collapse into a less energetic highly-localized mobile solution, moving toward south-east. Global $\mathcal{PT}$ symmetry is almost recovered after the blow-up phase.
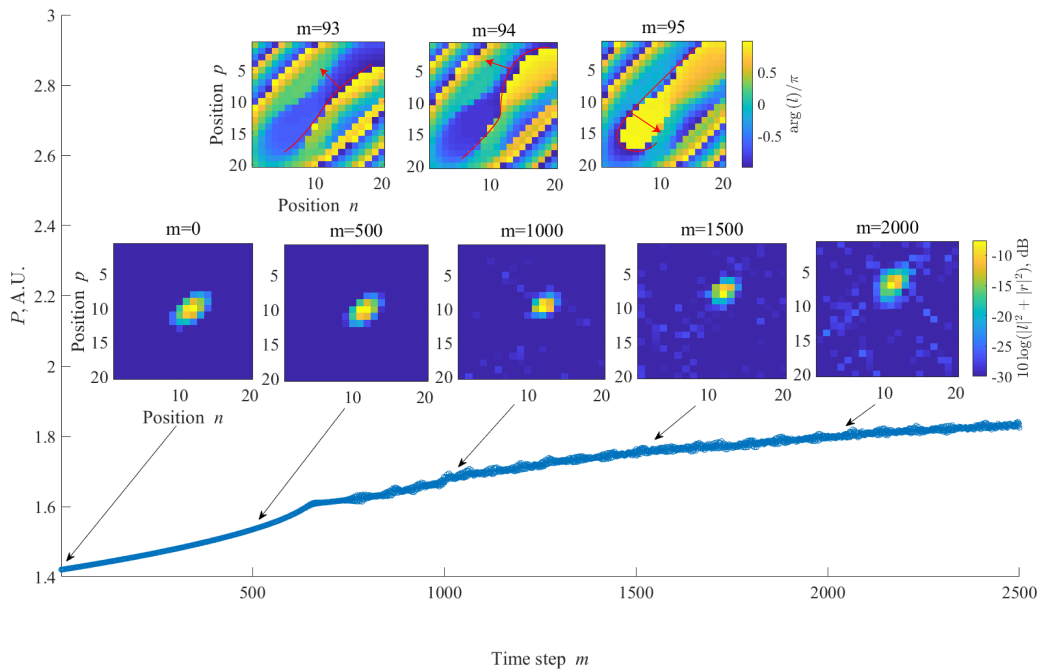
Figure 3.14: Finely tuned quasi-collapse transition without power blow-up. The resulted soliton acquires a little to no momentum, slowly surpasses the potential barrier and randomly wonders on the lattice.

came experimentally accessible in various optical systems: in photonic arrays and crystals [145–148], metamaterials [149], coupled resonator arrays [150, 151], quasi-crystals [152–154] and photonic quantum walks [155, 156]. Furthermore, realization of topological phases and edge states has been proposed [82, 90, 157–160] and observed [146, 156, 161, 162] in non-Hermitian optical systems.

The simplest known (1+1)D lattice, supporting symmetry-protected topological edge states, is the celebrated Su-Schrieffer-Heeger (SSH) model [163], describing conduction properties of a one-dimensional chain of polyacetylene, which consists of carbon-hydrogen molecules (C-H) with alternating single- and double-bondings between nearest neighbour carbon atoms. In particular, the SSH model describes the hopping of effectively non-interacting electrons between outermost electronic orbitals ($\pi-$orbitals) of carbon atoms. According to the topological classification [65], the SSH chain belongs to the chiral BDI class of 1D topological insulators, characterized by an integer winding number. Note, that hopping (tunneling) of electrons between adjacent $\pi-$orbitals takes place continuously in time, as follows from Schrödinger equation. A semi-infinite SSH chain with one end terminated at the "strong" interatomic bonding (topologically non-trivial case) necessarily supports one defect state, that is localized at the edge of the chain and that spectrally appears at $E = 0$, which is the middle of the band gap, separating a covalence and conduction bands of extended bulk modes of the chain. Topological protection of a chiral edge state is ensured by preserved chiral symmetry of the bulk, meaning that none of the perturbations, being applied in the vicinity of the edge and preserving chiral symmetry of the bulk, are able to spectrally shift the state from its mid-gap position and therefore to significantly disturb its wavefunction amplitude profile. Due to a simplicity of the SSH model, treating the hopping electrons as effectively non-interacting and spinless particles, the model can be equivalently applied to bosonic systems, in particular to photonic ones based on arrays of weakly coupled waveguides

or photonic lattices. In this regard, SSH chiral defect states have been observed in various experimental platforms based on such periodic structures [161, 164–166].

Next, an extension of the SSH model and chiral edge states to their periodically driven (Floquet) counterparts have been discovered [62], [63] and experimentally implemented in photonic quantum walks [155]. A typical features of such Floquet SSH-based models are their band structure, which is in addition periodic in energy, and the occurrence of a second band gap around $E = \pi$. The new band gap can feature a topologically protected mid-gap edge state at $E = \pi$, manifesting one additional topological invariant $\mathbb{Z}$, as argued in [75]. In contrast to the SSH edge state at $E = 0$, associated with a motionless particle having zero kinetic energy, the new mid-gap state at $E = \pi$ inherits a certain internal dynamics, which stems from periodic Floquet drive of the system [75, 167].

It is known, that interactions between particles can in general destroy or alter the symmetry-protected topological order [168] of linear systems, as, for example, mathematically illustrated in [169] by the reduction of the BDI to the $\mathbb{Z}_8$ class in 1D. In particular, a chiral edge state, that is mid-gapped in the linear limit, does typically leave its mid-gap position and thus may loose its topological protection, once interactions are in place. This happens because an interaction potential (typically of a local or nearest-neighbour type) locally breaks chiral symmetry of the underlying linear system, as it was shown for fermionic [170],[171] and bosonic [172] cases. Such an interaction can even close the gap and destroy the state, if the interaction strength is above a certain critical value. The most explored and common type of interaction in 1D and 2D systems is a repulsive spinful [173],[174],[175],[171],[176],[170] or spinless [177],[172] Hubbard term, modifying the topological linear SSH model or some even more complicated network, as for example in [176]. In the original electronic SSH model [163], for example, the interactions are associated with electron-phonon coupling, thus allowing for a nonlinear modification of the chain topology and eventually may even lead to self-induced topological solitons. Nevertheless, general observation of the previous studies is that a weak or even moderate local (on-site) interaction may still preserve symmetry-protected order of the underlying linear system, so that a topological edge state, even without being exactly mid-gapped, may still adopt to nonlinear conditions and remain a stable particle channel, that is robust against a large class of symmetry-preserving local disorders. However, in order to formulate a more accurate criterium, one would have to generalize the bulk-edge correspondence principle to systems with broken translation invariance, as proposed, for example, in [167] for one-dimensional Floquet insulators.

Specifically in optical experiments, robust topological edge states have been observed even in open dissipative strongly nonlinear environments, such as exciton-polariton SSH chains fabricated in the appropriately structured semiconductor microcavities [178] or in arrays of coupled split-ring resonators with a magnetic dipole resonance in GHz frequency range [179]. Strong enhancement of a third harmonic signal at a topological edge state of a zigzag array of dielectric nano-resonators has been reported [180]. Apart from edge states, topological gap solitons [181] have been recently observed in a 2D Floquet insulator based on a laser-written waveguide array with local Kerr nonlinearity [182]. Another works, combining topological protection with nonlinear effects, concern topological insulator lasers [183], [184]. Lasing in the topological edge states of one-[178] and two-[185]dimensional lattices has been demonstrated under incoherent excitation of microstructured semiconductor microcavities operating in the strong coupling regime.

In what follows, we further contribute to that relatively new research area, promising novel optical devices that shall combine both nonlinear features of self-tunability and non-

reciprocity with topological robustness. Namely, we will study chiral symmetry-protected edge states of the fully discrete 1D Quantum Walk with an inhomogeneous coupling, belonging to the non-trivial BDI class according to section 1.7, in the presence of focusing on-site Kerr nonlinearity. The latter is induced experimentally via self-phase modulation of pulses in our one-dimensional time-multiplexed fiber loop set-up, while the coupling between lattice sites can be modulated in both artificial time and space via the voltage-driven variable coupler. In particular, we will distinguish two types of edges and, respectively, two types of edge states in our discrete Floquet system, in contrast to one edge type in the SSH chain. Next, we will study numerically the existence and stability conditions, valid for nonlinear counterparts of the chiral edge states, using the standard self-consistency method and linear stability analysis. Finally, we will demonstrate experimentally on-site excitation of the chiral edge states in the linear regime as well as their remote excitation via instantaneous chiral symmetry breaking induced by nonlinear waves in the nonlinear regime.

3.2.1   Edge states in the linear lattice

According to the classifying table 1.1 of the preceded section 1.7, the 1D Quantum walk described in the effective stroboscopic Floquet picture (with doubled temporal period) belongs to the chiral BDI class of topological insulators, which also comprises the canonical SSH lattice. Moreover, we found out that the parametric extension of the 1D walk treated in the Floquet stroboscopic picture also belongs to the chiral BDI class, if the height of the periodic phase potential parametrized by φ takes value 0 or $\pi/2$, while the periodically alternating coupling coefficients θ_1 and θ_2 can take any values. According to the classifying table, the topological order protected by chiral symmetry corresponds to two integer topological invariants (winding numbers) of the Floquet system. The doubling of invariants stems from Floquet temporal periodicity of the system [75] and hence from two quasienergy bands doubly gapped at $E = 0$ and $E = \pi/2$. Note, that the canonical SSH model characterized by one integer invariant delivers two bands as well, however they are gapped only at $E = 0$, since the band structure is not periodic in energy.

In accordance with the bulk-edge correspondence principle, the existence of an edge state at $E = 0$ or $E = \pi/2$ is predefined by the topological invariant, associated with the respective band gap. For the 1D insulator, this is the winding number, which can be calculated using the above demonstrated chiral reference time frame. This method has been originally proposed in [62]. However, in our study [B2] we used other, more heuristic, methods to correctly predict the number of edge states. One of them is visual, proposed and implemented in [186],[80],[155], and based on the number of band closings on the phase diagram (see Fig. 2(d) of [B2]). In another method, we calculate the winding number of a Floquet-Bloch eigenmode $|k\rangle$, belonging to one of the bands (e.g. with positive energy). Periodic evolution in the infinite bulk can be equivalently described in one of the two "natural" time frames with the evolution operator $\hat{U} = \hat{S}\hat{C}(\theta_2)\hat{S}\hat{C}(\theta_1)$ or $\hat{U} = \hat{S}\hat{C}(\theta_1)\hat{S}\hat{C}(\theta_2)$. Hence, two independent winding numbers W_{12} and W_{21} can be calculated in one and another time frame, respectively. Once the bulk is terminated by setting θ_1 or θ_2 to $\pi/2$ at an odd or even position n (see Figs.3.15a,b), a reflecting edge is introduced and therefore one is allowed to choose only that time frame, that could consistently incorporate the respective lattice termination (see Supplementary material of [B2] for more details). Indeed, in Fig.3.15a (Fig. 3.15(b)) one would have to start the stroboscopic evolution with $\hat{C}(\theta_1)$ ($\hat{C}(\theta_2)$), since otherwise one of the pseudospin components at the edge position will remain unpaired within the bulk. Hence, the respective winding number should be able to correctly predict the number of edge states, that
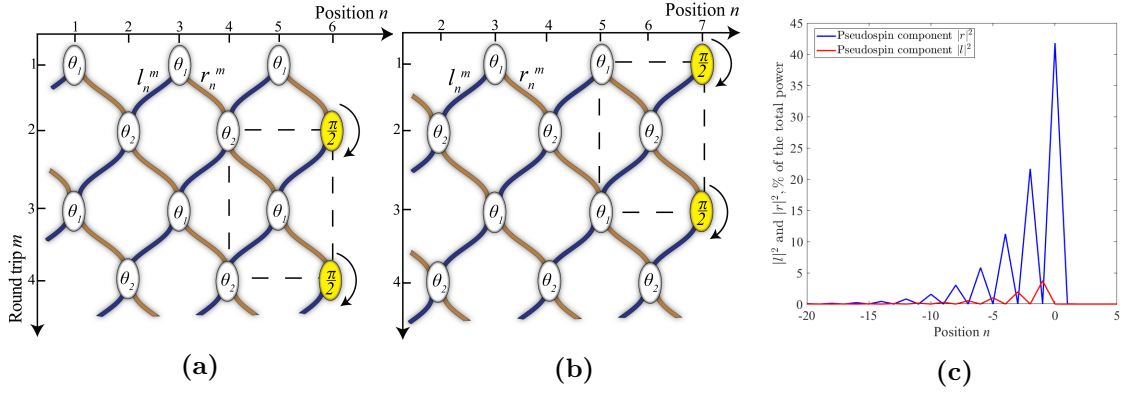
Figure 3.15: (a,b) The periodic Floquet lattice with alternating hopping between one and another sublattices can be terminated either at an odd (b) or even (a) position, by setting the outermost beam splitters at the edge to full reflection. No light can propagate beyond the edge. The dashed rectangle designates elementary unit cell of the respective terminated lattice. The coupling strength parameters $\theta_{1,2}$ are periodically alternating not only in space (as hoping rates of electrons in the canonical SSH model), but are also staggered in time (the distinguishing feature of the Floquet model).(c) Typical edge state profile, having a strong amplitude asymmetry between pseudospin components. The exponentially decaying tale is a characteristic of 1D chiral edge states, however SSH edge states in contrast occupy only one pseudospin component per unit cell, thus hindering any particle motion within the state.

might appear once that particular lattice cut (at θ_1 or θ_2) is implemented. In other words, the respective winding number is associated with one of the two constituent sublattices, that may host a topological edge state.

These winding numbers W_{12} and W_{21}, however, do not show directly the number of edge states in each band gap $N_{E=0}$ and $N_{E=\pi/2}$, since from the beginning we do not use the chiral reference time frames. Instead, the "correctly" chosen winding number shows the difference $N_{E=0} - N_{E=\pi/2}$, and thus the bulk-edge principle has a form of the index theorem [187],[157]. Later on, without loss of generality, we fix θ_1 to $\pi/4$, since according to the phase diagram depicted in Fig. 2(d) of [B2] the bulk can have all possible topological phases while θ_2 sweeps from $-\pi$ to π. The chiral BDI classification for the Floquet lattice predicts two integer topological invariants $\mathbf{Z} \times \mathbf{Z}$, i.e. the winding numbers can in principle take any integer value. Indeed, using the definition

$$W = \frac{1}{\pi} \int_{-\pi/2}^{\pi/2} \left(a_x \frac{\partial a_y}{\partial k} - a_y \frac{\partial a_x}{\partial k} \right) dk, \tag{3.7}$$

where $\vec{a}(k) = a_x(k)\vec{e}_x + a_y(k)\vec{e}_y$ is the pseudospin eigenvector of a fixed band, mapped on the Bloch sphere[4] and sweeping over the first Brillouine zone $k \in (-\pi/2, \pi/2)$, we calculate

$$W_{12} = \begin{cases} 1, & \text{if } \theta_2 \in (-\pi, -3\pi/4) \cup (-\pi/4, \pi/4) \cup (3\pi/4, \pi), \\ 0, & \text{otherwise} \end{cases} \tag{3.8}$$

---

[4]Note, that a_z can be always made zero by an appropriate rotation of the Bloch sphere, because the Hamiltonian obeys chiral symmetry (see [188] and Supplementary Material of [B2] for details).

$$
W_{21} = \begin{cases} 1, & \text{if } \theta_2 \in (\pi/4, 3\pi/4), \\ -1, & \text{if } \theta_2 \in (-3\pi/4, -\pi/4), . \\ 0, & \text{otherwise} \end{cases} \tag{3.9}
$$

This result shows explicitly that the winding numbers are not binary topological invariants $\mathbb{Z}_2$. In light of the fact that W shows only the difference between the number of edge states in each gap, $W = 0$ could mean that none of the gaps support an egde state or that each gap supports one edge state. To resolve this ambiguity, we had to numerically calculate the band structures of finite lattices with different types of termination and values of θ_2. Results of these calculations are presented in the Table 3.1, further below.

Type of lattice termination	Corresponding bulk invariant	$\theta_2 \in$	W	$(N_{E=0}, N_{E=\pi/2})$
At the even position n_{edge}	W_{12}	$(-\pi, -\frac{3\pi}{4}) \cup (\frac{3\pi}{4}, \pi)$	1	(0,1)
		$(-\frac{3\pi}{4}, -\frac{\pi}{4})$	0	(1,1)
		$(-\frac{\pi}{4}, \frac{\pi}{4})$	1	(0,1)
		$(\frac{\pi}{4}, \frac{3\pi}{4})$	0	(0,0)
At the odd position n_{edge}	W_{21}	$(-\pi, -\frac{3\pi}{4}) \cup (\frac{3\pi}{4}, \pi)$	0	(0,0)
		$(-\frac{3\pi}{4}, -\frac{\pi}{4})$	-1	(1,0)
		$(-\frac{\pi}{4}, \frac{\pi}{4})$	0	(0,0)
		$(\frac{\pi}{4}, \frac{3\pi}{4})$	1	(0,1)

Table 3.1: Bulk-edge correspondence for the Floquet SSH-like model.

We see that whenever W_{12} is zero, W_{21} is non-zero and vice versa, implying that if one sublattice, associated with a particular type of edge, supports an edge state, another one does not. The exclusion is only in the range $\theta_2 \in (-3\pi/4, -\pi/4)$, where despite the triviality of the first sublattice (termination at an even position, $W_{12} = 0$) it still hosts a pair of edge states, one in each band gap. This situation is a direct consequence of Floquet periodicity of the band structure and can be referred to as Floquet anomalous topological insulator. In our recent experimental work [B1], we investigate this case for anomalous interface states by applying a phase modulation of pulses in the coupled fiber loop set-up. The applied phase potential allowed us to effectively extend the parametric range of coupling coefficients to negative values and hence to observe the coexisting pair of localized states. In contrast, our experiments in [B2] were limited to the parametric range $0 < \theta < \pi/2$, therefore only the edge state at $E = \pi/2$ could be experimentally accessible there.

A typical edge state profile is illustrated in Fig. 3.15c. One can see that the amplitude profile is localized and its tale decays exponentially inside the bulk, i.e. $|l|_n^2 = |l|_{n_{\text{edge}}}^2 \exp(-n/\xi)$ and $|r|_n^2 = |r|_{n_{\text{edge}}}^2 \exp(-n/\xi)$, where n_{edge} is the edge position and ξ is by definition a localization length of the edge mode. Such an exponential decay is a well-known characteristic of chiral edge states, in particular of these occurring in the canonical SSH model. Moreover, it is known that in the SSH dimeric chain the localization length varies depending on the intracell r and intercell t electron hopping rates as $\xi = 1/\log |t/r|$ [189]. For our system, we figured out numerically that 1) localization lengths in both sublattices (edge types) follow analogous inverse logarithmic laws $\xi \approx \alpha + \beta/\log |\cot(\theta_2)|$ 2) these laws are quantitatively different as they depend on the sublattice (the edge type) as well as on quasienergy of the edge mode itself ($E = 0$ or $E = \pi/2$). For example, the first sublattice at $\theta_2 \in (-\pi/4, \pi/4)$ hosts one edge mode at $E = \pi/2$ with $\xi \approx 1.9 + 2.83/\log(|\cot(\theta_2)|)$, while the other sublattice at $\theta_2 \in (\pi/4, 3\pi/4)$ supports one edge mode at $E = \pi/2$ with $\xi \approx 0.2 + 2.82/\log(|\cot(\theta_2)|)$.
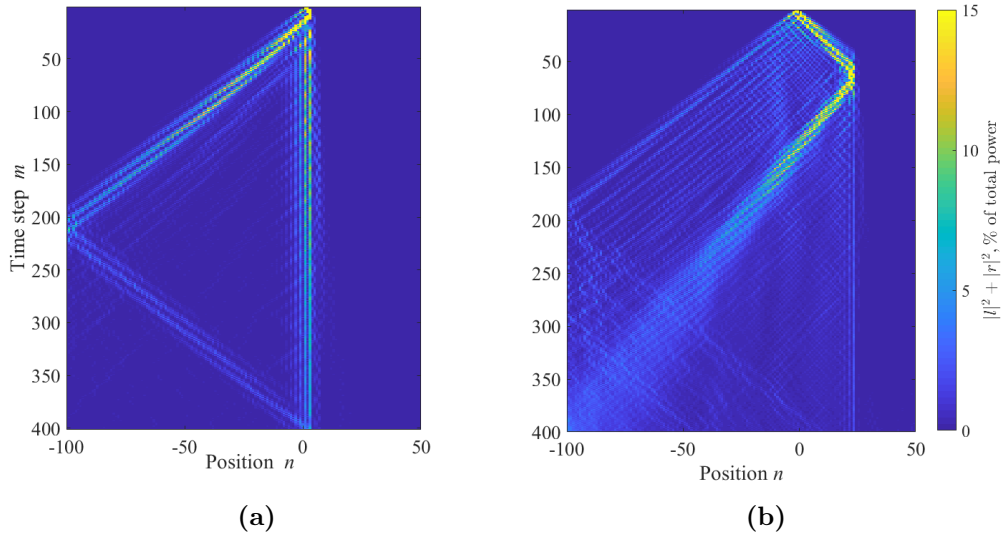
Figure 3.16: (a) Experimental on-site excitation of the linear edge state at $\theta_1 \approx 0.25\pi$, $\theta_2 \approx 0.32\pi$. A coherent trapping of light has been observed for more than 400 time steps. Due to a limited size of the lattice, the mobile wave travelling to the left side gets reflected backwards, but is irrelevant for the edge state excitation. (b) Remote excitation of an edge state at $\theta_1 \approx 0.25\pi$, $\theta_2 \approx 0.3\pi$ with a chiral symmetry breaking nonlinear wave. Power of the input pulse was finely adjusted, in order to spectrally match the edge state with bulk modes and thus to maximize the excitation efficiency (in this configuration, about 6% of the input power).

Note, that the former mode has a finite minimum localization length of 1.9 positions at $\theta_2 = 0$, corresponding to the splitting ratio 100/0 for each even beam splitter. On the other hand, for the latter edge mode we formally get the minimum of $\xi = 0.2$ at $\theta_2 = \pi/2$, however the exponential fitting model does not work exactly in this highly localized limit, because in fact beam splitters located at even positions are set to full reflection (0/100), implying that the edge state is confined within one single pseudospin and therefore its amplitude profile has an abrupt delta-like shape. Finally, it is worth mentioning that in contrast to the canonical SSH edge states, where π-orbitals of only every second carbon atom are occupied [163] and therefore any motion of an electron along the chain is suppressed within the edge state, in our Floquet model both pseudospin components l and r within a unit cell are non-zero, although one of them typically dominates, indicating a strong chirality of the edge state. As a consequence, such a state with all non-zero pseudospin components supports a certain internal light dynamics within itself. This is in accordance with the temporal periodic Floquet drive, physically associated with zigzag wiggling of the coupled waveguides, forming the spatiotemporal lattice.

To conclude this section, we will provide some experimental details on the linear on-site excitation of the edge state at $E = \pi/2$, as follows from [B2]. As already mentioned, because of the fixed relative phase $\pi/2$ between the transmission t and reflection ir ports of the dynamical variable coupler used in the experiments, the coefficients $\theta_{1,2}$ had to be restricted to the range from 0 to $\pi/2$. A topological edge state has been excited in the linear regime by launching a single optical pulse into one of the loops, which corresponds to a delta-like signal. If the injected pulse is far away from the edge position n_{edge}, then mostly extended bulk modes over the entire Brilloine zone become excited in the lattice. If, however, the pulse significantly overlaps with the edge mode profile or in the best case it is exactly at n_{edge}, then a great amount of the injected power (up to 30% with the delta-

like excitation) gets trapped within the mid-gap edge mode. The rest of the light power, in turn, gets distributed between free propagating bulk modes. In the experiments, we could observe a coherent and robust field localization within the edge state for more than 400 round trips (see Fig. 3.16a and Fig. 3g of [B2]). Experimental imperfections are mainly due to inevitable acoustic and other environmental perturbations, hindering interferometric stability of the walk, as well as due to a certain gain/loss disbalance between pulses amplified in the short and in the long loop, stemming from a strong pseudospin asymmetry in the edge state amplitude profile. The latter, as one can see in the Fig. 3.16a, leads to a continuous light radiation from the edge state into the bulk. Moreover, a limited extinction ratio and modulation bandwidth of the voltage-driven variable coupler do not allow to set a perfect (100 percent) pulse reflection at the edge position, thus leading to a visible power "leakage" beyond the boundary (see Fig. 3.16a). Nevertheless, the light trapped within the edge state could be evidently decoupled from the free-propagating waves and remain localized for at least 400 round trips and even longer.

3.2.2   Edge states in the Kerr nonlinear regime

The last section is devoted to adaptation of the chiral topological mid-gap edge states to on-site instantaneous nonlinearities, mathematically described by the operator (3.1) and physically stemming from nonlinear Kerr effect and resulted self-phase modulation of the pulses, circulating through dispersion-compensating fibers, that are incorporated in both long and short loops of the set-up.

Due to the previously mentioned strong pseudospin asymmetry of a typical edge state profile, each unit cell covered by the edge state would acquire an asymmetric nonlinearity-induced phase potential, according to eq. (3.1). Such phase potentials would inevitably break chiral symmetry of the respective unit cells (for details, see Supplementary Material of [B2]). As a result, the local symmetry breaking should lead to a broken topological protection of the mid-gap state, thus lifting it up energetically towards one of the bulk bands. Nevertheless, as it was earlier shown for the tight-binding Bose-Hubbard model in [172], topological order of the underlying linear system may still be preserved and the adopted nonlinear edge state may still be considered as conditionally robust up to a moderate level of nonlinearity strength. Further on, we verify these observations numerically for the Floguet edge states .

First, in order to trace out the nonlinear edge state solutions, we use the standard self-consistency iterative method, used earlier in this thesis for solitonic solutions. Namely, we start with the linear edge state solution, which is valid in the linear limit $P \to 0$, where P is the total power of the state, and stepwise increase the power, meanwhile letting the state adopt to the every new level of nonlinearity strength. The nonlinear coefficient γ is fixed to +1 throughout the optimization. Chosen lattice size is 200 positions. As anticipated from chiral symmetry breaking, the state starts to leave its mid-gapped position $E = -\pi/2$. We illustrate this with two concrete examples in Figs. 3.17a,b, which are the "broad" edge state at $\theta_1 > \theta_2$ (lattice termination at the even coupler θ_2) and the "narrow" edge state at $\theta_1 > \theta_2$ (lattice termination at the odd coupler θ_1). Note, that the band gap size at $E = -\pi/2$ is the same in both cases, being equal to $\Delta E = 0.3\pi$. On the other hand, the size of the trivial gap around $E = 0$ as well as spectral width of both bands are not the same in one and another lattice configuration. Indeed, we see that quasienergies of both nonlinear edge states first grow linearly with total power, but later they start to saturate in a quadratic manner until their total powers reach corresponding critical values and the states encounter the upper bulk band. As illustrated in Fig. 3.17a, the amplitude profiles remain almost the
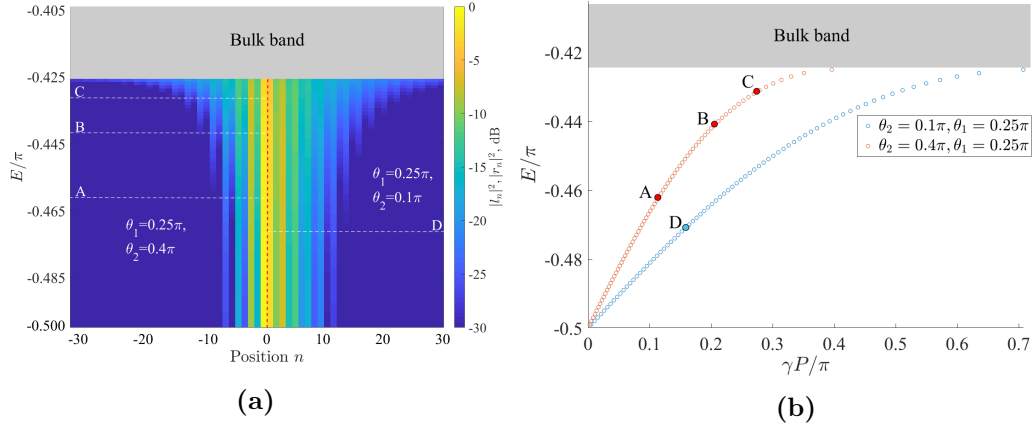
Figure 3.17: (a) Spatial amplitude profiles of the nonlinear steady-state "narrow" edge (left side, termination at odd couplers as shown in Fig. 3.15b) and "broad" edge solutions (right side, termination at even couplers as shown in Fig. 3.15a) versus the propagation constant E. The logarithmic scale is chosen for a better visibility. The pseudospin components l and r are stacked one after another in the plot, so that pseudospin asymmetry within each unit cell is visible as well. Dashed lines mark instability thresholds discussed in the text. (b) Total powers of the "narrow" (red circles, $\theta_2 = 0.4\pi, \theta_1 = 0.25\pi$) and "broad" (blue circles, $\theta_2 = 0.1\pi, \theta_1 = 0.25\pi$) nonlinear edge states versus the propagation constant E.

same up respective moderate levels of nonlinearity strength (points A and D), but later the profile's changes become visible in the logarithmic scale, and closer to the upper band the states quickly broaden until they finally disperse into the bulk. Further on, we will interpret these moderate levels as instability thresholds for the edge states.

As already mentioned above, previous studies on tight binding-models with on-site and nearest-neighbour Hubbard interactions typically display a robust topological order at a low or even moderate level of interaction strength. As known from nonlinear optics, instability thresholds in Kerr nonlinear media typically trigger non-reciprocal parametric processes and lead to instabilities of solitonic solutions. To verify this numerically for the nonlinear Floquet edge states, we perform the standard stability analysis by linearizing the following discrete evolution equations around the "broad" or "narrow" nonlinear solution $|\psi\rangle_E$ with varying propagation constant E

$$\hat{U}(\theta_1, \theta_2)\hat{K}\Big(|\psi\rangle_E + |\alpha\rangle_{E,\Omega} + |\beta\rangle_{E,-\Omega} \Big) = e^{iE}\Big(|\psi\rangle_E + |\alpha\rangle_{E,\Omega}\, e^{i\Omega} + |\beta\rangle_{E,-\Omega}\, e^{-i\Omega} \Big), \quad (3.10)$$

where $|\alpha\rangle$ and $|\beta\rangle$ are small-amplitude perturbation terms, propagating, respectively, forward and backward in time, $\pm\Omega$ are respective eigenenergies of these terms, $\hat{U}(\theta_1, \theta_2)$ is the linear Floquet evolution operator and $\hat{K}$ is the Kerr nonlinear phase shifter, given by the expression (3.1). After the standard linearization procedure, one can numerically solve the resulted eigenvalue problem and obtain stability spectrum, as shown in Figs. 3.18 and 3.19 for the "broad" and "narrow" edge states, respectively. One can see, that the spectra contain linear bulk modes (green dots) with mainly real-valued Ωs. Small imaginary parts of the Ωs in the right side plots are not generic, since they can be arbitrarily suppressed by increasing the numerical size of the lattice. In addition, both spectra contain the linear topological mid-gap state (red dots), which however gets shifted from the mid-gap position in the reference frame of the nonlinear edge state. Another similarity between stability spectra of the "broad" and "narrow" edge states is the presence of so-called "Goldstone" mode at $\Omega = 0$ (blue dots),

95

which is associated with phase symmetry of the steady-state solution.

Now, we turn our attention to instabilities of the edge states, which are triggered at $E_{\theta_2=0.1\pi} \approx -0.467\pi$ (point D) and $E_{\theta_2=0.4\pi} \approx -0.462\pi$ (point A) by another nonlinear localized formation (black dots in Figs. 3.18 and 3.19), which bifurcates from bulk modes of the upper band into another (originally topologically trivial) band gap around $E = 0$. These formations are unbounded due to the non-zero imaginary part of Ω. Therefore, they can grow on the cost of the respective nonlinear edge states, thus destabilizing them. Here, we do not specify the parametric processes and related phase matching conditions that eventually lead to the edge state instability. Instead, we note that the triggered nonlinear interactions between defect states in the originally (in the linear limit) trivial and non-trivial gap should alter topological order of the underlying system. Indeed, if one would formally apply the earlier found bulk-boundary correspondence principle $W = N_{E=0} - N_{E=\pi/2}$, one would get 0 instead of 1, thus implying a topological transition [5] Provided this argumentation is valid, linear stability of the edge state and its weakly modified amplitude profile (except a global power scaling) can be associated with a robust topological order, although topological protection in terms of the mid-gapped spectral position is lost in a strict sense at any level of nonlinearity strength. Another indication of validity of the index theorem is that the "narrow" edge state becomes stable additionally in the strongly nonlinear regime (between points B and C), once the gap nonlinear formation undergoes a bifurcation into two bounded oscillating solutions (see Fig. 3.19). As a result, the topological invariant becomes now $N_{E=0} - N_{E=\pi/2} = 2 - 1 = 1$, indicating the return to the non-trivial topology. Although for a direct proof of the bulk-boundary correspondence principle one would have to construct a proper topological invariant, it is nevertheless clear already from the above reasoning that: 1) the definition of a robust topological order in the nonlinear regime has to be extended to not exactly mid-gap defect states, preserving their amplitude profiles; 2) the anticipated topological transition or even a complete change of the topological order above the instability threshold is not associated with an ultimate destruction of the edge state, but instead leads to its instability, triggered by non-reciprocal interactions with the defect state in another gap. In [B2] we show that such an unstable edge state is in fact self-stabilizing, as it eventually radiates its excess power into the bulk until its total power drops below the instability threshold. It is worth mentioning that in the SSH model with nearest-neighbour interactions, a similar self-recovering behaviour of a nonlinear edge state was observed [190], however the state there was "repelling" from a trivial topology by keeping its total power above the instability threshold. Finally, we note that since the presence of two band gaps is a feature of the Floquet model, one can not expect the same type of edge state instability in the canonical SSH model. Our preliminary stability analysis shows that SSH edge states are unstable at any level of local Kerr nonlinearity strength, in contrast to the Floquet edge states. However, further details of that phenomenon go beyond the scope of the thesis.

Concluding current section on nonlinear edge states, we demonstrate the possibility of a remote excitation of an otherwise topologically protected edge state by means of an impinging nonlinear wave, which is able to locally break chiral symmetry of the linear lattice and thus to temporarily lift up the edge state from its mid-gap position towards one of the bulk bands. The effect has been demonstrated experimentally in the coupled fiber loop set-up and results have been published in [B2]. More specifically, there we launch a single pulse into one of the loops at a substantial distance from the edge site n_{edge}, so that the spatial overlap of the input signal with the edge mode is negligible. The pulse excites the entire

---

[5]Note that the topological invariant W can not be defined here as the winding number given by eq. (3.7), since transverse invariance of the lattice is broken in the nonlinear regime.
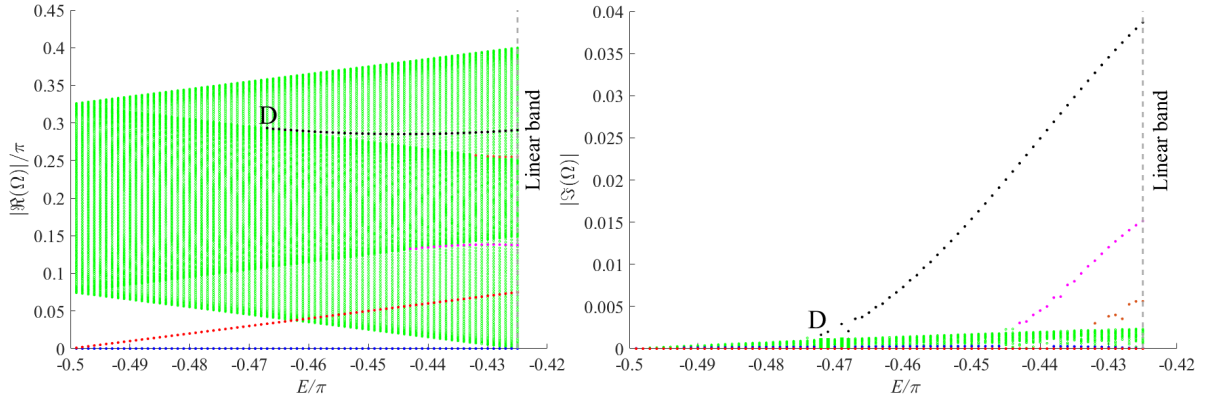
Figure 3.18: Real (left) and imaginary (right) components of the linearized spectrum of perturbations around the "broad" edge state at $\theta_2 = 0.1\pi$, containing linear bands (green), the linear topological edge state (red), the zero-energy "Goldstone" mode (blue) and the unbounded nonlinear formation (black). The latter triggers instability at the point D.
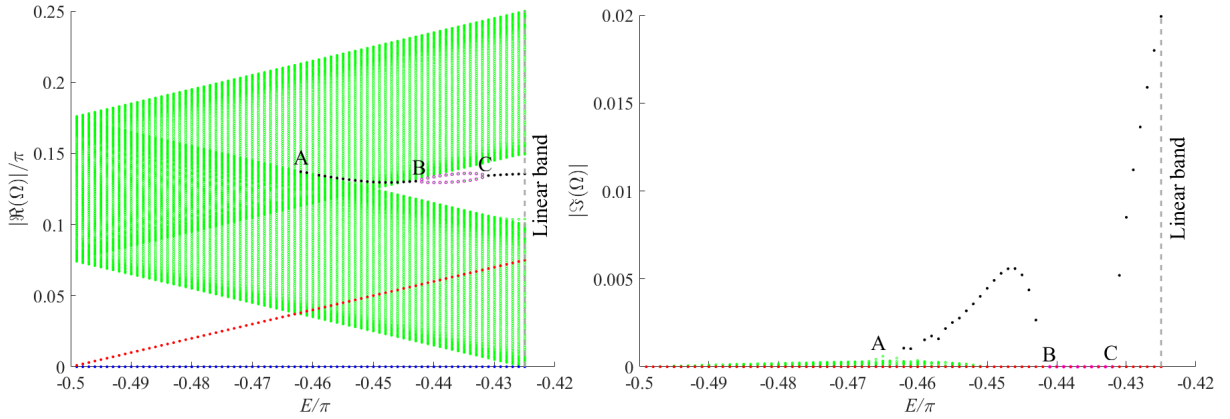

Figure 3.19: Real (left) and imaginary (right) components of the linearized spectrum of perturbations around the "narrow" edge state at $\theta_2 = 0.4\pi$, containing linear bands (green), the linear topological edge state (red), the zero-energy "Goldstone" mode (blue) and the unbounded nonlinear formation (black). The latter triggers instability at the point A. The nonlinear formation bifurcates in two bounded oscillating solutions (magenta) between points B and C.

band structure of the bulk and the majority of the excited waves are heading then towards the edge. The edge state however, being topologically protected in the linear regime, can not acquire any power from the impinging waves, so that all of them get simply reflected at the edge. On the other hand, the situation changes drastically if the amplitude of the input pulse is tuned up, thus entering Kerr nonlinear regime. The otherwise non-interacting waves form now a propagating nonlinear wave, which is precursor for a discrete gap soliton [10, 11]. The nonlinear wave propagates towards the edge without changing considerably its shape. Once the nonlinear wave reaches the edge, it breaks chiral symmetry of the unit cells covered by the edge state, thus lifting it spectrally from the mid-gap position towards one of the bands. Provided the input pulse power is finely tuned, the edge state can be brought in resonance with some of the bulk modes and thus it can couple some light power out of them, as illustrated experimentally in Fig. 3.16b. Once the nonlinear wave gets reflected, the chiral symmetry in the vicinity of the edge becomes again recovered and the edge state returns to its mid-gap position, but now with some light trapped within. For the given excitation scheme, the amount of trapped light does not exceed 6% and 3% in the lattice terminated at odd and

even time steps, respectively. This relatively low transfer efficiency is close to theoretical estimations as it mainly owns to the demanding phase matching condition, which has to be satisfied for both quasimomenta and quasienergies. Therefore, a certain optimization of the initial field distribution with regard to these requirements could noticeably increase the transfer efficiency. Nevertheless, the nonlinear pumping of the edge state has been detected experimentally even with the delta-like initial distribution. Due to a gradually increasing level of phase decoherence in the experimental set-up [11], the nonlinear waves get dissolved after around 150 time steps. On the other hand, once excited the edge state is able to coherently trap the light for more than 400 time steps.

Chapter 4

Summary and outlook

4.1 Summary

In conclusion, this thesis is devoted to novel nonlinear effects in time-multiplexed 1D and 2D Discrete Quantum Walks, studied both theoretically and experimentally in the classical regime. In the opening chapter "Theoretical background", we gave a broad description of linear walks based on 2×2 beam splitters, including one 2D network, which is not amenable to an interferometrically stable time-multiplexing. The linear dynamics was thoroughly described in the framework of periodic Floquet-Bloch waves, known from Solid State Physics. In addition, we extended the description towards networks with periodic potentials and periodic coupling strengths. Both degrees of freedom were found to introduce continuous dispersion shaping as well as band gap splitting effects, while specifically decoupled network knots also resulted in a reduced dimensionality and effectively in a flat band dispersion.

Based on local and global symmetries of the lattices and using the notion of the instantaneous and stroboscopic (Floquet) pictures, we could give an exhaustive classification of the walks among other non-interacting topological insulators. Remarkably, the time-multiplexed 1D and 2D and the interferometrically nonamenable 2D walks had fundamentally different underlying symmetries and topological properties. So, for example, the nonamenable 2D walk always belongs to one of the chiral insulator class (A, AI or BDI) with a boson-like pseudspin and robust achiral properties of the network, while the time-multiplexed walks in addition cover Bogoliubov-de Gennes classes (D, DIII), typical for fermionic systems, such as superconductors. Thus, the two-component pseudospin features a certain boson-fermion duality, what eventually might be a key reason, why correlated photons can exhibit both quantum statistics in the same quantum walk [37, 41]. The stroboscopic picture was expectedly found to be generally less "sensitive" to "temporally microscopic" symmetry breakings, compared to the instantaneous picture. As a result, several classes in the instantaneous picture could be unified into one chiral class in the stroboscopic picture. The last section of "Theoretical background" is devoted to the pseudo-Hermitian framework of parity-time symmetric complex potential. For all time-multiplexed walks, we could find recovered parity-time symmetry phases with real-valued eigenenergies. Also, some exotic cases of 1D networks with twisted ports and coupled sublattices were considered.

The next chapter "Time-multiplexed fiber loop set-ups" is devoted to technical details of the time-multiplexing techniques. For the 1D fiber loop set-up, we gave only a brief description as the most of the set-up features has been already extensively covered by my supervisor Martin Wimmer in his previous works. The 2D fiber loop set-up is to a large extend based on its one-dimensional counterpart and therefore only technical difficulties related specifically to the extended dimensionality are mentioned. All in all, a coherent

propagation over 100 time steps could be successfully implemented in 2D.

The final core element of the thesis concerns discrete 1D and 2D solitons in pseudo-Hermitian parity-time symmetric environments and 1D topological edge states in the presence of local Kerr nonlinearity. In this part, we concentrated on time-multiplexed networks, since these are only experimentally realizable within our framework configurations. The experiments on 2D solitons were implemented in our group by Andre Muniz and Martin Wimmer, while 1D topological edge states were experimentally realized by the author of the thesis. In the beginning of the chapter, we reproduced basic theoretical results on 1D solitons previously obtained in [99]. In addition, we numerically investigated the phenomenon of super-exponential "blow-up" of solitons in the parity-time symmetric potential. Remarkably, although the solitons generically are not conservative, their average lifetimes, defined as the number of time steps until blow-up and depending on the "blow-up" power threshold, follow the celebrated Bose-Einstein statistics, provided the parity-time symmetry is not recovered. Moreover, if the parity-time symmetry is recovered, the lifetime distribution follows a quadratic Bose-Einstein statistics, which significantly enhances solitonic lifetimes at small enough gain/loss parameters. This lifetime enhancement effect of $\mathcal{PT}$ phase recovery has been discovered for the first time.

Regarding the 2D discrete solitons, we achieved a considerable understanding of the inherently two-dimensional and discrete phenomenon of nonlinear quasi-collapse, which has been observed experimentally in a conservative lattice in [B4]. Although numerical data revealed at least two post-collapse highly-localized solutions (steady-state and oscillating) with slightly different powers and extremely long propagation times, in the experiment we could observe only the steady-state solution after quasi-collapse. Further on, we studied numerically the non-Hermitian blow-up in the parity-time symmetric environment and, just as for 1D solitons, we similarly observed Bose-Einstein and enhanced quadratic Bose-Einstein statistics of lifetimes for the 2D solitons. We partly attribute this similarity to the quasi-1D configuration of the recovering real part of the $\mathcal{PT}$ potential and therefore it would be tempting to study a genuine 2D $\mathcal{PT}$-symmetric potential as well. If possible at all, such configuration would require an even more extended size of the elementary unit cell of the 2D lattice. Finally, we merged the two phenomena of 2D discrete quasi-collapse and non-Hermitian blow-up and determined several non-trivial connections between them. First of all, the quasi-collapse event is usually accompanied with the "exothermic" blow-up, while the alternative scenario of soliton's broadening, typical for small adiabatic gain/loss amplitudes, has been found associated with the "endothermic" blow-up. Interestingly, the intermediate finely tuned scenario, when the quasi-collapse takes place without any power blow-up, was found as well, indicating that the blow-up and quasi-collapse are inherently distinct phenomena with different underlying mechanisms. The non-conservative blow-ups boost the momentum of resulted nonlinear formations in one or another direction and we provided some heuristic explanations of these effects for both "endothermic" and "exothermic" cases.

Finally, we investigated chiral topological edge states in the 1D Discrete Quantum Walk with periodically variable coupling, which is based on the celebrated 1D Su-Schrieffer-Heeger (SSH) chain model and which, in the stroboscopic picture, belongs to the BDI chiral class of topological insulators. We discovered, that the variable coupling along with non-trivial topology also introduces Floquet periodicity to the lattice, which in turn results in two distinct band gaps and two topological invariants, in accordance with theory [75]. Further implication of this doubling is that the Floquet lattice, in contrast to the SSH chain, can be terminated in two different ways and thus two physically distinct edge states can exist, residing on one or another sublattice. Deriving the topological winding numbers for different

topological phases and comparing them with the number of edge states in each gap, we could establish an incomplete bulk-edge correspondence relation in the form of the index theorem. Despite the Floquet "duality" of the lattice, the topological edge states possess exponentially decaying tales and localization lengths, which behave similarly to those of the edge states in the canonical 1D SSH model. Due to previously mentioned experimental limitations met in [B2], we had to restrict ourselves to the edge state hosted at $E = \pi/2$, but not at $E = 0$. In that regard, a linear propagation of the edge state has been successfully measured for more than 400 time steps. A possibility for anomalous Floquet interface states in the fiber loop set-up has been briefly discussed in the thesis and demonstrated in our recent work [B1].

Next, in accordance with previous studies of bosonic and fermionic topological insulators with local and nearest-neighbour interactions, we could numerically reassure that Floquet chiral edge states can adopt to Kerr nonlinear regime, while remaining stable and hardly changing their amplitude profiles up to a moderate level of Kerr nonlinearity. We argued that nonlinear system below the instability threshold can be considered as preserving the topological order of the underlying linear system, despite topological protection in a sense of the mid-gap position is lost strictly speaking. In addition, we found out that one of the two edge state types can become stable even within the power range with high levels of nonlinearity, presumably designating recovered topological order of the underlying linear system. Last, but not least, we could for the first time observe a finely tuned nonlinearity-induced pumping of the topological state, based on the effect of local chiral symmetry breaking. Although the amount of trapped light was relatively small due to mismatched phase conditions, a coherent edge state localization has been observed for more than 400 time steps.

4.2 Outlook

The variety of concepts involved in this thesis (topology, discreteness, pseudo-Hermiticity, nonlinearity) naturally provide a rich playground for potential extensions in both theoretical and experimental directions. Here, I would like to list only several ideas and aspirations, which in one or another way popped up during my research, but had not been yet realized either completely or halfway.

1. In the 2D time-multiplexed walk, one can observe the celebrated Bloch oscillations, which in two dimensions follow trajectories similar to Lissajous curves. In the context of the fascinating phenomenon of unidirectional Bloch oscillations in parity-time symmetric systems [191], it is even more tempting to extend the preceding experimental results on 1D $\mathcal{PT}$-symmetric photonic lattices [83, 84] towards two dimensions.

2. A mathematical equivalence of the nonlinear 2D Schrödinger equation, approximately holding for extended field distributions in the time-multiplexed 2D Quantum Walk, and the so-called Gross-Pitaevsky equation, describing Bose-Einstein condensation of a dilute gas in the mean-field approximation [10], provides a practical experimental ground for studying thermalization process, Bose condensation of light in a trap, Kosterlitz-Thouless transition with vortex-antivortex pair annihilation [3–5] and even Kibble-Zurek quenching mechanism [192, 193], if the available trap is large enough. However, due to a limited number of propagation time steps, such statistical processes have to be sufficiently optimized for the experiment. In particular, when it comes to Bose condensation, one should sufficiently minimize the trap size, keep the effective mass of particles small enough, introduce a faster cooling and a stronger nonlinearity level.

3. Another direction to go is conceptually very different from all the project tackled in the thesis, as the framework of a single particle quantum walk is not enough for that. Namely, the idea of time-multiplexing clearly works on the quantum level for single photons [33, 46, 96]. Therefore, the next natural step in the quantum regime would be extending the walk to two spatially correlated or even entangled photons. One idea, for example, within the topological framework could be demonstrating a topologically protected bunching-antibunching conversion of a correlated two-photon state [194]. This path is however accompanied with many technical difficulties, such as considerable photon losses, low coincidence-to-accidentals ratio, quantum decoherence, etc.

4. Topological edge states can be also experimentally studied in the two-dimensional time-multiplexed set-up. As shown in the thesis [188] of our former master student Mark Kremer, vertical and horizontal edges of the two-dimensional lattice can indeed support mobile localized states, topologically protected by the so-called Chern number.

5. Finally, the interferometrically nonamenable 2D walk with a robust network "achirality" and boson-like pseudospin remained completely unexplored from the experimental side. Possible realizations based on counter-propagating directions [49] or additionally involved polarization degree of freedom [50] could be feasible. This network is interesting already in the linear regime with the static periodic potential, because as we demonstrated it has a very peculiar (essential) singularity point, isolated from surrounding eigenmodes and resembling some features of non-Hermitian exceptional points.

Own publications

[B1] **A. Bisianov**, A. Muniz, O. Egorov, and U. Peschel, "Topological floquet interface states in optical fiber loops", Physical Review A, submitted (2020).

[B2] **A. Bisianov**, M. Wimmer, U. Peschel, and O. A. Egorov, "Stability of topologically-protected edge states in nonlinear fiber loops", Phys. Rev. A **100**, 063830 (2019).

[B3] A. L. M. Muniz, M. Wimmer, **A. Bisianov**, P. S. Jung, D. N. Christodoulides, R. Morandotti, and U. Peschel, "2D solitons in $\mathcal{PT}$-symmetric photonic lattices", Physical Review Letters, accepted (2019).

[B4] A. L. M. Muniz, M. Wimmer, **A. Bisianov**, R. Morandotti, and U. Peschel, "Collapse on the line: how synthetic dimensions influence nonlinear effects", Scientific Reports **9** (2019).

[B5] Y. Zhang, M. Kues, P. Roztocki, C. Reimer, B. Fischer, B. MacLellan, **A. Bisianov**, U. Peschel, B. E. Little, S. T. Chu, D. J. Moss, L. Caspani, and R. Morandotti, "Induced photon correlations through superposition of two four-wave mixing processes in integrated cavities", submitted (2020).

Bibliography

[1] T. Ozawa, H. M. Price, A. Amo, N. Goldman, M. Hafezi, L. Lu, M. C. Rechtsman, D. Schuster, J. Simon, O. Zilberberg, and I. Carusotto, "Topological photonics", Rev. Mod. Phys. **91**, 015006 (2019).

[2] S. Longhi, "Parity-time symmetry meets photonics: a new twist in non-hermitian optics", EPL (Europhysics Letters) **120**, 64001 (2017).

[3] J. M. Kosterlitz and D. J. Thouless, "Long range order and metastability in two dimensional solids and superfluids. (application of dislocation theory)", Journal of Physics C: Solid State Physics **5**, L124–L126 (1972).

[4] J. M. Kosterlitz and D. J. Thouless, "Ordering, metastability and phase transitions in two-dimensional systems", Journal of Physics C: Solid State Physics **6**, 1181–1203 (1973).

[5] V. L. Berezinsky, "Destruction of long range order in one-dimensional and two-dimensional systems having a continuous symmetry group. I. Classical systems", Sov. Phys. JETP **32**, 493–500 (1971).

[6] K. von Klitzing, "The quantized hall effect", Rev. Mod. Phys. **58**, 519–531 (1986).

[7] K. v. Klitzing, G. Dorda, and M. Pepper, "New method for high-accuracy determination of the fine-structure constant based on quantized hall resistance", Phys. Rev. Lett. **45**, 494–497 (1980).

[8] C. M. Bender and S. Boettcher, "Real spectra in non-hermitian hamiltonians having $\mathcal{PT}$-symmetry", Phys. Rev. Lett. **80**, 5243–5246 (1998).

[9] C. M. Bender, "Making sense of non-hermitian hamiltonians", Reports on Progress in Physics **70**, 947–1018 (2007).

[10] M. Wimmer, "Experiments on photonic mesh lattices", Doctoral Thesis (Friedrich-Alexander-Universität Erlangen-Nürnberg (FAU), Jan. 2018).

[11] M. Wimmer, "Nichtlineare pulsausbreitung in einem optischen fasernetzwerk", Master Thesis (Friedrich-Alexander-Universität Erlangen-Nürnberg (FAU), Jan. 2013).

[12] J.-F. Collet, *Discrete stochastic processes and applications*, Universitext (Springer International Publishing, 2018).

[13] J. Kempe, "Quantum random walks: an introductory overview", Contemporary Physics **50**, 339–359 (2009).

[14] F.Benatti and R. Floreanini, *Irreversible quantum dynamics*, Physics (Springer Berlin Heidelberg, 2003).

[15] C. M. Chandrashekar, "Implementing the one-dimensional quantum (hadamard) walk using a bose-einstein condensate", Phys. Rev. A **74**, 032307 (2006).

[16]M. Karski, L. Forster, J.-M. Choi, A. Steffen, W. Alt, D. Meschede, and A. Widera, "Quantum walk in position space with single optically trapped atoms", Science **325**, 174–177 (2009).

[17]G. Summy and S. Wimberger, "Quantum random walk of a bose-einstein condensate in momentum space", Phys. Rev. A **93**, 023638 (2016).

[18]M. Genske, W. Alt, A. Steffen, A. H. Werner, R. F. Werner, D. Meschede, and A. Alberti, "Electric quantum walks with individual atoms", Phys. Rev. Lett. **110**, 190601 (2013).

[19]B. C. Travaglione and G. J. Milburn, "Implementing the quantum random walk", Phys. Rev. A **65**, 032310 (2002).

[20]P. Xue, B. C. Sanders, and D. Leibfried, "Quantum walk on a line for a trapped ion", Phys. Rev. Lett. **103**, 183602 (2009).

[21]H. Schmitz, R. Matjeschk, C. Schneider, J. Glueckert, M. Enderlein, T. Huber, and T. Schaetz, "Quantum walk of a trapped ion in phase space", Phys. Rev. Lett. **103**, 090504 (2009).

[22]F. Zähringer, G. Kirchmair, R. Gerritsma, E. Solano, R. Blatt, and C. F. Roos, "Realization of a quantum walk with one and two trapped ions", Phys. Rev. Lett. **104**, 100503 (2010).

[23]B. C. Sanders, S. D. Bartlett, B. Tregenna, and P. L. Knight, "Quantum quincunx in cavity quantum electrodynamics", Phys. Rev. A **67**, 042305 (2003).

[24]T. Di, M. Hillery, and M. S. Zubairy, "Cavity qed-based quantum walk", Phys. Rev. A **70**, 032304 (2004).

[25]C. A. Ryan, M. Laforest, J. C. Boileau, and R. Laflamme, "Experimental implementation of a discrete-time quantum random walk on an nmr quantum-information processor", Phys. Rev. A **72**, 062317 (2005).

[26]J. Du, H. Li, X. Xu, M. Shi, J. Wu, X. Zhou, and R. Han, "Experimental implementation of the quantum random-walk algorithm", Phys. Rev. A **67**, 042316 (2003).

[27]D. Bouwmeester, I. Marzoli, G. P. Karman, W. Schleich, and J. P. Woerdman, "Optical galton board", Phys. Rev. A **61**, 013410 (1999).

[28]B. Do, M. L. Stohler, S. Balasubramanian, D. S. Elliott, C. Eash, E. Fischbach, M. A. Fischbach, A. Mills, and B. Zwickl, "Experimental realization of a quantum quincunx by use of linear optical elements", J. Opt. Soc. Am. B **22**, 499–504 (2005).

[29]A. Regensburger, C. Bersch, B. Hinrichs, G. Onishchukov, A. Schreiber, C. Silberhorn, and U. Peschel, "Photon propagation in a discrete fiber network: an interplay of coherence and losses", Phys. Rev. Lett. **107**, 233902 (2011).

[30]H. B. Perets, Y. Lahini, F. Pozzi, M. Sorel, R. Morandotti, and Y. Silberberg, "Realization of quantum walks with negligible decoherence in waveguide lattices", Phys. Rev. Lett. **100**, 170506 (2008).

[31]P. Xue, H. Qin, B. Tang, and B. C. Sanders, "Observation of quasiperiodic dynamics in a one-dimensional quantum walk of single photons in space", New Journal of Physics **16**, 053009 (2014).

[32]F. Cardano, F. Massa, H. Qassim, E. Karimi, S. Slussarenko, D. Paparo, C. de Lisio, F. Sciarrino, E. Santamato, R. W. Boyd, and L. Marrucci, "Quantum walks and wavepacket dynamics on a lattice with twisted photons", Science Advances **1** (2015).

[33] A. Schreiber, K. N. Cassemiro, V. Potocek, A. Gábris, P. J. Mosley, E. Andersson, I. Jex, and C. Silberhorn, "Photons walking the line: a quantum walk with adjustable coin operations", Phys. Rev. Lett. **104**, 050502 (2010).

[34] Y. Bromberg, Y. Lahini, R. Morandotti, and Y. Silberberg, "Quantum and classical correlations in waveguide lattices", Phys. Rev. Lett. **102**, 253904 (2009).

[35] A. Peruzzo, M. Lobino, J. C. F. Matthews, N. Matsuda, A. Politi, K. Poulios, X.-Q. Zhou, Y. Lahini, N. Ismail, K. Wörhoff, Y. Bromberg, Y. Silberberg, M. G. Thompson, and J. L. OBrien, "Quantum walks of correlated photons", Science **329**, 1500–1503 (2010).

[36] J. O. Owens, M. A. Broome, D. N. Biggerstaff, M. E. Goggin, A. Fedrizzi, T. Linjordet, M. Ams, G. D. Marshall, J. Twamley, M. J. Withford, and A. G. White, "Two-photon quantum walks in an elliptical direct-write waveguide array", New Journal of Physics **13**, 075003 (2011).

[37] L. Sansoni, F. Sciarrino, G. Vallone, P. Mataloni, A. Crespi, R. Ramponi, and R. Osellame, "Two-particle bosonic-fermionic quantum walk via integrated photonics", Phys. Rev. Lett. **108**, 010502 (2012).

[38] G. Di Giuseppe, L. Martin, A. Perez-Leija, R. Keil, F. Dreisow, S. Nolte, A. Szameit, A. F. Abouraddy, D. N. Christodoulides, and B. E. A. Saleh, "Einstein-podolsky-rosen spatial entanglement in ordered and anderson photonic lattices", Phys. Rev. Lett. **110**, 150503 (2013).

[39] J. D. A. Meinecke, K. Poulios, A. Politi, J. C. F. Matthews, A. Peruzzo, N. Ismail, K. Wörhoff, J. L. O'Brien, and M. G. Thompson, "Coherent time evolution and boundary conditions of two-photon quantum walks in waveguide arrays", Phys. Rev. A **88**, 012308 (2013).

[40] K. Poulios, R. Keil, D. Fry, J. D. A. Meinecke, J. C. F. Matthews, A. Politi, M. Lobino, M. Gräfe, M. Heinrich, S. Nolte, A. Szameit, and J. L. O'Brien, "Quantum walks of correlated photon pairs in two-dimensional waveguide arrays", Phys. Rev. Lett. **112**, 143604 (2014).

[41] A. Crespi, R. Osellame, R. Ramponi, V. Giovannetti, R. Fazio, L. Sansoni, F. De Nicola, F. Sciarrino, and P. Mataloni, "Anderson localization of entangled photons in an integrated quantum walk", Nature Photonics **7**, 322–328 (2013).

[42] S. E. Venegas-Andraca, "Quantum walks: a comprehensive review", Quantum Information Processing **11**, 1015–1106 (2012).

[43] A. Ambainis, E. Bach, A. Nayak, A. Vishwanath, and J. Watrous, "One-dimensional quantum walks", in Proceedings of the thirty-third annual acm symposium on theory of computing, STOC '01 (2001), pp. 37–49.

[44] A. Gerrard and J. Burch, *Introduction to matrix methods in optics*, Dover Books on Physics (Dover, 1994).

[45] E. Prince, *Mathematical techniques in crystallography and materials science* (Springer Berlin Heidelberg, 2004).

[46] A. Schreiber, "Quantum walks in time", Doctoral Thesis (Friedrich-Alexander-Universität Erlangen-Nürnberg (FAU), 2013).

[47] M. Santha, "Quantum walk based search algorithms", in Theory and applications of models of computation, edited by M. Agrawal, D. Du, Z. Duan, and A. Li (2008), pp. 31–46.

[48]M. Ornigotti, L. Maczewsky, and A. Szameit, *Lecture notes in fundamentals of quantum optics*, June 2016.

[49]L. Lorz, E. Meyer-Scott, T. Nitsche, V. Potocek, A. Gábris, S. Barkhofen, I. Jex, and C. Silberhorn, "A photonic quantum walk with a four-dimensional coin", in (Sept. 2018).

[50]C. S. Hamilton, A. Gábris, I. Jex, and S. M. Barnett, "Quantum walk with a four-dimensional coin", New Journal of Physics **13**, 013015 (2011).

[51]M. Wimmer, H. M. Price, I. Carusotto, and U. Peschel, "Experimental measurement of the berry curvature from anomalous transport", Nature Physics, 545–550 (2016).

[52]M. V. Berry, "Quantal phase factors accompanying adiabatic changes", Proceedings of the Royal Society of London. A. Mathematical and Physical Sciences **392**, 45–57 (1984).

[53]Y. Aharonov and J. Anandan, "Phase change during a cyclic quantum evolution", Phys. Rev. Lett. **58**, 1593–1596 (1987).

[54]A. H. Castro Neto, F. Guinea, N. M. R. Peres, K. S. Novoselov, and A. K. Geim, "The electronic properties of graphene", Rev. Mod. Phys. **81**, 109–162 (2009).

[55]J. C.F. Matthews, K. Poulios, J. Meinecke, A. Politi, A. Peruzzo, N. Ismail, K. Worhoff, M. G Thompson, and J. O'Brien, "Corrigendum: observing fermionic statistics with photons in arbitrary processes", Scientific reports **3**, 1539 (2013).

[56]W. D. Heiss, "Exceptional points of non-hermitian operators", Journal of Physics A: Mathematical and General **37**, 2455–2464 (2004).

[57]K. Kawabata, T. Bessho, and M. Sato, "Classification of exceptional points and non-hermitian topological semimetals", Phys. Rev. Lett. **123**, 066405 (2019).

[58]B. Midya, H. Zhao, and L. Feng, "Non-hermitian photonics promises exceptional topology of light", Nature Communications **9**, 752–762 (2018).

[59]S. Longhi, "Floquet exceptional points and chirality in non-hermitian hamiltonians", Journal of Physics A: Mathematical and Theoretical **50**, 505201 (2017).

[60]W. Heiss and H. Harney, "The chirality of exceptional points", The European Physical Journal D - Atomic, Molecular, Optical and Plasma Physics **17**, 149–151 (2001).

[61]A. Fang, Z.-Q. Zhang, S. G. Louie, and C. Chan, "Pseudospin-1 physics of photonic crystals", Research **2019**, 1–15 (2019).

[62]J. K. Asboth, B. Tarasinski, and P. Delplace, "Chiral symmetry and bulk-boundary correspondence in periodically driven one-dimensional systems", Phys. Rev. B **90**, 125143 (2014).

[63]J. K. Asboth and H. Obuse, "Bulk-boundary correspondence for chiral symmetric quantum walks", Phys. Rev. B **88**, 121406 (2013).

[64]D. Kim, M. Ken, N. Kawakami, and H. Obuse, "Floquet topological phases driven by $\mathcal{PT}$ symmetric nonunitary time evolution", (2016).

[65]A. P. Schnyder, S. Ryu, A. Furusaki, and A. W. W. Ludwig, "Classification of topological insulators and superconductors in three spatial dimensions", Phys. Rev. B **78**, 195125 (2008).

[66]C.-K. Chiu, J. C. Y. Teo, A. P. Schnyder, and S. Ryu, "Classification of topological quantum matter with symmetries", Rev. Mod. Phys. **88**, 035005 (2016).

[67]A. Kitaev, "Periodic table for topological insulators and superconductors", AIP Conference Proceedings **1134**, 22–30 (2009).

[68]J. C. Teo and T. L. Hughes, "Topological defects in symmetry-protected topological phases", Annual Review of Condensed Matter Physics **8**, 211–237 (2017).

[69]J. C. Y. Teo and C. L. Kane, "Topological defects and gapless modes in insulators and superconductors", Phys. Rev. B **82**, 115120 (2010).

[70]S. Matsuura, P.-Y. Chang, A. P. Schnyder, and S. Ryu, "Protected boundary states in gapless topological phases", New Journal of Physics **15**, 065001 (2013).

[71]C.-K. Chiu and A. P. Schnyder, "Classification of reflection-symmetry-protected topological semimetals and nodal superconductors", Phys. Rev. B **90**, 205136 (2014).

[72]T. Morimoto and A. Furusaki, "Topological classification with additional symmetries from clifford algebras", Phys. Rev. B **88** (2013).

[73]M. Koshino, T. Morimoto, and M. Sato, "Topological zero modes and dirac points protected by spatial symmetry and chiral symmetry", Phys. Rev. B **90**, 115207 (2014).

[74]K. Shiozaki and M. Sato, "Topology of crystalline insulators and superconductors", Phys. Rev. B **90** (2014).

[75]R. Roy and F. Harper, "Periodic table for floquet topological insulators", Phys. Rev. B **96**, 155118 (2017).

[76]F. Nathan and M. S. Rudner, "Topological singularities and the general classification of floquet–bloch systems", New Journal of Physics **17**, 125014 (2015).

[77]D. V. Else and C. Nayak, "Classification of topological phases in periodically driven interacting systems", Phys. Rev. B **93**, 201103 (2016).

[78]D. Leykam, M. C. Rechtsman, and Y. D. Chong, "Anomalous topological phases and unpaired dirac cones in photonic floquet topological insulators", Phys. Rev. Lett. **117**, 013902 (2016).

[79]M. S. Rudner, N. H. Lindner, E. Berg, and M. Levin, "Anomalous edge states and the bulk-edge correspondence for periodically driven two-dimensional systems", Phys. Rev. X **3**, 031005 (2013).

[80]T. Kitagawa, E. Berg, M. Rudner, and E. Demler, "Topological characterization of periodically driven quantum systems", Phys. Rev. B **82**, 235114 (2010).

[81]L. Feng, Y.-L. Xu, W. Fegadolli, M.-H. Lu, J. Oliveira, V. Almeida, Y.-F. Chen, and A. Scherer, "Experimental demonstration of a unidirectional reflectionless parity-time metamaterial at optical frequencies", Nature materials **12** (2012).

[82]L. Feng, R. El-Ganainy, and L. Ge, "Non-hermitian photonics based on parity–time symmetry", Nature Photonics **11** (2017).

[83]Y.-L. Xu, W. Fegadolli, L. Gan, M.-H. Lu, X.-P. Liu, Z.-Y. Li, A. Scherer, and Y.-F. Chen, "Experimental realization of bloch oscillations in a parity-time synthetic silicon photonic lattice", Nature Communications **7**, 11319 (2016).

[84]M. Wimmer, M.-A. Miri, D. Christodoulides, and U. Peschel, "Observation of bloch oscillations in complex $\mathcal{PT}$-symmetric photonic lattices", Scientific Reports **5**, 17760 (2015).

[85]A. Regensburger, C. Bersch, M.-A. Miri, G. Onishchukov, D. N Christodoulides, and U. Peschel, "Parity time synthetic photonic lattices", Nature **488**, 167–71 (2012).

[86] A. Mostafazadeh, "Invisibility and $\mathcal{PT}$ symmetry", Phys. Rev. A **87**, 012103 (2013).

[87] S. Ozdemir, S. Rotter, F. Nori, and L. Yang, "Parity–time symmetry and exceptional points in photonics", Nature Materials **18**, 1 (2019).

[88] H. Hodaei, A. Hassan, S. Wittek, H. Garcia-Gracia, R. El-Ganainy, D. Christodoulides, and M. Khajavikhan, "Enhanced sensitivity at higher-order exceptional points", Nature **548**, 187–191 (2017).

[89] P. Djorwe, Y. Pennec, and B. Djafari-Rouhani, "Exceptional point enhances sensitivity of optomechanical mass sensors", Phys. Rev. Applied **12**, 024002 (2019).

[90] K. Kawabata, Y. Ashida, H. Katsura, and M. Ueda, "Parity-time-symmetric topological superconductor", Phys. Rev. B **98**, 085116 (2018).

[91] Z. Gong, Y. Ashida, K. Kawabata, K. Takasan, S. Higashikawa, and M. Ueda, "Topological phases of non-hermitian systems", Phys. Rev. X **8**, 031079 (2018).

[92] H. Shen, B. Zhen, and L. Fu, "Topological band theory for non-hermitian hamiltonians", Phys. Rev. Lett. **120**, 146402 (2018).

[93] A. Mostafazadeh, "Pseudo-hermiticity versus pt symmetry: the necessary condition for the reality of the spectrum of a non-hermitian hamiltonian", Journal of Mathematical Physics **43**, 205–214 (2002).

[94] V. Lutsky, E. Luz, E. Granot, and B. A. Malomed, "Making the $\mathcal{PT}$ symmetry unbreakable", in (2018).

[95] A. Schreiber, K. N. Cassemiro, V. Potocek, A. Gábris, P. J. Mosley, E. Andersson, I. Jex, and C. Silberhorn, "Decoherence and disorder in quantum walks: from ballistic spread to localization", Phys. Rev. Lett. **106**, 180403 (2011).

[96] A. Schreiber, A. Gábris, P. P. Rohde, K. Laiho, M. Štefaňák, V. Potoček, C. Hamilton, I. Jex, and C. Silberhorn, "A 2D quantum walk simulation of two-particle dynamics", Science **336**, 55–58 (2012).

[97] M.-A. Miri, A. Regensburger, U. Peschel, and D. N. Christodoulides, "Optical mesh lattices with $\mathcal{PT}$ symmetry", Phys. Rev. A **86**, 023807 (2012).

[98] A. Regensburger, M.-A. Miri, C. Bersch, J. Näger, G. Onishchukov, D. N Christodoulides, and U. Peschel, "Observation of defect states in $\mathcal{PT}$-symmetric optical lattices", Phys. Rev. Lett. **110**, 223902 (2013).

[99] M. Wimmer, A. Regensburger, M.-A. Miri, C. Bersch, D. N. Christodoulides, and U. Peschel, "Observation of optical solitons in $\mathcal{PT}$-symmetric lattices", Nature communications **6** (2015).

[100] A. Regensburger, C. Bersch, B. Hinrichs, G. Onishchukov, A. Schreiber, C. Silberhorn, and U. Peschel, "Zitterbewegung, bloch oscillations and landau-zener tunneling in a quantum walk", (2011).

[101] M. Wimmer and U. Peschel, "Observation of time reversed light propagation by an exchange of eigenstates", Scientific Reports **8** (2018).

[102] A. V. Pankov, I. Vatnik, D. Churkin, and S. Derevyanko, "Anderson localization in synthetic photonic lattice with random coupling", Optics Express **27**, 4424 (2019).

[103] I. Prigogine and G. Nicolis, *Self-organisation in nonequilibrium systems: towards a dynamics of complexity*, edited by M. Hazewinkel, R. Jurkovich, and J. H. P. Paelinck (Springer Netherlands, Dordrecht, 1985).

[104] J. Klaers, F. Vewinger, and M. Weitz, "Thermalization of a two-dimensional photonic gas in a "white wall" photon box", Nature Physics **6**, 512–515 (2010).

[105] J. Klaers, J. Schmitt, F. Vewinger, and M. Weitz, "Bose-einstein condensation of photons in an optical microcavity", Nature **468**, 545–8 (2010).

[106] T. Damm, J. Schmitt, Q. Liang, D. Dung, F. Vewinger, M. Weitz, and J. Klaers, "Calorimetry of a bose einstein condensed photon gas", Nature Communications **7**, 11340 (2016).

[107] C. Sun, S. Jia, C. Barsi, S. Rica, A. Picozzi, and J. Fleischer, "Observation of the condensation of classical waves", Nature Physics **8**, 470 (2012).

[108] T. Peyronel, O. Firstenberg, Q.-Y. Liang, S. Hofferberth, A. Gorshkov, T. Pohl, M. Lukin, and V. Vuletic, "Quantum nonlinear optics with single photons enabled by strongly interacting atoms", Nature **488**, 57–60 (2012).

[109] O. Firstenberg, T. Peyronel, Q.-Y. Liang, A. Gorshkov, M. Lukin, and V. Vuletic, "Attractive photons in a quantum nonlinear medium", Nature **502**, 71–75 (2013).

[110] D. Chang, V. Vuletic, and M. Lukin, "Quantum nonlinear optics - photon by photon", Nature Photonics **8**, 685–694 (2014).

[111] N. Manton and P. Sutcliffe, *Topological solitons*, Cambridge Monographs on Mathematical Physics (Cambridge University Press, 2007).

[112] N. Akhmediev and A. Ankiewicz, *Dissipative solitons in the complex ginzburg-landau and swift-hohenberg equations*, edited by N. Akhmediev and A. Ankiewicz (Springer Berlin Heidelberg, Berlin, Heidelberg, 2005).

[113] P. Grelu and N. Akhmediev, "Dissipative solitons for mode-locked lasers", Nature Photonics **6**, 84–92 (2012).

[114] G. P. Agrawal, *Nonlinear fiber optics (fourth edition)*, Fourth Edition, Optics and Photonics (Academic Press, San Diego, 2006).

[115] F. K. Abdullaev, Y. V. Kartashov, V. V. Konotop, and D. A. Zezyulin, "Solitons in $\mathcal{PT}$-symmetric nonlinear lattices", Phys. Rev. A **83**, 041805 (2011).

[116] R. Driben and B. A. Malomed, "Stability of solitons in parity-time-symmetric couplers", Opt. Lett. **36**, 4323–4325 (2011).

[117] X. Zhu, H. Wang, L.-X. Zheng, H. Li, and Y.-J. He, "Gap solitons in parity-time complex periodic optical lattices with the real part of superlattices", Opt. Lett. **36**, 2680–2682 (2011).

[118] Z. Shi, X. Jiang, X. Zhu, and H. Li, "Bright spatial solitons in defocusing kerr media with $\mathcal{PT}$-symmetric potentials", Phys. Rev. A **84**, 053855 (2011).

[119] Y. V. Bludov, V. V. Konotop, and B. A. Malomed, "Stable dark solitons in $\mathcal{PT}$-symmetric dual-core waveguides", Phys. Rev. A **87**, 013816 (2013).

[120] Y. V. Kartashov, B. A. Malomed, and L. Torner, "Unbreakable $\mathcal{PT}$ symmetry of solitons supported by inhomogeneous defocusing nonlinearity", Opt. Lett. **39**, 5641–5644 (2014).

[121] Y. Lumer, Y. Plotnik, M. C. Rechtsman, and M. Segev, "Nonlinearly induced $\mathcal{PT}$ transition in photonic systems", Phys. Rev. Lett. **111**, 263901 (2013).

[122] I. Barashenkov, D. Pelinovsky, and P. Dubard, "Dimer with gain and loss: integrability and $\mathcal{PT}$-symmetry restoration", Journal of Physics A Mathematical and Theoretical **48**, 325201 (2015).

[123] A. A. Sukhorukov and Y. S. Kivshar, "Spatial optical solitons in nonlinear photonic crystals", Phys. Rev. E **65**, 036609 (2002).

[124] A. A. Sukhorukov and Y. S. Kivshar, "Nonlinear guided waves and spatial solitons in a periodic layered medium", J. Opt. Soc. Am. B **19**, 772–781 (2002).

[125] D. E. Pelinovsky, A. A. Sukhorukov, and Y. S. Kivshar, "Bifurcations and stability of gap solitons in periodic potentials", Phys. Rev. E **70**, 036618 (2004).

[126] A. A. Sukhorukov, Z. Xu, and Y. S. Kivshar, "Nonlinear suppression of time reversals in $\mathcal{PT}$-symmetric optical couplers", Phys. Rev. A **82**, 043818 (2010).

[127] A. A. Sukhorukov, S. V. Dmitriev, S. V. Suchkov, and Y. S. Kivshar, "Nonlocality in $\mathcal{PT}$-symmetric waveguide arrays with gain and loss", Opt. Lett. **37**, 2148–2150 (2012).

[128] N. V. Alexeeva, I. V. Barashenkov, A. A. Sukhorukov, and Y. S. Kivshar, "Optical solitons in $\mathcal{PT}$-symmetric nonlinear couplers with gain and loss", Phys. Rev. A **85**, 063837 (2012).

[129] I. V. Barashenkov, S. V. Suchkov, A. A. Sukhorukov, S. V. Dmitriev, and Y. S. Kivshar, "Breathers in $\mathcal{PT}$-symmetric optical couplers", Phys. Rev. A **86**, 053809 (2012).

[130] J. Yang, "Can parity-time-symmetric potentials support families of non-parity-time-symmetric solitons?", Studies in Applied Mathematics **132** (2013).

[131] J. Yang, "Symmetry breaking of solitons in one-dimensional parity-time-symmetric optical potentials", Optics Letters **39** (2014).

[132] P. Li, C. Dai, R. Li, and Y. Gao, "Symmetric and asymmetric solitons supported by a $\mathcal{PT}$-symmetric potential with saturable nonlinearity: bifurcation, stability and dynamics", Opt. Express **26**, 6949–6961 (2018).

[133] S. Flach and C. Willis, "Discrete breathers", Physics Reports **295**, 181–264 (1998).

[134] Z. Shi and J. Yang, "Solitary waves bifurcated from bloch-band edges in two-dimensional periodic media", Phys. Rev. E **75**, 056602 (2007).

[135] P. L. Christiansen, Y. B. Gaididei, V. K. Mezentsev, S. L. Musher, K. Ø. Rasmussen, J. J. Rasmussen, I. V. Ryzhenkova, and S. K. Turitsyn, "Discrete localized states and localization dynamics in discrete nonlinear schrödinger equations", Physica Scripta **T67**, 160–166 (1996).

[136] E. W. Laedke, K. H. Spatschek, and S. K. Turitsyn, "Stability of discrete solitons and quasicollapse to intrinsically localized modes", Phys. Rev. Lett. **73**, 1055–1059 (1994).

[137] K. D. Moll, A. L. Gaeta, and G. Fibich, "Self-similar optical wave collapse: observation of the townes profile", Phys. Rev. Lett. **90**, 203902 (2003).

[138] C. Sulem and P. Sulem, *The nonlinear schrödinger equation: self-focusing and wave collapse*, Applied Mathematical Sciences (Springer New York, 1999).

[139] H. Chen and S. Hu, "The asymmetric solitons in two-dimensional parity-time symmetric potentials", Physics Letters A **380** (2015).

[140] J. Yang, "Symmetry breaking of solitons in two-dimensional complex potentials", Phys. Rev. E **91** (2014).

[141] Y. S. Kivshar and D. K. Campbell, "Peierls-nabarro potential barrier for highly localized nonlinear modes", Phys. Rev. E **48**, 3077–3081 (1993).

[142] C. L. Kane and E. J. Mele, "Z2 topological order and the quantum spin hall effect", Phys. Rev. Lett. **95**, 146802 (2005).

[143] B. A. Bernevig, T. L. Hughes, and S.-C. Zhang, "Quantum spin hall effect and topological phase transition in hgte quantum wells", Science **314**, 1757–1761 (2006).

[144] C. L. Kane and E. J. Mele, "Quantum spin hall effect in graphene", Phys. Rev. Lett. **95**, 226801 (2005).

[145] R. El-Ganainy and M. Levy, "Optical isolation in topological-edge-state photonic arrays", Opt. Lett. **40**, 5275–5278 (2015).

[146] S. Weimann, M. Kremer, Y. Plotnik, Y. Lumer, S. Nolte, K. Makris, M. Segev, M. Rechtsman, and A. Szameit, "Topologically protected bound states in photonic parity-time symmetric crystals", Nature Materials **16** (2016).

[147] M. Rechtsman, J. Zeuner, Y. Plotnik, Y. Lumer, D. Podolsky, F. Dreisow, S. Nolte, M. Segev, and A. Szameit, "Photonic floquet topological insulators", Nature **496**, 196–200 (2013).

[148] Z. Wang, Y. Chong, J. Joannopoulos, and M. Soljacic, "Observation of unidirectional backscattering-immune topological electromagnetic states", Nature **461**, 772–5 (2009).

[149] A. Khanikaev, S. Mousavi, W.-K. Tse, M. Kargarian, A. Macdonald, and G. Shvets, "Photonic topological insulators", Nat Mat 12, 3 (2013).

[150] M. Hafezi, S. Mittal, J. Fan, A. Migdall, and J. Taylor, "Imaging topological edge states in silicon photonics", Nature Photonics **7**, 1001–1005 (2013).

[151] M. Hafezi, E. Demler, M. Lukin, and J. Taylor, "Robust optical delay lines via topological protection", Nature Physics **7** (2011).

[152] M. Verbin, O. Zilberberg, Y. E. Kraus, Y. Lahini, and Y. Silberberg, "Observation of topological phase transitions in photonic quasicrystals", Phys. Rev. Lett. **110**, 076403 (2013).

[153] M. Verbin, O. Zilberberg, Y. Lahini, Y. E. Kraus, and Y. Silberberg, "Topological pumping over a photonic fibonacci quasicrystal", Phys. Rev. B **91**, 064201 (2015).

[154] Y. E. Kraus, Y. Lahini, Z. Ringel, M. Verbin, and O. Zilberberg, "Topological states and adiabatic pumping in quasicrystals", Phys. Rev. Lett. **109**, 106402 (2012).

[155] T. Kitagawa, M. Broome, A. Fedrizzi, M. Rudner, E. Berg, I. Kassal, A. Aspuru-Guzik, E. Demler, and A. White, "Observation of topologically protected bound states in photonic quantum walks", Nature communications **3**, 882 (2012).

[156] L. Xiao, X. Zhan, Z. Bian, K. Wang, X. Zhang, X. Wang, J. Li, K. Mochizuki, D. Kim, N. Kawakami, W. Yi, H. Obuse, B. Sanders, and P. Xue, "Observation of topological edge states in parity–time-symmetric quantum walks", Nature Physics **13** (2017).

[157] K. Esaki, M. Sato, K. Hasebe, and M. Kohmoto, "Edge states and topological phases in non-hermitian systems", Phys. Rev. B **84**, 205128 (2011).

[158] H. Schomerus, "Topologically protected midgap states in complex photonic lattices", Optics letters **38**, 1912–4 (2013).

[159] S. Malzard, C. Poli, and H. Schomerus, "Topologically protected defect states in open photonic systems with non-hermitian charge-conjugation and parity-time symmetry", Phys. Rev. Lett. **115** (2015).

[160] T. E. Lee, "Anomalous edge state in a non-hermitian lattice", Phys. Rev. Lett. **116**, 133903 (2016).

161 J. M. Zeuner, M. C. Rechtsman, Y. Plotnik, Y. Lumer, S. Nolte, M. S. Rudner, M. Segev, and A. Szameit, "Observation of a topological transition in the bulk of a non-hermitian system", Phys. Rev. Lett. **115**, 040402 (2015).

162 M. Kremer, T. Biesenthal, M. Heinrich, R. Thomale, and A. Szameit, "Demonstration of a two-dimensional $\mathcal{PT}$-symmetric crystal", Nature Communications **10** (2019).

163 W. P. Su, J. R. Schrieffer, and A. J. Heeger, "Solitons in polyacetylene", Phys. Rev. Lett. **42**, 1698–1701 (1979).

164 Z. Fedorova (Cherpakova), C. Jörg, C. Dauer, F. Letscher, M. Fleischhauer, S. Eggert, S. Linden, and G. von Freymann, "Limits of topological protection under local periodic driving", Light Sci. Appl. **8** (2019).

165 A. Blanco-Redondo, I. Andonegui, M. J. Collins, G. Harari, Y. Lumer, M. C. Rechtsman, B. J. Eggleton, and M. Segev, "Topological optical waveguiding in silicon and the transition between topological and trivial defect states", Phys. Rev. Lett. **116**, 163901 (2016).

166 N. Malkova, I. Hromada, X. Wang, G. Bryant, and Z. Chen, "Transition between tamm-like and shockley-like surface states in optically induced photonic superlattices", Phys. Rev. A **80**, 043806 (2009).

167 X. Liu, F. Harper, and R. Roy, "Chiral flow in one-dimensional floquet topological insulators", Phys. Rev. B **98**, 165116 (2018).

168 S. Rachel, "Interacting topological insulators: a review", Reports on Progress in Physics **81** (2018).

169 L. Fidkowski and A. Kitaev, "Topological phases of fermions in one dimension", Phys. Rev. B **83**, 075103 (2011).

170 S. Ryu and Y. Hatsugai, "Zero-energy edge states and chiral symmetry breaking at edges of graphite sheets", Physica E Low-dimensional Systems and Nanostructures **22** (2003).

171 H. Guo and S.-Q. Shen, "Topological phase in a one-dimensional interacting fermion system", Phys. Rev. B **84**, 195107 (2011).

172 F. Grusdt, M. Höning, and M. Fleischhauer, "Topological edge states in the one-dimensional superlattice bose-hubbard model", Phys. Rev. Lett. **110**, 260405 (2013).

173 S. R. Manmana, A. M. Essin, R. M. Noack, and V. Gurarie, "Topological invariants and interacting one-dimensional fermionic systems", Phys. Rev. B **86**, 205119 (2012).

174 L. Barbiero, L. Santos, and N. Goldman, "Quenched dynamics and spin-charge separation in an interacting topological lattice", Phys. Rev. B **97**, 201115 (2018).

175 D. Wang, S. Xu, Y. Wang, and C. Wu, "Detecting edge degeneracy in interacting topological insulators through entanglement entropy", Phys. Rev. B **91**, 115118 (2015).

176 J. Junemann, A. Piga, S.-J. Ran, M. Lewenstein, M. Rizzi, and A. Bermudez, "Exploring interacting topological insulators with ultracold atoms: the synthetic creutz-hubbard model", Phys. Rev. X **7**, 031057 (2017).

177 J. Sirker, M. Maiti, N. P. Konstantinidis, and N. Sedlmayr, "Boundary fidelity and entanglement in the symmetry protected topological phase of the SSH model", Journal of Statistical Mechanics: Theory and Experiment **2014**, P10032 (2014).

[178]P. St-Jean, V. Goblot, E. Galopin, A. Lemaitre, T. Ozawa, L. Legratiet, I. Sagnes, J. Bloch, and A. Amo, "Lasing in topological edge states of a one-dimensional lattice", Nature Photonics **11** (2017).

[179]D. A. Dobrykh, A. V. Yulin, A. P. Slobozhanyuk, A. N. Poddubny, and Y. S. Kivshar, "Nonlinear control of electromagnetic topological edge states", Phys. Rev. Lett. **121**, 163901 (2018).

[180]S. Kruk, A. Poddubny, D. Smirnova, L. Wang, A. Slobozhanyuk, A. Shorokhov, I. Kravchenko, B. Luther-Davies, and Y. Kivshar, "Nonlinear light generation in topological nanostructures", Nature Nanotechnology **14**, 126–130 (2019).

[181]D. D. Solnyshkov, O. Bleu, B. Teklu, and G. Malpuech, "Chirality of topological gap solitons in bosonic dimer chains", Phys. Rev. Lett. **118**, 023901 (2017).

[182]S. Mukherjee and M. Rechtsman, "Observation of topological band gap solitons", in (2019).

[183]G. Harari, M. Bandres, Y. Lumer, M. Rechtsman, Y. Chong, M. Khajavikhan, D. Christodoulides, and M. Segev, "Topological insulator laser: theory", Science **359** (2018).

[184]M. A. Bandres, S. Wittek, G. Harari, M. Parto, J. Ren, M. Segev, D. N. Christodoulides, and M. Khajavikhan, "Topological insulator laser: experiments", Science **359** (2018).

[185]S. Klembt, T. Harder, O. Egorov, K. Winkler, R. Ge, M. Bandres, M. Emmerling, T. Liew, M. Segev, C. Schneider, and S. Höfling, "Exciton-polariton topological insulator", Nature **562**, 552–556 (2018).

[186]J. K. Asboth, "Symmetries, topological phases, and bound states in the one-dimensional quantum walk", Phys. Rev. B **86**, 195414 (2012).

[187]M. Sato, Y. Tanaka, K. Yada, and T. Yokoyama, "Topology of andreev bound states with flat dispersion", Phys. Rev. B **83**, 224511 (2011).

[188]M. Kremer, "Topological effects in fibre networks", Masterarbeit (Friedrich-Schiller-Universität Jena, 2017).

[189]J. Asboth, L. Oroszlany, and A. Palyi, *A short course on topological insulators: bandstructure and edge states in one and two dimensions* (Springer International Publishing, 2016).

[190]Y. Hadad, A. B. Khanikaev, and A. Alu, "Self-induced topological transitions and edge states supported by nonlinear staggered potentials", Phys. Rev. B **93**, 155112 (2016).

[191]S. Longhi, "Bloch oscillations in complex crystals with $\mathcal{PT}$ symmetry", Phys. Rev. Lett. **103**, 123601 (2009).

[192]T. W. B. Kibble, "Topology of cosmic domains and strings", Journal of Physics A: Mathematical and General **9**, 1387–1398 (1976).

[193]T. Kibble, "Some implications of a cosmological phase transition", Physics Reports **67**, 183–199 (1980).

[194]Y. Bromberg, Y. Lahini, and Y. Silberberg, "Bloch oscillations of path-entangled photons", Phys. Rev. Lett. **105**, 263604 (2010).

Ehrenwörtliche Erklärung

Ich erkläre hiermit ehrenwörtlich, dass ich die vorliegende Arbeit selbständig, ohne unzulässige Hilfe Dritter und ohne Benutzung anderer als der angegebenen Hilfsmittel und Literatur angefertigt habe. Die aus anderen Quellen direkt oder indirekt übernommenen Daten und Konzepte sind unter Angabe der Quelle gekennzeichnet.

Niemand war an der inhaltlich-materiellen Erstellung der vorliegenden Arbeit beteiligt. Insbesondere habe ich hierfür nicht die entgeltliche Hilfe von Vermittlungs bzw. Beratungsdiensten (Promotionsberater oder andere Personen) in Anspruch genommen. Niemand hat von mir unmittelbar oder mittelbar geldwerte Leistungen für Arbeiten erhalten, die im Zusammenhang mit dem Inhalt der vorgelegten Dissertation stehen.

Die Arbeit wurde bisher weder im In- noch im Ausland in gleicher oder ähnlicher Form einer anderen Prüfungsbehörde vorgelegt.

Die geltende Promotionsordnung der Physikalisch-Astronomischen Fakultät ist mir bekannt.

Ich versichere ehrenwörtlich, dass ich nach bestem Wissen die reine Wahrheit gesagt und nichts verschwiegen habe.

_____   _____
Ort, Datum   Unterschrift d. Verfassers

Acknowledgements